Université Sorbonne Paris Nord
Institut Galilée

Laboratoire de physique des lasers

Habilitation à diriger des recherches
Spécialité: Sciences

présentée par
Romain Dubessy

Sujet de la thèse d'habilitation:

Contributions to the study of out-of-equilibrium superfluids in one and two dimensions

Contributions à l'étude des superfluides hors équilibre en dimensions un et deux

Soutenance prévue le 14 Avril ou le 30 Mai 2023 devant le jury composé de:

Mme	Anne Amy-Klein	Examinatrice
M.	Jérôme Beugnon	Examinateur
M.	Mariusz Gajda	Rapporteur
M.	David Guéry-Odelin	Rapporteur
Mme	Hélène Perrin	Examinatrice
M.	Wolf von Klitzing	Rapporteur

Contents

Curriculum Vitae

Romain Dubessy
Tél: 01 49 40 33 96 — born on December 22nd, 1983
romain.dubessy@univ-paris13.fr — no children

Education and employment

Since 2022 Maître de conférence hors classe at Laboratoire de physique des lasers (UMR 7538 CNRS / Université Sorbonne Paris Nord) in the BEC (Bose-Einstein condensates) group lead by Hélène Perrin.
Research interests:

- ultracold atoms (*Bose-Einstein condensates, superfluidity, collective modes, low dimensional systems, fast rotation, supersonic flow*)
- atom-photon interactions (*laser cooling & trapping, non-linear effects, radio-frequency dressed magnetic traps*)
- theoretical models (*Gross-Pitaevskii equation, classical fields, generalized hydrodynamics*).

2012-2022 Maître de conférence, classe normale, in the BEC group.

2010-2012 Post-doctoral position, in the BEC group.

2007-2010 PhD thesis, Université Paris Diderot, entitled: *Réalisation, étude et exploitation d'ensembles d'ions refroidis par laser stockés dans des pièges micro-fabriqués pour l'information quantique*, defended on October 12th 2010. Work done under the supervision of Luca Guidoni, in the trapped ions and quantum information group of Laboratoire Matériaux et Phénomènes Quantiques. Referees: Isabelle Bouchoule and Ferdinand Schmidt-Kaler.
Keywords: trapped ions, laser cooling, quantum information, repeaters, photo-ionization, anomalous heating.

2006-2007 Master degree in fundamental concepts of physics, specialization in quantum physics, École normale supérieure, Paris

2003-2007 Engineering degree at École polytechnique, Palaiseau

Professional offices

Supervision and management of research activities

Supervision:

1. Supervision (50%) of the PhD thesis of Rishabh Sharma, started in September 2021.

2. Supervision of a work contributing to the PhD thesis of Abhik Kumar Saha, defended in May 2022. Due to the pandemics this supervision consisted only in weekly online meetings. A work was published [Saha and Dubessy, 2021] and another one has been submitted [Saha and Dubessy, 2022].

3. Supervision of a post-doc, Avinash Kumar, on a work proposing a phase imprinting scheme for a ring shaped BEC [Kumar *et al.*, 2018].

4. Supervision of a part of the PhD thesis of David Rey, defended in January 2023, concerning the upgrade of the experiment control system. A technical work has been published [Rey *et al.*, 2022].

5. Supervision of parts of the PhD work of previous PhD students: Yanliang Guo, Mathieu de Goër de Herve, Camilla De Rossi, Dani Ben Ali and Karina Merloti. These contributions and the related works are highlighted in the manuscript.

Research grants:

1. French research agency (ANR), VORTECS: Superfluid vortex turbulence on a curved surface, 2023–2026, coordinator, in collaboration with Sergey Nazarenko, 407 k€.

2. Région Île-de-France grant (Sirteq), HydroLive: Real-time out-of-equilibrium hydrodynamics in quantum fluids, 2021–2023, coordinator, in collaboration with Quentin Glorieux et Nicolas Pavloff, 180 k€.

3. Labex FIRST-TF, Atom based microwave imaging, 2016–2017, 27 k€.

4. Université Paris 13 grant, μWAFER: Microwave atomic Feshbach resonance, 2015–2016, 25 k€.

Management:

1. Member of the national council for the atomic, molecular and optics division (CNU section 30), since December 2019.

2. Member of the scientific committee for quantum technologies of the French research agency (ANR – CE47), since December 2020.

3. Hiring committee for a computer science engineer at Laboratoire de physique des lasers, July 2022.

4. Hiring committee for a fellow associate professor at Laboratoire de physique des lasers, June 2020.

5. Member of four PhD committees between October 2021 and December 2022.

Teaching duties, responsibilities and dissemination

Teaching duties:

I teach about 200 hours per year at the science institute of the university, known as *Institut Galilée* and more specifically in the Network and Telecommunication engineering degree of *Sup'Galilée*.

First year physics (2014–2021) This is a lecture common for all first year students from the Physics, Mathematics, Computer science, Chemistry and Engineering departments. It aims at introducing the basic tools used in science: calculus, vectors, scalar and vector products, differential equations and integration, through the study of dimensional analysis, equilibrium of mechanical systems, kinematics, dynamics and energy conservation.

Measures and digital signals (2012–2022) This is an introductory lecture to signal analysis for second year students focused on the physical aspects of data acquisition, sampling and digitization of a signal. I use Matlab and the Simulink tool during laboratory works to illustrate the concepts of frequency aliasing, quantization noise, frequency spectrum and data compression.

C programming (2012–2022) This is a third year lecture for engineering school students, focused on the practical aspects of C programming: the students learn how to use a compiler, a debugger and an integrated development interface to write complex programs. It consists mainly in laboratory works in which students must solve a particular problem: write a database application or solve an optimization problem, as the traveling salesman, for example.

Robotics projects (2017–2023) I tutor a team of third year engineering school students that take part in the French robotics cup: they must build and program a autonomous robot capable of solving a particular task, in a given amount of time. This provides a good introduction to the use of micro-controllers and confronts the students to the difficulties of teamwork.

Telecommunication antennas (2013–2023) This fourth year lecture is an electromagnetism lecture for engineering students, focused on practical applications: the far field pattern, the gain, directivity and equivalent area of a wide variety of antennas. The students learn how to establish a transmission budget, the principle of operation of a radar or a phased antenna network and the measurement of radiation patterns during laboratory works.

Digital communications (2012–2023) I tutor fourth year engineering school students during electronics laboratory works aiming at understanding the principle of frequency modulation, by building from scratch a voltage controlled oscillator, using a phase lock loop or realizing a heterodyne detection with a local oscillator.

Teaching responsibilities:

Engineering degree – 2nd year From 2016 to 2018, I was in charge of the second year of the Telecommunications & Networks engineering program (about 30 students each year) and was therefore in charge of managing schedules, coordinating the professors and organizing the juries.

Director of studies Since September 2018, I am the director of studies of the Network and Telecommunication engineering degree, concerning a total of about 100 students: I manage the student selection, academic exchange programs, credit validation and participate in regular meetings to coordinate all the engineering school degrees.

Dissemination:

Scientific outreach As a member of Laboratoire de physique des lasers I participate in several scientific outreach events each year, as for example: the science fair, exhibitions and laboratory visits. In 2014 I co-founded the Atouts Sciences organization aiming at facilitating scientific outreach towards young people, and in particular high school students. Since then I am the secretary of the organization and in charge of the science by experience action. It consists in organizing the meeting between a group of high school students and a researcher to discover a spectacular optics experiment, as for example: a laser fountain, the stroboscopic effect or holography setups. In 2015–2017 we assembled and distributed a pedagogical kit *The LightBox* for high school teachers enabling them to realize with their students optics experiments as the observation of refraction, light guiding in a plastic fiber, polarization or diffraction. Thanks to a Labex First-TF grant we produced about 300 kits.

Publications

Research works published in international peer-reviewed journals

1. D. Rey, S. Thomas, R. Sharma, T. Badr, L. Longchambon, R. Dubessy, and H. Perrin. *Loading a quantum gas from a hybrid dimple trap to a shell trap.* Journal of Applied Physics **132**, 214401 (2022).

2. Y. Guo, E. Mercado Gutierrez, D. Rey, T. Badr, A. Perrin, L. Longchambon, V. Bagnato, H. Perrin, and R. Dubessy. *Expansion of a quantum gas in a shell trap.* New Journal of Physics **24**, 093040 (2022).

3. A. K. Saha and R. Dubessy. *Dynamical phase diagram of a one-dimensional Bose gas in a box with a tunable weak link: From Bose-Josephson oscillations to shock waves.* Physical Review A, **104**, 023316 (2021)

4. M. de Goër de Herve, Y. Guo, C. De Rossi, A. Kumar, T. Badr, R. Dubessy, L. Longchambon and H. Perrin. *A versatile ring trap for quantum gases.* Journal of Physics B, **54**, 125302 (2021)

5. R. Dubessy, J. Polo, H. Perrin, A. Minguzzi, and M. Olshanii. *Universal shock-wave propagation in one-dimensional Bose fluids.* Physical Review Research, **3**, 013098 (2021)

6. Y. Guo, R. Dubessy, M. de Goër de Herve, A. Kumar, T. Badr, A. Perrin, L. Longchambon, and H. Perrin. *Supersonic rotation of a superfluid: a long-lived dynamical ring.* Physical Review Letters, **124**, 025301 (2020). Selected as *Editor's suggestion* and for a synopsis in *Physics*. Highlighted by INP in *Reflets de la physique.*

7. J. Polo, R. Dubessy, P. Pedri, H. Perrin, and A. Minguzzi. *Oscillations and decay of superfluid currents in a one-dimensional Bose gas on a ring.* Physical Review Letters, **123**, 195301 (2019)

8. T. Badr, D. Ben Ali, J. Seaward, Y. Guo, F. Wiotte, R. Dubessy, H. Perrin, and A. Perrin. *Comparison of time profiles for the magnetic transport of cold atoms.* Applied Physics B, **125**, 102 (2019).

9. D. M. Segal, V. Lorent, R. Dubessy, and B. Darquié. *Studying fundamental physics using quantum enabled technologies with trapped molecular ions.* Journal Modern Optics, **65**, 490-500 (2018)

10. A. Kumar, R. Dubessy, T. Badr, C. De Rossi, M. de Goër De Herve, L. Longchambon and H. Perrin. *Producing superfluid circulation states using phase imprinting.* Physical Review A, **97**, 043615 (2018).

11. D. Ben Ali, T. Badr, T. Brézillon, R. Dubessy, H. Perrin and A. Perrin. *Detailed study of a transverse field Zeeman slower.* Journal of Physics B, **50**, 055008 (2017).

12. C. De Rossi, R. Dubessy, K. Merloti, M. De Goër de Herve, T. Badr, A. Perrin, L. Longchambon and H. Perrin. *Probing superfluidity in a quasi two-dimensional Bose gas through its local dynamics.* New Journal of Physics, **18**, 062001 (2016).

13. R. Dubessy, C. De Rossi, T. Badr, L. Longchambon and H. Perrin. *Imaging the collective excitations of an ultracold gas using statistical correlations*. New Journal of Physics, **16**, 122001 (2014). (Fast Track Communication). Accompanied by a video abstract and a news from INP.

14. B. Dubost, R. Dubessy, B. Szymanski, S. Guibal, J.-P. Likforman, and L. Guidoni. *Isotope shifts of natural Sr$^+$ measured by laser fluorescence in a sympathetically cooled Coulomb crystal*. Physical Review A **89**, 032504 (2014).

15. K. Merloti, R. Dubessy, L. Longchambon, M. Olshanii, and H. Perrin. *Breakdown of scale invariance in a quasi-two-dimensional Bose gas due to the presence of the third dimension*. Physical Review A **88**, 061603(R) (2013).

16. K. Merloti, R. Dubessy, L. Longchambon, A. Perrin, P.-E. Pottie, V. Lorent and H. Perrin. *A two-dimensional quantum gas in a magnetic trap*. New Journal of Physics, **15**, 033007 (2013).

17. R. Dubessy, T. Liennard, P. Pedri, and H. Perrin. *Critical rotation of an annular superfluid Bose-Einstein condensate*. Physical Review A, **86**, 011602(R) (2012).

18. B. Szymanski, R. Dubessy, B. Dubost, S. Guibal, J.-P. Likforman, and L. Guidoni. *Large two dimensional Coulomb crystals in a radio frequency surface ion trap*. Applied Physics Letters, **100**, 171110 (2012).

19. R. Dubessy, K. Merloti, L. Longchambon, P.-E. Pottie, T. Liennard, A. Perrin, V. Lorent, and H. Perrin. *Rubidium-87 Bose-Einstein condensate in an optically plugged quadrupole trap*. Physical Review A, **85**, 013643 (2012). Erratum Physical Review A **87**, 049903 (2013).

20. T. Coudreau, B. Douçot, R. Dubessy, D. Andreoli, and P. Milman. *Robust preparation and manipulation of protected qubits using time-varying hamiltonians*. Physical Review Letters, **107**, 030502 (2011).

21. Q. Glorieux, R. Dubessy, S. Guibal, L. Guidoni, J. P. Likforman, T. Coudreau, and E. Arimondo. *Double-Λ microscopic model for entangled light generation by four-wave-mixing*. Physical Review A, **82**, 033819 (2010).

22. R. Dubessy, T. Coudreau, and L. Guidoni. *Electric field noise above surfaces: A model for heating-rate scaling law in ion traps*. Physical Review A, **80**, 031402(R) (2009).

23. S. Removille, R. Dubessy, B. Dubost, Q. Glorieux, T. Coudreau, S. Guibal, J. P. Likforman, and L. Guidoni. *Trapping and cooling of Sr$^+$ ions: strings and large clouds*. Journal of Physics B, **42**, 154014 (2009).

24. S. Removille, R. Dubessy, Q. Glorieux, S. Guibal, T. Coudreau, L. Guidoni, and J. P. Likforman. *Photoionisation loading of large sr+ ion clouds with ultrafast pulses*. Applied Physics B, **42**, 47–52 (2009).

25. N. Sangouard, R. Dubessy, and C. Simon. *Quantum repeaters based on single trapped ions*. Physical Review A, **79**, 042340 (2009).

26. O. Morizot, L. Longchambon, R. Kollengode Easwaran, R. Dubessy, E. Knyazchyan, P. E. Pottie, V. Lorent, and H. Perrin. *Influence of the radio-frequency source properties on rf-based atom traps.* European Physical Journal D, **47**, 209–214 (2008).

Proceedings with peer-review

1. R. Dubessy, C. De Rossi, M. de Goër De Herve, T. Badr, A. Perrin, L. Longchambon and H. Perrin. *Local correlations reveal the superfluid to normal boundary in a trapped two-dimensional quantum gas.* AIP Conference Proceedings, **1936**, 020027 (2018).

2. C. De Rossi, R. Dubessy, K. Merloti, M. de Goër de Herve, T. Badr, A. Perrin, L. Longchambon and H. Perrin. *The scissors oscillation of a quasi two-dimensional Bose gas as a local signature of superfluidity.* Journal of Physics: Conference Series, **793**, 012023 (2017).

Conferences – talks

I list here the conferences where I gave a talk.

1. A fast rotating superfluid on a curved surface. *GDR IQFA 13th Colloquium*, November 2022, Palaiseau, contributed talk.

2. A fast rotating superfluid on a curved surface. *GDR Quantum gases annual workshop*, October 2022, Lille, invited talk.

3. A 2D superfluid on a curved surface. *Prospects of Quantum Bubble Physics*, April 2022, **online workshop**, invited talk.

4. Exploring new regimes with atoms trapped on a curved surface. *Atomtronics@Abu-Dhabi*, June 2021, **online workshop**, invited talk.

5. Universal shock-wave (hydro)dynamics in a 1D Bose gas. *Statistical Physics and Low Dimensional Systems*, October 2020, Pont-à-Mousson, France, invited talk.

6. Superfluid dynamics, collective excitations and extreme rotations of a quasi-two dimensional Bose gas. *6th IEA International Workshop: Physics of Cold Atom Gases: Ordered and Chaotic Aspects*, April 2019, São Paulo, Brazil, invited talk.

7. Dynamics after a current quench in a 1D annular Bose gas. *Low-dimensional Quantum Systems*, November 2018, Vandoeuvre les Nancy, invited talk.

8. Probing superfluidity in a quasi 2D Bose gas through its local dynamics. *International Conference on Quantum Simulators*, November 2017, Paris, contributed talk.

9. Imaging the collective modes of a two-dimensional Bose gas. *Congrès général de la Société Française de Physique*, August 2015, Strasbourg, contributed talk.

10. Fluctuations du champ électrique au voisinage d'une surface métallique. *Colloque de la division de Physique Atomique, Moléculaire et Optique de la Société Française de Physique*, June 2010, Orsay, contributed talk.

Conferences – posters

I list here the conferences where I presented a poster.

1. Fast rotating superfluid on a curved surface. *Finite-Temperature Non-Equilibrium Superfluid Systems*, May 2022, St Martin, Germany.

2. Exploring new regimes with atoms trapped on a curved surface. *BEC – Frontiers in Quantum Gases*, September 2021, Sant Feliu de Guixols, Spain.

3. Barrier induced oscillations and decay of the current in a one-dimensional Bose gas. *European Quantum Technologies Conference*, February 2019, Grenoble.

4. Probing superfluidity in a quasi two-dimensional Bose gas through its local dynamics. *49 th Conference of the European Group on Atomic Systems*, July 2017, Durham, Scotland.

5. Probing superfluidity in a quasi two-dimensional Bose gas through its local dynamics. *Workshop on Many-body Dynamics and Open Quantum Systems*, August 2016, Glasgow, Scotland.

6. Imaging the collective excitations of an ultracold gas using statistical correlations. *BEC – Frontiers in Quantum Gases*, September 2015, Sant Feliu de Guixols, Spain.

7. Towards out of equilibrium dynamics of sodium condensates. *Congrès général de la Société Française de Physique*, August 2015, Strasbourg.

8. Critical rotation of an annular superfluid Bose gas. *The 23rd International Conference on Atomic Physics*, July 2012, Palaiseau.

9. Critical rotation of an annular superfluid Bose gas. *Theory of Quantum Coherence*, June 2012, Lyon.

10. Critical rotation of an annular superfluid Bose gas. *Quantum Science and Technologies*, Mai 2011, Rovereto, Italy.

11. Electric field noise above surfaces: A model for heating-rate scaling law in ion traps. *CLEO-Europe*, June 2009, Munich, Germany.

Introduction

This manuscript summarize my research works during the past ten years in the Bose-Einstein condensate (BEC) group at *Laboratoire de physique des lasers*. I started my scientific career by a PhD thesis on the development of micro-fabricated surface traps for cold ions, in the context of quantum computing and quantum communications, supervised by Luca Guidoni at *Laboratoire matériaux et phénomènes quantiques*. After my defense in 2010, I joined the BEC group, led by Hélène Perrin, for a post-doctoral stay, during which I became familiar with the topic of degenerate Bose gases, both experimentally and theoretically. Two years later I obtained a position as associate professor in the same group.

Overall context

My research work belongs to the domain of ultra-cold quantum gases, that was enabled by the realization of the first Bose-Einstein condensates in 1995 [Anderson *et al.*, 1995; Davis *et al.*, 1995], an achievement recognized by the 2001 Nobel prize in physics [Cornell and Wieman, 2002; Ketterle, 2002]. Since these pioneering times, a lot of groups worldwide managed to reach the BEC threshold with an increasing variety of atoms[1], developing along the way new techniques to trap and cool dilute atomic vapors and enriching the playground of ultracold atom physics. A few years later, the first degenerate Fermi gas was achieved [DeMarco and Jin, 1999] opening a new research direction with fermionic species[2].

Ultracold atom experiments are very demanding but enable the implementation of quantum simulators [Bloch *et al.*, 2012]: by trapping dilute atomic samples in a ultra-high vacuum environment using optical or magnetic forces and cooling them to quantum degeneracy enables the study of fundamental phenomena and the implementation of model Hamiltonian. For example, by tightly confining one or two spatial degree of freedom it is possible to study low dimensional physics [Görlitz *et al.*, 2001], while optical lattices allow to mimic the structure of crystals [Bloch *et al.*, 2008], or Feshbach resonances enable to tune the two-body interactions [Chin *et al.*, 2010]. This lead to the observation of a Bose-Einstein condensate of molecules [Jochim *et al.*, 2003] and stimulated the study of atomic mixtures of any flavor (Bose-Bose, Bose-Fermi or Fermi-Fermi).

[1] by chronological order: Rubidium 6, Sodium 44, Lithium 19, Hydrogen 73, metastable Helium 159, Potassium 146, Cesium 200, Ytterbium 194, Chromium 86, Strontium 188, Calcium 120, Dysprosium 133, Erbium 4 and Europium 145.

[2] by chronological order: Potassium 49, Lithium 180; 196, Ytterbium 74, Dysprosium 132, Erbium 3 and Chromium 154.

Among the long list of impressive experiments that use trapped atomic quantum gases I would like to highlight the quantum gas microscopes [Bakr *et al.*, 2009] that can test the simple theoretical models proposed to explain phase transitions in solid state devices, the observation of a supersolid phase in a quantum gas with dipolar interactions [Natale *et al.*, 2019], the measurement of the equation of state of both Fermi [Nascimbène *et al.*, 2010] and Bose [Desbuquois *et al.*, 2014] quantum gases or the test of the Kibble-Zurek mechanism in a superfluid [Corman *et al.*, 2014]. Closer to the topics I will discuss in this manuscript, several groups have been interested in the dynamical properties of low dimensional Bose gases, as for example the study of the Quantum Newton's cradle in one dimension [Kinoshita *et al.*, 2006; Schemmer *et al.*, 2019], stable breathers [Saint-Jalm *et al.*, 2019] or the emergence of turbulent metastable states [Gauthier *et al.*, 2019] in two-dimensions.

My experimental research activity rely on the adiabatic potential technique [Zobay and Garraway, 2001, 2004] that enables the trapping of ultracold atoms in tunable, smooth, magnetic potentials. This technique is mastered by a few groups worldwide [Garraway and Perrin, 2016] and can be used to create shell shaped potentials [Colombe *et al.*, 2004; Merloti *et al.*, 2013b], realize matter-wave interferometry between two wells [Kim *et al.*, 2016; Mas *et al.*, 2019; Schumm *et al.*, 2005; Sunami *et al.*, 2022] or a ring geometry [Guo *et al.*, 2022; Heathcote *et al.*, 2008; de Goër de Herve *et al.*, 2021; Kim *et al.*, 2016]. Its possibilities can be further enhanced by combining it with time-averaging [Gildemeister *et al.*, 2010; Lesanovsky and von Klitzing, 2007], to realize ring traps [Gildemeister *et al.*, 2012] or guided interferometry [Pandey *et al.*, 2019].

The BEC group

The Bose-Einstein condensate group has been contributing to the study of ultracold atoms for more than 20 years and pioneered in particular the adiabatic potential technique that enables the trapping of quantum gases in very smooth, highly tunable geometries. It currently runs two experimental setups: the *Rubidium* machine is devoted to the study of two-dimensional superfluid dynamics and the *Sodium* machine aiming at controlling the interactions in a one-dimensional system to reach the strongly interacting regime. The former was originally designed to produce ring shaped traps by combining a shell-shaped trap and a optical light-sheet potential, while the latter relies on an atom chip trap to tightly confine the atoms in the vicinity of an embedded micro-wave waveguide.

The group is led by Hélène Perrin, research director at CNRS, who initiated the *Rubidium* experiment, and gathers Aurélien Perrin, researcher at CNRS who is the principal investigator of the *Sodium* experiment, Laurent Longchambon, associate professor in charge of the superfluid ring experiments on the *Rubidium* machine and Thomas Badr, research engineer who develops new tools for both experiments. Vincent Lorent, professor, and Paul-Éric Pottie, research engineer, made decisive early contributions to the *Rubidium* setup, but have since then moved to other topics. Over the years several interns, PhD students and post-doctoral researchers have joined the projects, and I detail their contributions in the following chapters.

When I was hired as associate professor, it was to work on both projects: to finish the works initiated during my post-doc on the *Rubidium* experiment and to contribute to the construction of the *Sodium* experiment. In particular I took part in the design of the atom chip embedding a microwave waveguide and I participated in the realization of the first sodium magneto-optical trap in the group. In parallel I initiated several new projects on the *Rubidium* setup, that I detail in this manuscript and progressively resumed working full time on this experiment. From 2013 to 2020, the *Rubidium* setup was used to investigate the superfluid dynamics in a ring geometry under the supervision of Laurent Longchambon, and in a two-dimensional harmonic trap, under my supervision. Both projects were coordinated by Hélène Perrin. Since 2021, I am the principal investigator on the *Rubidium* experiment. I made the choice to focus in this manuscript on the projects and results in which I had a significative contribution.

Main results of this work

- I participated in the construction of a BEC machine that enabled the realization of the first two-dimensional superfluid trapped in a pure magnetic trap, over which we have a great control;

- I contributed to the study of superfluid dynamics on a curved surface, evidencing the Kosterliz-Thouless transition and reaching for the first time the fast rotation limit;

- I played a part in the study of one-dimensional superfluid rings revealing the role of solitons in the phase-slip dynamics and evidencing the universal features of shock wave propagation in integrable systems.

Overview of the manuscript

The first chapter describes the important details of the experiment going from a hot Rubidium vapor down to a quantum gas. I detail the setup, including the vacuum chamber, the laser sources and the geometry of the coils generating the magnetic traps. I explain the path we follow to reach Bose-Einstein condensation in a hybrid trap and discuss the tools we use to manipulate and probe the ultracold atom sample.

The second chapter details the key features of two-dimensional superfluidity, how we trap the atoms onto a surface using adiabatic potentials and achieve a fine control of the geometry. I summarize the known properties of the two-dimensional superfluid transition and introduce a few simple models that I use to simulate the dynamics of a quasi-two-dimensional Bose gas. I discuss the trap geometry and explain an original method to analyze the dynamics of a superfluid that reveals its collective modes. I also show how a fine tuning of the parameters enables a new geometry for atom trapping.

The third chapter presents original properties of superfluid dynamics on a curved surface, from small oscillations to fast rotations. I report a study of the scissors mode dynamics, that evidences the coexistence of normal and superfluid phases in the ultracold atom sample. I then present how we can spin up the gas and finely control its angular rotation frequency, enabling a study of the melting of a vortex lattice in a quasi-two-dimensional system, induced by thermal fluctuations. I show that it is also possible to reach in our experiment a fast rotation regime in which the gas takes the form of a ring, dynamically sustained by its own angular momentum and resulting in a supersonic flow.

The fourth chapter summarizes several theoretical studies of superfluidity in a one-dimensional ring atomtronic device. I briefly discuss the context of atomtronics and introduce specific tools to deal with the one-dimensional limit, taking advantage of the integrability of the equations. I then report on several works addressing the topics of superfluid transport and dissipation, evidencing the role of shock waves and solitons.

Finally I conclude with an overall discussion of the results and perspectives of future works aiming at probing two-dimensional turbulence. In addition three short appendices give additional technical details on the adiabatic potentials formalism and the thermodynamics in a rotating frame.

I made the choice of a thematic presentation of my works, rather than following chronological order. This may give the impression that I have followed a clear path over the years, which is somewhat artificial. Nevertheless, having now ten years of experience I think that writing this habilitation thesis is a good opportunity to tell a coherent story. I hope that it will be useful for future PhD students or fellow researchers that want an introduction to these works. In particular I tried to keep the mathematical descriptions as simple as possible and give further details in the appendices. I also tried to use a common set of notations throughout the manuscript, therefore some of the formulas may not be written exactly in the same form as in the publications. As it is almost impossible to keep track of all research works currently happening in the quantum gas community I indicated in each chapter recent reviews covering the relevant topics.

List of Figures

List of Symbols

The next list describes several symbols that will be later used within the body of the document. I have tried to use a coherent set of notations throughout the manuscript. I made the choice to write all quantities and equations using physical dimensions.

Acronyms

AOM Acousto-optic modulator

BEC Bose-Einstein condensate

GHD Generalized hydrodynamics

GPE Gross-Pitaevskii equation

MOT Magneto-optical trap

PCA Principal component analysis

Physics constants

$\hbar = \frac{h}{2\pi}$	reduced Planck constant	$1.054\,571\,82 \times 10^{-34}$ J/rad
μ_B	Bohr magnetron	$h \times 1.399\,624\,604$ MHz/G
a_s	low energy s wave scattering length	for ^{87}Rb 5.3 nm
g	gravitational acceleration	9.81 m/s^2
g_F	gyromagnetic factor	for the $F = 1$ groundstate $-1/2$ (-0.70 MHz/G)
k_B	Bolzmann constant	$1.380\,650\,4 \times 10^{-23}$ J/K
M	atomic mass	for ^{87}Rb $1.443\,160\,648 \times 10^{-25}$ kg

Thermodynamical quantities

$\bar{\mu} = \frac{\mu}{k_B T}$ reduced chemical potential

$\Lambda = \sqrt{\frac{2\pi\hbar^2}{M k_B T}}$ thermal de-Broglie wavelength

μ chemical potential

N atom number

T temperature

Dressed trap parameters

α quadrupole trap horizontal magnetic gradient in frequency units

$\ell = \sqrt{\rho^2 + 4z^2}$ quadrupolar length

$\epsilon = \frac{Mg}{2\hbar\alpha}$ gravitational sag

η fraction of rf coupling in the σ^+ polarization

Ω_0 maximum Rabi coupling

ω_r radial trapping frequency

ω_z vertical trapping frequency

ω_{rf} rf dressing frequency

$\omega_{x,y}$ in plane trapping frequency

Θ, Φ angles describing an elliptical polarization

ε in plane anisotropy

b' quadrupole trap horizontal magnetic gradient

r_0 shell trap radius at equator

Bose-Einstein condensate physics

$\tilde{g}$ two-body dimensionless interaction strength in two-dimensions

$\xi = \frac{\hbar}{\sqrt{2M\mu}}$ healing length

ζ eigenvalue of the Lax spectrum

$c = \sqrt{\frac{\mu}{M}}$ speed of sound

$g_{1D} = 2\hbar\omega_r a_s$ two-body dimensionless interaction strength in one-dimension

$g_{3D} = 4\pi\frac{\hbar^2}{M}a_s$ two-body interaction strength

$k_c = Mg_{1D}/\hbar^2$ inverse length scale of the two-body interactions in one-dimension

Other symbols

(ℓ, χ, ϕ) spheroidal coordinates

(ρ, ϕ, z) cylindrical coordinates

(r, θ, ϕ) spherical coordinates

(x, y, z) cartesian coordinates

Chapter 1

Overview of the experiment

The aim of this first chapter is to present the experimental setup that is used by the group to study low dimensional superfluids. It was built during the PhD thesis of [Liennard, 2011] and upgraded during the following theses. I will summarize the main tools we use and focus on details that are necessary for the understanding of the following chapters. I will point out the references where further technical details are given. I assume that the reader is familiar with the basic physics of magneto-optical traps (MOT) and magnetic traps for neutral atoms [Ketterle *et al.*, 1999]. I will also comment on the technical choices we made and discuss the evolutions of the setup in the past ten years.

Contents

1.1 The ultracold atom machine

This first section introduces the Rubidium BEC machine in use at Laboratoire de physique des lasers, focusing on the different lasers we use to trap and cool the atoms and on the coils that generate static and oscillating magnetic fields.

1.1.1 The Rubidium 87 atom

The experiment was designed to cool down Rubidium 87 ensembles. The choice of this particular atom can be motivated by several factors:

- the cooling transition in the near infrared, see figure 1.1, can be obtained by doubling a fiber laser in the telecom frequency range, thus obtaining a reasonable amount of power to operate simultaneously a 2D MOT and a 3D MOT at a moderate cost;

- its level structure is compatible with the use of Nd:YAG laser systems at the fundamental and doubled wavelengths to implement far-detuned optical dipole traps;

- its scattering properties in the electronic groundstate $F = 1$ and $F = 2$ are very favorable, all scattering lengths between Zeeman m_F sublevels being nearly equal and positive.

The last property ensures that the mean-field interaction is not changed when the atoms are transferred into a radio-frequency dressed magnetic potential [Lavoine *et al.*, 2021], which is crucial for our experiment.

1.1.2 The vacuum chamber

The vacuum chamber is made of three parts: a two-dimensional magneto optical trap (MOT), bought from SYRTE; an octagonal metal chamber with four CF-40, two CF-16 and two CF-63 viewports; and a rectangular cuboid glass cell. The cell and all viewports are coated with a anti-reflective coating optimized for wavelengths 780 nm, 532 nm and 1064 nm. As the cell is assembled before coating, only its exterior is coated. This choice of wavelengths is convenient for Rubidium 87, and for the most commonly available high power, far detuned laser systems. A partial pressure of Rubidium is created in the 2D MOT chamber using a small oven heated to about 60 °C. We operate the system with a quite low flux and the Rubidium oven shows no sign of failure after more than ten years of daily operation.

The chambers are pumped by three ion pumps ($2\,\mathrm{L\,s^{-1}}$ for the 2D MOT and $25\,\mathrm{L\,s^{-1}}$ for the others) and separated by two differential pumping tubes. This ensures a very high quality vacuum in the last chamber. Finally a titanium sublimation pump is attached to the last chamber and can be activated if needed. We do not use vacuum gauges, but rely on the current reading on the ion pumps power supplies to monitor the residual pressure. Usually all pump controllers display a reassuring 0 µA value. The chambers are under ultra high vacuum conditions since more than ten years, the only serious alert concerning vacuum happened recently with a small leak on one indium seal on the 2D MOT chamber. It necessitated the use of a turbomolecular pumping bench to detect it and protect the first ion pump and was solved by adding a flange to constrain the leaking seal.

The main drawbacks of this design are related to the intermediate metal chamber that favors Eddy currents when we change rapidly the MOT coils currents. This prevents us

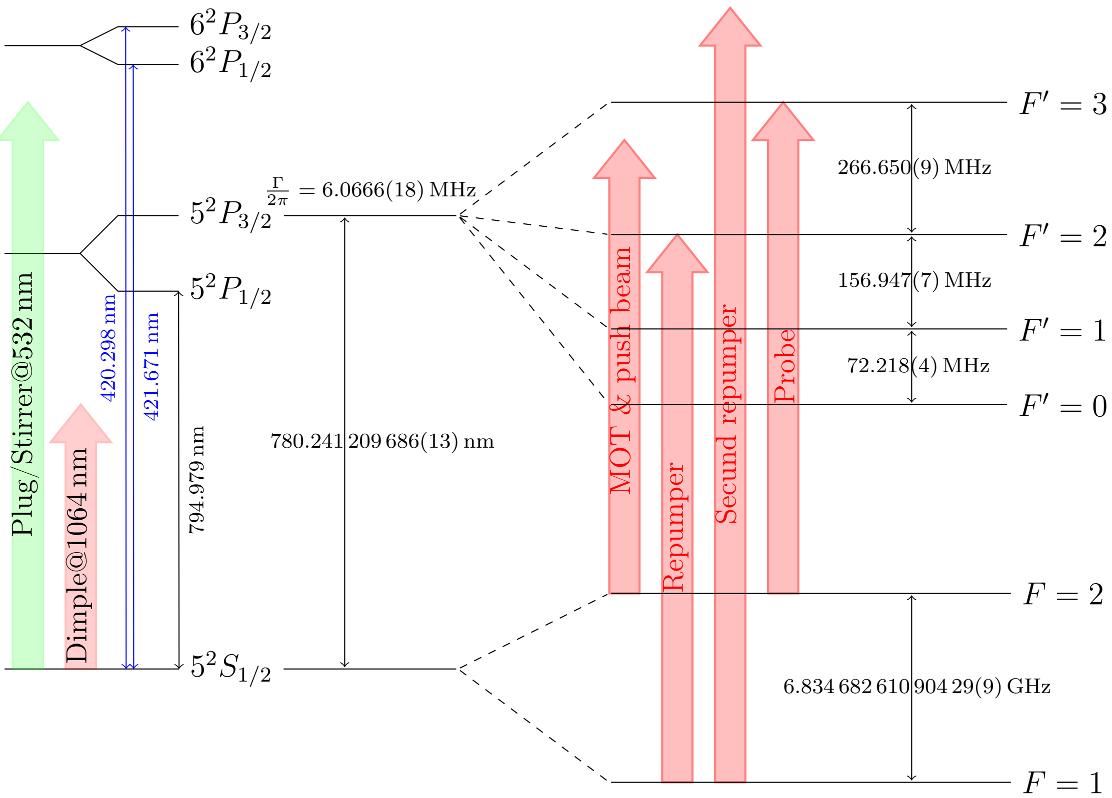

Figure 1.1: Energy levels of the Rubidium 87 atom (directly accessible from the ground state), with a focus on the D_2 line and the lasers used in the experiment. The D_1 and $5S$–$6P$ lines are indicated for reference. The numbers are taken from [Steck, 2021].

to reach very low temperatures during the optical molasses stage and to implement an efficient optical pumping scheme to load the atoms in the $F = 2$ groundstate manifold. Therefore we work in the $F = 1$ manifold and capture only about $1/3$ of the laser-cooled atoms in the magnetic trap for the transport stage and, due to the relatively high temperature we loose a significant part of the cloud on the walls of the differential pumping tube during the transport to the final glass cell [Liennard, 2011].

1.1.3 The laser system

The whole laser system is mounted on two optical tables and boxed to protect it from dust, to avoid air flow from the air conditioner and for laser safety.

Master laser The master laser is a external cavity diode laser, locked onto a saturated absorption signal in a Rubidium vapor cell using a modulation transfer scheme. It produces two resonant probe beams, injected into two optical fibers that are used to perform resonant absorption imaging to measure the atomic cloud density profile at the end of the experimental sequence. The imaging pulses are created with a double-pass acousto-optic modulator (AOM) and are typically 20 µs long. A small part of the master laser light is used to lock the cooling laser with a beatnote on a photodiode.

Cooling laser The cooling laser is a telecom fiber laser amplified up to 10 W and frequency doubled in a single pass PPLN crystal, resulting in about 1 W of light at 780 nm. Its power is controlled by a single pass AOM and it is split in four beams to inject the MOT fibers and the push-beam. The 3D MOT is fed by a 2 to 6 fiber cluster that enables the use of six independent fiber output collimators for the MOT beams. The second input port of the fiber cluster receives a part of the repumper beam.

Repumper laser The repumper laser is a simple laser diode locked onto a saturated absorption signal in a Rubidium vapor cell. It is injected in the 3D MOT fiber cluster, in the two fibers of the 2D MOT and in a additional fiber to repump the atoms during the imaging sequence from the $F = 1$ manifold to the $F = 2$, as the resonant probe beam is tuned to the $F = 2 \to F' = 3$ cycling transition. A small amount of light is used to lock the off-resonant repumper with a beatnote on a fast photodiode.

Off resonant repumper laser In order to image high-density, in situ, samples we use a dedicated repumper beam, centered onto the trap position and with a waist of ~ 1 mm. This is necessary because the intensity of the resonant repumper mentioned in the previous paragraph is too low at the trap position, and this results in a inhomogeneous repumping of the atoms. Indeed this beam is centered ~ 2 mm below the trap position and has a larger waist ~ 4 mm allowing to image clouds after typically 15 to 27 ms of time of flight. To reduce the optical depth seen by the second repumper beam, we use a independent laser diode detuned to the blue of the $F = 1 \to F' = 2$ transition by typically 500 MHz, controlled thanks to a beatnote with the main repumper. This enables the repumping of a controlled fraction of the atoms, without altering the density profile [De Rossi, 2016].

Far detuned optical dipole traps beams To achieve an efficient evaporative cooling in a magnetic quadrupole trap it is necessary to use an auxiliary laser beam to reduce the detrimental impact of Majorana losses. This can be achieved either by using a blue

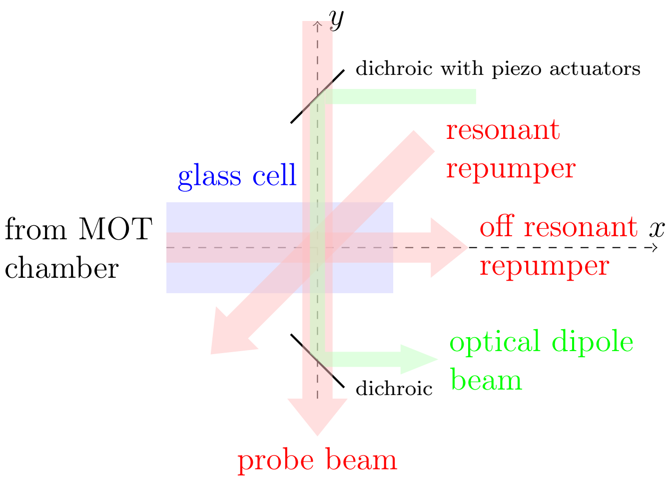

Figure 1.2: Top view sketch of the final glass cell, with all beams in the horizontal plane. Not shown: the vertical probe beam and the stirring/defect beam, propagating downwards along the vertical axis.

detuned optical dipole trap, a plug beam [Davis *et al.*, 1995] or a red detuned optical dimple trap, a dimple beam [Lin *et al.*, 2009]. For historical reasons we started by using a plug beam, produced by a 10 W@532 nm Millenia laser that was available in the group [Merloti, 2013] and replaced after some years by a more compact 10 W@532 nm laser from the ALS company [De Rossi, 2016]. We had a bad experience with this model, especially with failures of the integrated power stabilization scheme. During the downtime of the ALS laser we managed to use a 5 W@532 nm Verdi laser to reach the condensation threshold.

As green high power lasers are quite expansive I suggested to try the dimple beam strategy and implemented recently a 5 W@1064 nm amplified fiber laser system from Keopsys on the experiment [Rey, 2023]. It turned out to be almost as efficient as the plug beam scheme to produce a Bose-Einstein condensate in our experiment and enabled a simpler loading strategy, see section 2.3.2. Both the plug and dimple beams need to be focused down to waists of about 30 to 70 µm, in the vicinity of the quadrupole trap center, which is achieved with a single lens of focal length 200 mm. To achieve a precise control over their position we superimpose their path on the horizontal probe beam path using dichroic mirrors with high transmission at 780 nm and high reflection at 532 nm or 1064 nm and control the orientation of the input dichroic with piezo-electrical elements.

1.1.4 The magnetic traps

MOT and transport The main originality of our setup consists in the magnetic transport that transfers the atoms from the MOT chamber to the final glass cell: the MOT coils are mounted on a translation rail that moves the coils on a distance of 28 cm. To be able to trap the atoms during this transport stage, a large gradient is required. In the present version of the setup, the current flowing in those coils is increased up to 360 A, which requires an efficient cooling. Therefore the coils are made of hollow copper wire in which circulates cold water. Two independent current power supply provide the currents in the two coils. A small imbalance is introduced to maximize the overlap of the cloud position during the transport with the entrance of the differential pumping tube separating the 3D MOT chamber and the final glass cell.

The coils and their support were built during the thesis of [Merloti, 2013] in replacement of the first design [Liennard, 2011] that suffered from several problems: insufficient cooling that limited the maximum current (and gradient), rigid cables that were not easily handled during the transport stage and large eddy currents due to the water cooling elements. The new design solved these problem by using hollow copper wires and a conveyor belt system that guides the cables and water cooling pipes during the translation, at the cost of an increased current (from 40 A to 400 A). The horizontal magnetic field gradient of the transport quadrupole coils is 0.25 G/cm/A [Merloti, 2013].

This transport system has been running smoothly for more than 10 years doing between 100 and 300 round trip per day, at each run of the experiment. We had to replace once the motor of the translation stage, which can be done in situ without unmounting the coils. Finally the main disagreements we encountered over the year were several water leaks on the watercooling system, probably due to the constrains accumulated by the back and forth movement of the conveyor belt. This was solved by using more flexible water pipes that are less prone to pull on the connections.

Science quadrupole trap The science quadrupole trap coils are two conical coils made of hollow copper wire, build and assembled during the thesis of [Liennard, 2011]. They produce a horizontal gradient of about 1.98 G/cm/A and are typically operated with currents in the range 28 to 110 A, provided by a single power supply. A specially designed high current switch system, based on high power IGBT transistors and Zener diodes enables a fast switching of the current in the coils (the magnetic field reaches 10% of its initial value in about 350 µs). This is important to release suddenly the atoms held in the trap and perform time of flight expansions.

Compensation coils The whole vacuum chamber is surrounded by three pairs of meter-scale square coils used to compensate the Earth magnetic field at the position of the 3D MOT. The currents in those coils are switched off after the transport stage and a set of two pairs of rectangular coils (10 by 5 cm) are then used to create a homogeneous magnetic field component in the y and z directions near the glass cell center. These coils are used to compensate stray magnetic fields at the final quadrupole trap position, such that the position of the trap does not move when the gradient changes, or produce homogeneous magnetic fields during the imaging sequence. The residual magnetic field along the x direction is very small as it is orthogonal to the Earth magnetic field direction.

radio-frequency coils Finally, a few coils are placed in the vicinity of the glass cell that we use to apply radio-frequency signals to the atoms to induce controlled spin flip transitions between the Zeeman states of the $F = 1$ groundstate manifold: this enables the possibility of performing rf evaporation, rf spectroscopy and, last but not least, rf dressing. In particular we use a set of three coils, with mutually orthogonal axis to fully control the polarization of the rf field.

Figure 1.3 displays a sketch of the quadrupole and dressing coils around the final glass cell. We expect that the atoms in the dressed trap will be located at a position where the static quadrupole magnetic field defines a vertical quantization axis and therefore we want to produce a rf dressing field with arbitrary in plane polarization:

$$\boldsymbol{B}_{\mathrm{rf}}(t) = B_{\mathrm{rf}} e^{i\omega_{\mathrm{rf}} t} \left(\cos\left[\Theta\right] \boldsymbol{e}_x + \sin\left[\Theta\right] e^{i\Phi} \boldsymbol{e}_y\right) + c.c. \tag{1.1}$$

Indeed, a π polarized component along z does not contribute usefully to the dressing potential, see appendix B for a detailed discussion. As is clear from Figure 1.3, an atom moving on the isomagnetic surface will experience a position dependent coupling to the

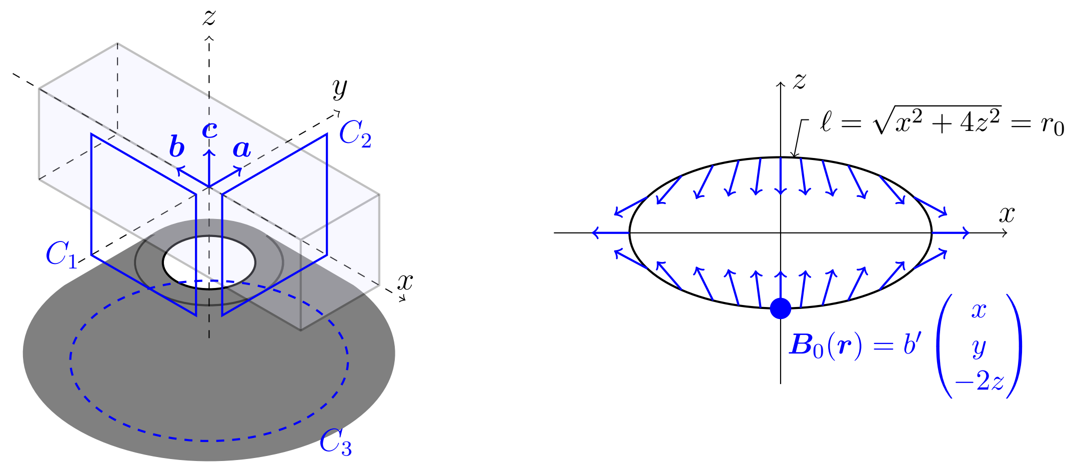

Figure 1.3: Left: sketch of the arrangement of the three dressing coils C_1, C_2 and C_3 around the glass cell (light blue rectangular cuboid). The dark cone gives the shape of the bottom quadrupole trap coil, the upper one is not shown. Right: sketch of one isomagnetic surface of the quadrupole field in a vertical plane, showing the expected ellipsoidal shape. The blue arrows indicate the local direction of the quadrupole magnetic field on the surface and the blue disk corresponds to the equilibrium position of the atoms in the dressed trap.

rf field, due to the change of the local quantization axis imposed by the static quadrupole field. This has important consequences, as detailed in section 2.4.

To achieve the desired polarization we use a set of three coils C_1, C_2 and C_3 fed with three independent phase coherent signals generated by a dedicated DDS device. Close to the center of the trap each dressing coil creates a locally homogeneous field directed along one of the units vector $\boldsymbol{a}$, $\boldsymbol{b}$ and $\boldsymbol{c}$. Because of possible misalignment of the coils, those vectors are close but not equal to the basis vectors $(\boldsymbol{a}, \boldsymbol{b}, \boldsymbol{c}) \simeq (\boldsymbol{e}_y, -\boldsymbol{e}_x, \boldsymbol{e}_z)$ and the field is:

$$\boldsymbol{B}_{\mathrm{rf}}^{\mathrm{exp}}(t) = B_1 \cos[\omega_{\mathrm{rf}} t]\, \boldsymbol{a} + B_2 \cos[\omega_{\mathrm{rf}} t + \varphi_2]\, \boldsymbol{b} + B_3 \cos[\omega_{\mathrm{rf}} t + \varphi_3]\, \boldsymbol{c}. \tag{1.2}$$

A lengthy but straightforward calculation shows that it is possible to map exactly equation (1.2) onto (1.1), up to a global irrelevant phase, by fine tuning the five parameters $(B_1, B_2, B_3, \varphi_2, \varphi_3)$.

For example, assuming that the misalignment is small, i.e.

$$\begin{aligned} \boldsymbol{a} &= \cos[\theta_a]\, \boldsymbol{e}_y + \sin[\theta_a] (\cos[\phi_a]\, \boldsymbol{e}_x + \sin[\phi_a]\, \boldsymbol{e}_z) \\ \boldsymbol{b} &= -\cos[\theta_b]\, \boldsymbol{e}_x + \sin[\theta_b] (\cos[\phi_b]\, \boldsymbol{e}_y + \sin[\phi_b]\, \boldsymbol{e}_z) \\ \boldsymbol{c} &= \cos[\theta_c]\, \boldsymbol{e}_z + \sin[\theta_c] (\cos[\phi_c]\, \boldsymbol{e}_x + \sin[\phi_c]\, \boldsymbol{e}_y), \end{aligned}$$

with $\theta_a, \theta_b, \theta_c$ small angles, the optimal parameters are:

$$\begin{aligned} \varphi_2 &= \pi - \Phi + (\theta_b \cos[\phi_b] \cot[\Theta] - \theta_a \cos[\phi_a] \tan[\Theta]) \sin[\Phi], \\ B_1 &= B_{\mathrm{rf}} (\sin[\Theta] + \theta_b \cos[\phi_b] \cos[\Phi] \cos[\Theta]), \\ B_2 &= B_{\mathrm{rf}} (\cos[\Theta] - \theta_a \cos[\phi_a] \cos[\Phi] \sin[\Theta]), \\ e^{i\varphi_3} B_3 &= B_{\mathrm{rf}} \left(e^{-i\Phi} \theta_b \sin[\phi_b] \cos[\Theta] - \theta_a \sin[\phi_a] \sin[\Theta]\right). \end{aligned}$$

These equations show how a small misalignment can be compensated by tuning the DDS parameters. In the experiment we only need to fine tune these parameters when we realize a trap with perfect rotational invariance to study fast rotating Bose gases.

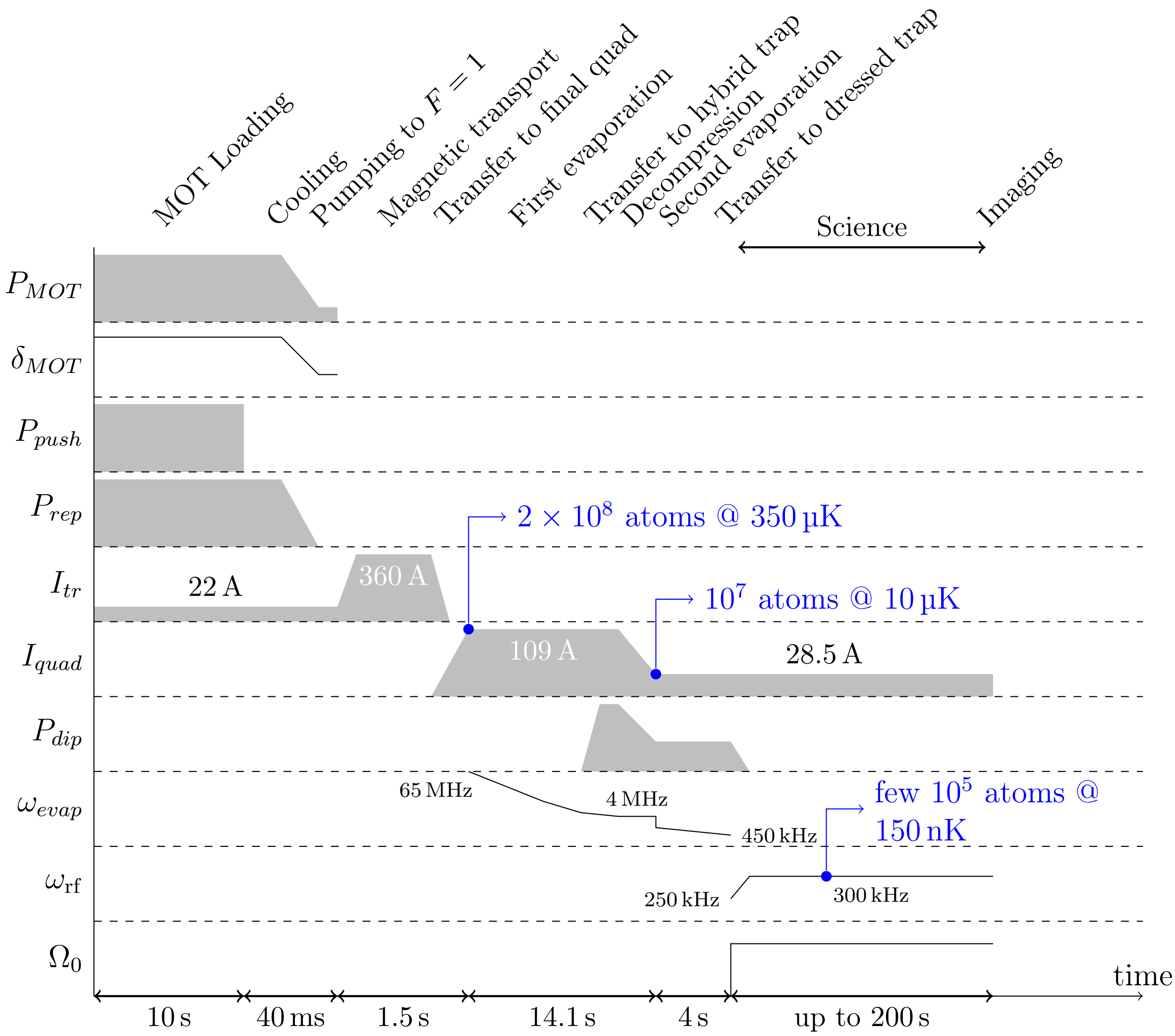

Figure 1.4: Summary of the experimental sequence, with orders of magnitude of the currents, frequencies and times typically used in the current setup [Rey, 2023]. Slight variations were used in the older versions of the setup, because other components were in use (lasers, coils, power supplies, ...), however the time scales, atom numbers and temperatures were similar.

1.2 The sequence

Each run of the experiment consists in preparing a ultracold sample of a weakly interacting dilute Bose gas containing a few 10^5 ^{87}Rb atoms at a typical temperature of 100 nK, at equilibrium in a radio-frequency dressed trap. We study then its dynamics by applying a perturbation, waiting for some evolution time in the trap and performing a measurement. A typical sequence is summarized on figure 1.4: several instruments (lasers, power supplies, signal generators) need to be operated simultaneously, with an accurate synchronization over relatively long times.

This is achieved by using dedicated electronic cards from National Instruments providing programmable analog and digital outputs, controlled by a computer program. In short, a sequence file specifies the values of the different outputs at different times, using a simple programming language; this file is parsed and converted in a table of values that is stored in memory. A dedicated electronic circuit then reads the numerical values and convert them to voltages on the cards outputs at each cycle of a clock signal. For a long time we relied on the `Manip` program, written in Borland C++ by Florian Schreck and slightly modified to adapt to our needs. It is efficient, simple to use and reliable but suffers from two main limitations: first it relies heavily on the Borland C++ API and thus compiles only on Windows Xp systems, which is an issue to ensure the long term support of the experiment, and second it uses a regular sample clock signal, which requires a value for all the outputs at each cycle, even when the outputs does not change. As a consequence the memory requirements are quite large and the resolution of the clock signal is limited to 100 µs.

During the thesis of [Rey, 2023] we upgraded both the hardware and the software of the experiment control system. We now use the `Labscript` software suite and a National Instrument PXI rack system with 64 digital outputs and 32 16-bits analog outputs. The software is written in python, works on any operating system (Windows, MacOS or Linux) and use a smart programming model: it stores only the changes of values and uses a synchronization signal to update the outputs at the desired times. this requires a dedicated micro-controller board that generate this synchronization clock. This programming model allows to benefit from the full 400 kHz refresh rate of the analog output cards while being able to run long sequences (up to 300 s).

1.2.1 MOT loading

To load the MOT, we operate the 2D MOT with about 70 mW of cooling beam power in each of the two beams (at the output of the fibers), red detuned by 3Γ with respect to the $F = 2 \to F' = 3$ cycling transition and a few mW of repumping beam power, at resonance with the $F = 1 \to F' = 2$ transition. The remaining power of the cooling laser is injected in the 3D MOT fiber cluster: about half the power is put in the vertical beams and the other half is split among the four horizontal beams. The 3D MOT is operated with a gradient of 5.5 G/cm. The detunings of the beams are the same for both MOTs. To increase the loading rate of the 3D MOT a few hundreds of µW are used as a push beam along the tube connecting the two chambers. The typical loading rate of the 3D MOT is 10 to 20 s, which is quite slow, compared to other setups where it occurs one order of magnitude faster. The lifetime of the atomic cloud trapped in the 3D MOT is 30 s, limited by background collisions

In order to load the magnetic trap, we use a standard MOT compression scheme, followed by a molasses stage. We then turn off first the repumper beam to accumulate atoms in the $F = 1$ manifold and then the cooling beams, just before increasing the gradient to its maximum value to capture the cloud in the magnetic trap. What is lacking in this sequence is an optical pumping stage: we could not implement it because of large Eddy currents arising when switching the magnetic field from the quadrupole to a homogeneous field configuration. Therefore we are able to load only about 30 % of the atoms in the magnetic trap. This lack of optical pumping also explains why we use the $F = 1$ manifold to produce the BEC: when we tried loading the $F = 2$ manifold we always get a significative fraction of atoms in the $F = 2, m_F = 1$ state, which leads to detrimental losses induced by inelastic collisions during the evaporation stage.

1.2.2 Magnetic transport

The kinematics of the transport are fully determined by the target distance of about 28 cm and the control of the jerk (third order time derivative of the position) during the acceleration and deceleration phases. We use a pre-loaded transport sequence with 8 steps of equal time and a jerk of $j_0 = \pm 25\,\mathrm{m/s^3}$, leading to a transport time of $\Delta T = 8(D/(10|j_0|))^{1/3} \simeq 0.83\,\mathrm{s}$, a maximum acceleration $|a_{\max}| = |j_0|\Delta T/8 \simeq 2.6\,\mathrm{m/s^2}$ and velocity $v_{\max} = 2|j_0|(\Delta T/8)^2 \simeq 0.54\,\mathrm{m/s}$. This results in a relatively fast transport without any noticeable center of mass excitation at the final position.

The main limitation during the transport is given by the overlap of the transverse size of the cloud with the 4 mm inner diameter of the differential pumping tube: even when we carefully align the transport axis with the tube direction, we always record losses during the transport. We attribute these losses to the fact that atoms on the edges of the cloud are lost when they hit the walls of the chamber. It turns out that these losses also help cooling the cloud during the transport as, on average, the most energetic atoms are lost. The horizontal rms size of a thermal cloud held in a quadrupole trap is $\Delta x \simeq 2k_BT/(\hbar\alpha)$. At the end of the transport the temperature is about 200 µK, for a gradient of 90 G/cm, resulting in a size of about 1.3 mm, compatible with this explanation. We estimate that only 40 % of the atoms loaded in the magnetic transport trap are transferred to the final chamber. However this low efficiency does not prevent us to reach condensation.

To minimize these losses, one can think of adiabatically compressing the trap to reduce the rms size. Indeed the phase space density scales as $\alpha^3/T^{9/2}$ in a quadrupole trap, and if the gradient increases from α_0 to α_1, the rms size should follow the scaling: $\Delta x_1/\Delta x_0 = (\alpha_0/\alpha_1)^{1/3}$. This is not very favorable as doubling the gradient only results in a reduction of about 20 % of the rms size. Another possibility would be to reduce the temperature by evaporative cooling before the transport. In our experiment the elastic collision rate is too small compared to the typical losses due to background collisions in the MOT chamber for evaporation to be efficient at this stage.

1.2.3 Evaporation

In the glass cell we transfer the atoms in the final quadrupole trap and increase the gradient adiabatically to 216 G/cm, leading to a higher temperature of 350 µK. We then use a radio-frequency signal fed to a 4 cm, few loops, coil antenna, through a 5 W amplifier to induce splin flips between the Zeeman sublevels of the F=1 manifold and perform evaporation. We start at a frequency of 65 MHz, truncating the trap at a energy of $k_B \times 3\,\mathrm{mK}$, much higher than the initial temperature and then ramp down the frequency to 4 MHz. This results in an efficient evaporation, with a phase-space density scaling as $N^{-3.1}$, down to a temperature of about 20 µK, as shown in figure 1.5 [Dubessy *et al.*, 2012b]. However at this point Majorana losses limit the rf evaporation and one has to use a mitigation strategy.

In our case we choose to rely on a hybrid quadrupole plus optical dipole beam trap to reduce Majorana losses. We first tried a blue detuned repulsive plug beam [Dubessy *et al.*, 2012b], a strategy that was successful for many years, and more recently implemented a red detuned attractive dimple trap [Rey *et al.*, 2022]. In short we turn on the optical trap during the evaporation ramp and when Majorana losses become too important we open the quadrupole trap by decreasing the gradient to 56 G/cm. We then resume the evaporation ramp from 2 MHz to 450kHz which gives samples with several 10^5 atoms at a temperature of about 250 nK. Both methods allow to reach Bose-Einstein condensation

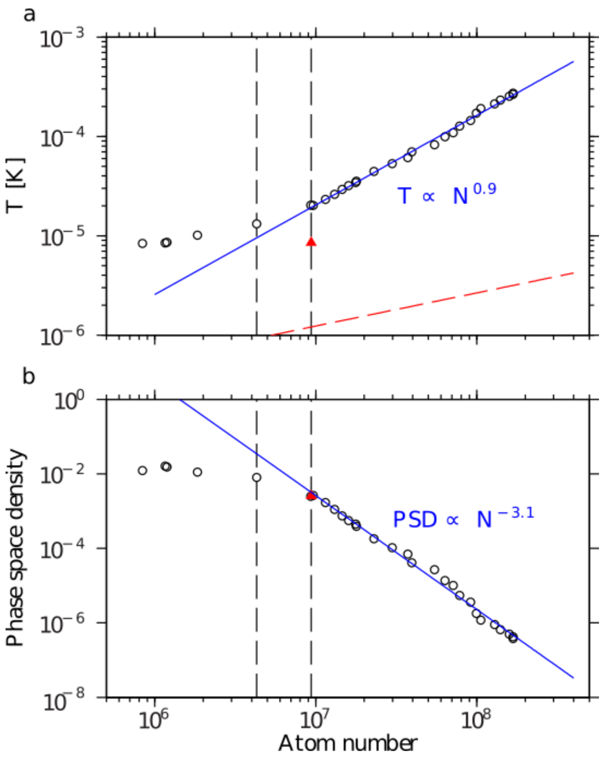

Figure 1.5: Evaporation efficiency in a bare quadrupole trap of gradient $b' = 216\,\mathrm{G/cm}$. a) Temperature and b) phase space density versus atom number, in log-log scale. The solid blue lines are power law fit to the data. Below 10^7 atoms the evaporation efficiency is lower, because of increased Majorana losses at $T \leq 20\,\mu\mathrm{K}$. The red symbols correspond to the temperature and phase space density after a adiabatic decompression of the quadrupole trap to $b' = 55\,\mathrm{G/cm}$, this lowers the Majonara losses and gives a good starting point for the final evaporation ramp in the hybrid trap.

with similar atom numbers and temperatures.

Finally we transfer the atoms into the adiabatic potential by turning on a strong rf field while decreasing the optical power. I will discuss in detail the loading protocol and the properties of the adiabatic potential in section 2.3.2.

1.3 Tools and diagnosis

Once the atoms are loaded in the adiabatic potential the sample is ready and the real science begins. As we are interested in studying the superfluid response of the cloud, we developed specific tools to probe and measure its dynamics.

1.3.1 Eight channel DDS

The main tool we developed in the laboratory, thanks to the support of the electronic workshop and specifically of Fabrice Wiotte, is a phase coherent eight outputs, fast, agile and fully programmable DDS. It is based on two four outputs DDS devices (AD9959), fed by a common 10 MHz clock and driven by a micro-controller unit (TM4C123). The DDS clocks are scaled up to 500 MHz using internal phase-locked loops. The micro-controller programs the two DDS using dedicated serial peripheral interfaces and achieves a refresh rate between 100 kHz and 1 MHz, limited by its internal 80 MHz clock. The outputs of the DDS are amplified by wide band instrumentation amplifiers up to a maximum power of 20 dBm and controlled by a fast rf switch.

Each output delivers a signal of the form $A \cos\left[\omega_{\mathrm{rf}} t + \phi\right]$, where the amplitude A is programmable with 10 bit resolution, the frequency ω_{rf} with 32 bit and the phase ϕ with 14 bit. To fully reconfigure one of the outputs 14 bytes of data must be sent to the DDS and the communication bus provides a 56 Mbytes data transfer rate, limited by the micro-controller clock frequency. Using three of the outputs we obtain a fully controllable rf field at the center of the quadrupole trap (1.2), that we tune to achieve the desired rf polarization (1.1). This results [Garraway and Perrin, 2016; Perrin and Garraway, 2017] in a rf-atom coupling in a quadrupole trap of the form:

$$\Omega(\boldsymbol{r}) = \frac{\Omega_0}{\sqrt{2}}\left(1 - \frac{\rho^2 + (x^2-y^2)\cos[2\Theta] + 2xy\sin[2\Theta]\cos[\Phi]}{2\ell^2} - \frac{2z}{\ell}\sin[2\Theta]\sin[\Phi]\right)^{1/2}, \tag{1.3}$$

where $\ell^2 = \rho^2 + 4z^2$, $\rho^2 = x^2 + y^2$ and Ω_0 is the maximum coupling, achieved for a circular polarization with $\Theta = \pi/4$ and $\Phi = \pi/2$.

Interestingly, equation (1.3) is isotropic in the (x, y) plane, except for the term $(x^2 - y^2)\cos[2\Theta] + 2xy\sin[2\Theta]\cos[\Phi]$, that can be written as $-2\sqrt{\eta(1-\eta)}(x'^2 - y'^2)$, where

$$\eta = \frac{1 + \sin[2\Theta]\sin[\Phi]}{2} \tag{1.4}$$

quantifies the fraction of the rf field that contributes to the coupling and the rotated frame is defined by

$$\begin{aligned} x' &= \cos[\phi']\,x + \sin[\phi']\,y, \\ y' &= \sin[\phi']\,x - \cos[\phi']\,y, \end{aligned}$$

where the angle of the rotated frame is:

$$\tan[\phi'] = \frac{\cos[\Phi]\sin[2\Theta]}{\cos[2\Theta] - \sqrt{1 - \sin[2\Theta]^2\sin[\Phi]^2}}. \tag{1.5}$$

Finally the coupling can be written as:

$$\Omega(\boldsymbol{r}) = \frac{\Omega_0}{\sqrt{2}}\left(1 - \frac{\rho^2 - 2\sqrt{\eta(1-\eta)}(x'^2 - y'^2)}{2\ell^2} - \frac{2z}{\ell}(2\eta - 1)\right)^{1/2}. \tag{1.6}$$

Equation (1.6) is very helpful to adjust the adiabatic potential properties: it becomes perfectly isotropic in the (x, y) plane for a pure circular polarization $\eta = 1$, which corresponds also to the maximum coupling, it is maximally anisotropic for a linear polarization $\eta = 1/2$, and to achieve a specific configuration, corresponding to a given couple (η, ϕ'), the DDS parameters can be found by inverting equations (1.4) and (1.5):

$$\begin{aligned} \Theta &= \frac{1}{2}\arccos\left[2\sqrt{\eta(1-\eta)}\cos[2\phi']\right], \\ \Phi &= \arccos\left[2\sqrt{\eta(1-\eta)}\frac{\sin[2\phi']}{\sin[2\Theta]}\right]. \end{aligned}$$

In particular it means that the trap axis can be rotated while keeping constant the oscillation frequencies.

The eight channel DDS was implemented during the thesis of [de Goër de Herve, 2018] and its integration in the computer controlled sequence was improved recently [Rey, 2023]. In prior works we used a simpler version with only two independent channels fed to the C_1 and C_2 coils, which did not allow a full control of the polarization.

1.3.2 Imaging

To probe the atomic cloud we use absorption imaging, along two axes: a probe beam propagating along the y axis, imaged with two lenses onto a camera (Andor - iXon) achieving a magnification of $G_h = 2.17$ and a probe beam propagating along the z axis, images with four lenses onto a camera (Andor - Luca) and a magnification of $G_v = 7.8$.

The horizontal imaging system is primarily intended to measure the density distribution after a time-of-flight expansion to extract the atom number, the condensed fraction and the temperature. The circularly polarized probe beam, with waist 2.7 mm, is therefore aligned below the trap position, with a 2.5 mm offset, such that the cloud is properly imaged with time-of-flights in the range 10 to 30 ms. During the imaging pulse we use a small homogeneous 1.9 G magnetic field along y to define the quantization axis and we tune the probe frequency to the $F = 2, m_F = 2 \to F' = 3, m_{F'} = 3$ cycling transition. We use a 17 µs long pulse to avoid blurring by atomic motion during the interrogation time. Just before the probe pulse we send a resonant 100 µs repumper pulse tuned to the $F = 1 \to F' = 2$ transition to repump the atoms in the $F = 2$ manifold.

The vertical imaging system is intended to measure the density distribution either in situ or after a time of flight: the whole camera-objective system is mounted onto a 3-axis translation stage to position the object plane at the desired position. Due to the moving transport coils, the first lens of the objective is always 10 cm away the atoms, resulting in a low numerical aperture NA$\sim$ 0.1, which limits the optical resolution to 4 µm and ensures a deep of field of 100 µm. For in situ imaging, the sample is quite dense and to avoid problems with the repumper pulse, we use a dedicated beam, propagating along x, with a higher intensity and detuned by 500 MHz from the $F = 1 \to F' = 2$ transition. It allows to repump uniformly a controllable fraction of the cloud without altering the density profile. The probe beam is circularly polarized, with a waist of 0.7 mm, and lasts for 20 µs.

For both imaging systems we adjust the peak intensity of the probe to exploit the full dynamic range of the camera. To take into account the inhomogeneous density profile of the probe beams, we calibrated the efficiency of each cameras in terms of photons per count, and deduce the density profile from [Reinaudi *et al.*, 2007]:

$$\sigma_0 n(x, y) = -c^* \ln \left[\frac{I_t(x, y) - I_d(x, y)}{I_r(x, y) - I_d(x, y)} \right] + \frac{I_t(x, y) - I_r(x, y)}{I_{\text{sat}}}, \tag{1.7}$$

where $n(x, y)$ is the atomic density profile integrated along the line of sight, σ_0 is the resonant absorption cross-section, c^* is a dimensionless parameter that can be self-consistently calibrated, $I_t(x, y)$ is the transmitted intensity profile, $I_r(x, y)$ is the reference intensity profile, $I_d(x, y)$ is the stray background light and I_{sat} is the saturation intensity of the cycling transition. A detailed discussion of this implementation in our setup is given in [De Rossi *et al.*, 2016]. To evaluate equation (1.7) we record the three pictures in a row. To obtain an accurate reference intensity profile we use a fringe removal algorithm using a bank of 50 reference images continuously updated at each run of the experiment [Ockeloen *et al.*, 2010].

1.3.3 Additional beams

Even though we rely heavily on the DDS to control and dynamically change the trap properties, we cannot achieve arbitrary potentials and specifically induce a local perturbation on a small fraction of the cloud. This is for example needed if one wants to put an obstacle on top of the trapping potential, to study the dissipation of a flow. To achieve this, Thomas Badr developed a laser stirrer, based on a repulsive optical beam (few mW at 532 nm), tightly focused to a waist of about 10 µm and controlled by two crossed AOMs, fed by a dedicated 2 channel DDS device. It is mixed with the path of the vertical probe beam using a 2 inches dichroic mirror and allows to add a controllable obstacle in the (x, y) plane. It has been used for example in the theses of [de Goër de Herve, 2018] and [Guo, 2021] to induce rotation in a ring-shaped Bose-Einstein condensate, as an alternative approach to the method I present in section 3.2.1.

As mentioned in the introduction, the setup can also produce ring traps by combining the adiabatic potential with a horizontal light sheet dipole trap, as proposed in [Morizot *et al.*, 2006] and realized in [Heathcote *et al.*, 2008; de Goër de Herve *et al.*, 2021]. This is achieved by using a $0 - \pi$ phase plate in the path of an elongated Gaussian beam, to create an intensity profile with a node, tightly confining the atoms in the horizontal plane. For this beam we use the 5W Verdi laser and the optical bench was developed during the theses of [De Rossi, 2016; de Goër de Herve, 2018] and [Guo, 2021] under the supervision of Laurent Longchambon. I contributed to this project mainly by studying theoretical proposals and performing numerical simulations, detailed in chapter 4.

Finally we investigated the possibility of adding arbitrary potentials by imaging a specific light pattern onto the atoms. Thomas Badr and Avinash Kumar, post-doc in the group at that time, tested on a separate bench both a spatial light modulator and a digital micro-mirrors device, by imaging the pattern onto a CCD camera. They used an optimization algorithm with a feedback loop to achieve the desired patterns. This possibility has not been implemented onto the experiment yet, but will certainly be in the future.

Conclusion

In this chapter I described the setup we use to study weakly interacting Bose gases in quasi two-dimensional geometries, as reported in the following chapters. It routinely produces ultracold atom samples of typically a few 10^5 atoms at a temperature below 200 nK, in approximately 30 s. The setup relies on a three chamber design, with a magnetic transport stage based on moving coils, which enables a very high quality vacuum in the final glass cell resulting in a typical lifetime above 120 s in the dressed trap. As I explained this complex chamber design prevents us to perform efficient optical pumping at the end of the MOT, resulting in a small overall transfer efficiency, from the MOT to the final magnetic trap. I think that this does not hinder the performances of the setup, although a better collection efficiency would allow to reduce the experiment cycling time. However, as I will show in chapter 3, the experiment cycle time may also be limited by other factors. Therefore, instead of trying to reduce the cycle time, we are thinking of trying to get as many information as possible from a single experiment.

I suggested that we try to apply a non destructive imaging scheme to measure the in situ density profile of our samples. The idea is to use a probe beam far detuned from the imaging transition, typically a few hundreds of MHz, such that the atomic sample behaves as a phase object: the information is then encoded in the diffraction pattern of the probe beam. One way to recover the atomic sample density profile is to measure this diffraction pattern after a short propagation distance and use a reconstruction algorithm to infer the shape of the diffracting phase object [Wigley *et al.*, 2016]. As the absorption remains low, thanks to the large detuning, this process can be repeated to take several pictures of the density profile. This would be extremely useful to study the dynamics of a ultracold Bose gas, as a movie of the in situ dynamics could be recorded before releasing the atoms and taking a last time-of-flight picture to calibrate the atom number and temperature. We estimate that it should be possible to take at least 10 pictures in a row while preserving a reasonable signal to noise ratio. This improvement will by implemented during the PhD of Rishabh Sharma that I co-supervise with Hélène Perrin.

In order to have more flexibility in the choice of laser detunings for the different beams, and in particular to perform non-resonant imaging, we are upgrading our 780 nm laser chain by locking all the lasers to a master laser using beatnotes. This will enable new opportunities and we think that it will also improve the stability of the experiment. Finally we are considering adding a microwave antenna, tuned to the ^{87}Rb hyperfine transition at ~ 6.8 GHz to transfer the atoms from the $F = 1$ to the $F = 2$ manifold in the final trap [Barker *et al.*, 2020; Bentine *et al.*, 2020, 2017].

Chapter 2

Two-dimensional superfluids

This chapter aims at introducing the key properties of superfluidity in two-dimensional systems, namely the existence of a critical phase-space density above which the superfluid transition occurs, and its observation with trapped weakly interacting ultracold atomic Bose gases held in highly oblate traps. I discuss the different models that we use to interpret the experiments and show how we reach the quasi two-dimensional limit in our experiment using a adiabatic potential in which the atoms are naturally trapped onto a surface. Finally I discuss how the curvature of the shell trap surface can be used to realize new two-dimensional trapping geometries.

Contents

2.1 Context: ultra-cold atoms in *flatland*

I present in this section the main tools that are now used by many groups to characterize quasi two-dimensional ultracold atomic samples, since the pioneering work of [Esslinger and Blatter, 2006; Hadzibabic *et al.*, 2006]. A comprehensive review of this topic can be found in [Hadzibabic and Dalibard, 2013].

2.1.1 The Kosterlitz-Thouless transition

As is well known, the homogeneous ideal Bose gas in three dimensions undergoes a Bose-Einstein condensate (BEC) phase transition when the phase space density $\mathcal{D} = n\Lambda^3$ exceeds a critical value: $\mathcal{D}_c = \zeta(3/2) \simeq 2.61$, in the thermodynamic limit where N and $L \to \infty$ at constant density $n = N/L^3$. For a weakly interacting Bose gas the transition still occurs, and because of the interactions the BEC is superfluid. In two dimensions the situation is very different: there is no BEC phase transition for the homogeneous ideal gas, while a weakly interacting Bose gas undergoes a Kosterlitz-Thouless transition to a superfluid phase, with a universal jump of the two-dimensional superfluid phase space density at the transition from 0 to 4. The absence of Bose-Einstein condensation can be understood by the increased role of thermal fluctuations in low dimensional systems that generically prevents phase coherence at large distances [Hohenberg, 1967; Mermin and Wagner, 1966].

A landmark experiment, using a thin film of Helium-4 adsorbed on a surface, allowed to test quantitatively the predictions of the Kosterliz-Thouless theory and confirmed the jump of the superfluid density at the transition [Bishop and Reppy, 1978]. Interestingly this was measured as a shift of the resonance frequency of a torque oscillator attached to the surface: indeed superfluidity manifests only in the dynamical properties of the fluid. Other diagnosis include the measurement of first and second sounds in a superfluid [Gałka *et al.*, 2021] or the direct evidence for the existence of a critical velocity [Desbuquois *et al.*, 2012].

Estimation of the critical point In the vicinity of the two-dimensional superfluid transition, the equation of state of an homogeneous weakly interacting Bose gas was computed using quantum Monte-Carlo methods, resulting in an estimation of the critical phase-space density and reduced chemical potential [Prokof'ev *et al.*, 2001]:

$$\mathcal{D}_c = \ln\left[\frac{380 \pm 2}{\tilde{g}}\right] \text{ and } \bar{\mu}_c = \frac{\tilde{g}}{\pi}\ln\left[\frac{13.2 \pm 0.4}{\tilde{g}}\right], \tag{2.1}$$

where $\tilde{g}$ is the dimensionless two-body interaction strength. Importantly, the equation of state can be written in the universal form [Prokof'ev and Svistunov, 2002]: $\mathcal{D} = \mathcal{D}_c + F((\bar{\mu} - \bar{\mu}_c)/\tilde{g})$, where $F(x)$ is a universal function, and $\bar{\mu} = \mu/(k_B T)$ is the ratio of the chemical potential to the temperature. Close to the superfluid transition the gas is also characterized by reduced density fluctuations that can be attributed to the existence of a non negligible quasi-condensate fraction.

Figure 2.1 shows the equation of state of the two-dimensional superfluid transition for $\tilde{g} = 0.1$, compared to simple analytical models. The fluctuating region where mean-field predictions are inaccurate is roughly of size $|X| \leq 1$, where $X = (\bar{\mu} - \bar{\mu}_c)/\tilde{g}$ vanishes at the critical point. For X large and negative the ideal Bose gas equation of state

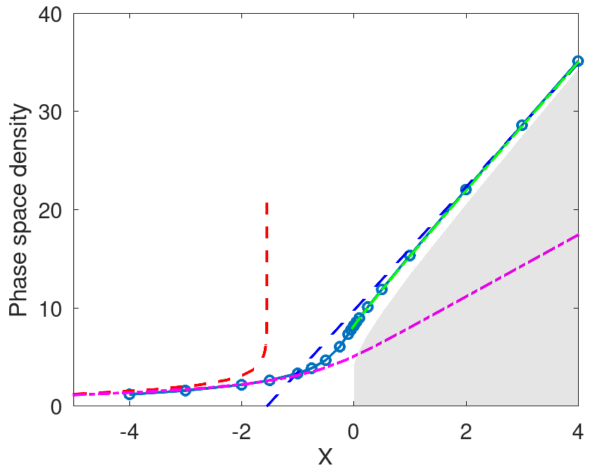

Figure 2.1: Equation of state of the homogeneous Kosterlitz-Thouless transition, for $\tilde{g} = 0.1$ (blue symbols), as a function of $X = (\bar{\mu} - \bar{\mu}_c)/\tilde{g}$ and compared to various analytical approximations: the ideal Bose gas (dashed red curve), the Hartree-Fock semi-classical model (magenta dash-dotted curve), the Thomas-Fermi limit (blue dashed curve) and the Bogoliubov prediction (green dash-dotted curve). The grey shaded area indicates the superfluid phase space density.

$\mathcal{D}_{\text{ideal}} = -\ln\left[1 - \exp\left[\bar{\mu}\right]\right]$ is relevant, up to $X \sim -3$, but diverges as expected for $\bar{\mu} \to 0^-$. A better approximation is provided by the Hartee-Fock mean-field model $\mathcal{D}_{HF} = -\ln\left[1 - e^{\bar{\mu} - \tilde{g}\mathcal{D}_{HF}/\pi}\right]$ that is accurate up to $X \sim -1$, but cannot capture the fluctuating region. For X large and positive the Thomas-Fermi model $\mathcal{D}_{TF} = 2\pi\bar{\mu}/\tilde{g}$ is accurate from $X \sim 1$. In this regime a better approximation is obtained by accounting for the Bogoliubov excitations [Prokof'ev and Svistunov, 2002], which results in the implicit model $\mathcal{D}_B = 2\pi\bar{\mu}/\tilde{g} + \ln\left[2\tilde{g}\mathcal{D}_B/\pi - 2\bar{\mu}\right]$, accurate for $X > 0$.

2.1.2 Ultracold atoms in quasi two dimensions

In most experiments dealing with dilute ultracold atomic ensembles in two dimensions, the atoms are held in a trapping potential, resulting in a inhomogeneous density profile. Thanks to the local density approximation it is possible to map an inhomogeneous system to a homogeneous one, upon using a local chemical potential $\mu_{\text{loc}}(\boldsymbol{r}) = \mu - V(\boldsymbol{r})$, where μ is now the chemical potential corresponding to the peak density. In such a system it is then natural to formulate the equation of state in terms of the total atom number $N(\mu, T)$, where

$$N = \Lambda^{-2} \int d\boldsymbol{r}\, \mathcal{D}\left(\frac{\mu - V(\boldsymbol{r})}{k_B T}\right). \tag{2.2}$$

The superfluid transition can then be defined when the peak phase space density, at the trap center, exceeds the critical value $\mathcal{D}_c$ and this defines a critical atom number N_c. For the special case of a harmonic trap of radial frequency ω_r we find: $N_c = (k_B T/(\hbar\omega_r))^2 \int_{-\infty}^{\bar{\mu}_c} d\bar{\mu}\, \mathcal{D}(\bar{\mu})$, which depends weakly on $\tilde{g}$ and is above the critical atom number for the BEC transition of an ideal gas in a harmonic trap $N^0_{BEC} = (k_B T/(\hbar\omega_r))^2 \pi^2/6$. In fact N^0_{BEC} already provides a fairly good estimate of N_c for a harmonically trapped Bose gas with small $\tilde{g}$.

Ultracold atom experiments deal with dilute atomic samples, usually trapped using magnetic fields or optical forces at the minimum of a harmonic potential $V(\boldsymbol{r}) = M(\omega_x^2 x^2 + \omega_y^2 y^2 + \omega_z^2 z^2)/2$, characterized by three oscillation frequencies $\omega_{x,y,z}$. If the typical energy of an atom is larger than all harmonic oscillator energies $\hbar\omega_{x,y,z}$, its motion will explore a three-dimensional volume. On the contrary, if its energy is comparable to or smaller than $\hbar\omega_z$, it must be described using the quantized energy states of the harmonic oscillator in the z direction. When there is not enough energy to populate the first excited state in the z direction, the atomic motion becomes effectively two dimensional.

A weakly interacting Bose gas is characterized by two natural energy scales: the chemical potential μ and the temperature k_BT. When the temperature decreases, we expect that the population of all thermal excitations in the z direction decrease, thus freezing this degree of freedom for the thermal cloud[1]. Obviously this is a continuous phenomenon and the crossover between the two regimes occurs when $k_BT \simeq \hbar\omega_z$. The chemical potential gives the order of magnitude of the energy available to promote a particle in the quasi-condensate to an excited state after a two-body collision. Due to symmetry reasons the first available excited state must be even and therefore the crossover is expected at $\mu \simeq 2\hbar\omega_z$.

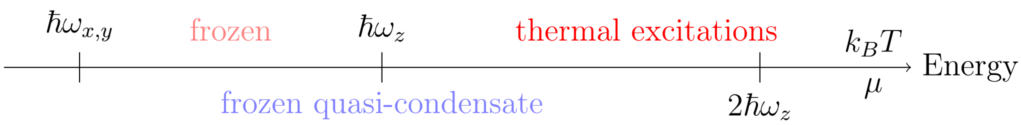

To realize a true two-dimensional system requires to have μ, $k_BT \ll \hbar\omega_z$, and most experiments are realized in the quasi-two-dimensional regime: $\mu \leq \hbar\omega_z$ and $k_BT \simeq \hbar\omega_z$. In this regime the strictly two-dimensional limit is not valid anymore but the transverse excited states can be taken into account. According to [Holzmann *et al.*, 2008], it affects the effective interaction strength, that can be approximated as:

$$\tilde{g} = \sqrt{8\pi}\frac{a_s}{a_z}\sqrt{\tanh\left[\frac{\hbar\omega_z}{2k_BT}\right]}, \tag{2.3}$$

where a_s is the s-wave scattering length, $a_z = \sqrt{\hbar/(M\omega_z)}$ is the length scale of the transverse harmonic oscillator. This expression is valid if the excited states are populated mainly because of the temperature and not because of the interactions, requiring $\mu \ll 2\hbar\omega_z$. In the limit $k_BT \ll \hbar\omega_z$ one recovers the usual two-dimensional interaction strength. Then in the limit of small population in the excited states, the quasi-two-dimensional phase space density in the Hartree-Fock mean-field limit reads [Holzmann *et al.*, 2008]:

$$\mathcal{D} = -\sum_{n_z=0}^{\infty} \ln\left[1 - e^{\tilde{\mu} - \tilde{g}\mathcal{D}/\pi - n_z\hbar\omega_z/(k_BT)}\right]. \tag{2.4}$$

Surprisingly this simple quasi-two-dimensional semi-classical model allows to compute accurately the critical atom-number for realistic experimental parameters, taking into account the small transverse states occupation. This was quantitatively benchmarked against quantum Monte-Carlo simulations [Holzmann *et al.*, 2008]. We will make use of this property in the remaining of this manuscript to estimate the superfluid transition point in inhomogeneous quasi two-dimensional Bose gases.

Since ten years, the progress in the tailoring of optical traps has enabled the realization of box-like traps, realizing uniform weakly interacting Bose gases in three or two dimensions [Chomaz *et al.*, 2015; Gaunt *et al.*, 2013]. Once combined with the ability to tune the interaction strength thanks to Feshbach resonances they offer unique opportunities to directly test the homogeneous models with minimal assumptions [Fletcher *et al.*, 2015].

However it is interesting to point out that, thanks to the local density approximation, combined with the ability to calibrate extremely well the trap potential in experiments,

[1] More precisely the atom number in the transverse excited states saturates [Chomaz *et al.*, 2015; van Druten and Ketterle, 1997].

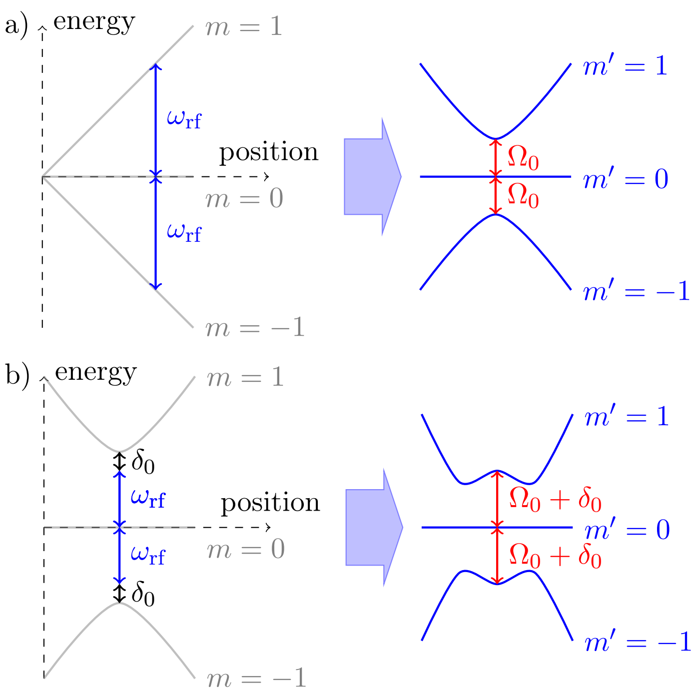

Figure 2.2: Sketch of the adiabatic potential picture with an atom of total spin $F = 1$, for a) resonant rf dressing of a linear potential and b) off-resonant rf dressing of a quadratic potential. Here Ω_0 is the rf coupling amplitude and δ_0 is the detuning with respect to the Larmor frequency at the trap minimum.

the inhomogeneity of the system can also be an asset. For example, by measuring precisely the in-situ density profile of a atomic cloud in a well known potential, it is possible to extract the equation of state from a single experimental measurement [Desbuquois *et al.*, 2014].

2.1.3 Adiabatic potentials

In the BEC group at Laboratoire de physique des lasers we realize quasi-two-dimensional ultracold atomic ensembles using adiabatic potentials proposed in [Zobay and Garraway, 2001, 2004] and pioneered in the group [Colombe *et al.*, 2004]. This technique relies on a very simple mechanism. Consider an atom in its electronic groundstate, with a total spin $\hat{\boldsymbol{F}}$, in the presence of a inhomogeneous magnetic field $\boldsymbol{B}_0(\boldsymbol{r})$. For weak enough fields, the resulting Hamiltonian is described by a linear Zeeman term and assuming that the atomic spin adiabatically follows the field direction, it reads: $\hat{H} = -\mu_B g_F |\boldsymbol{B}_0(\boldsymbol{r})| \hat{F}_z/\hbar$, where μ_B is the Bohr magnetron and μ_F is the gyromagnetic factor. Now if we add a homogeneous radio-frequency (rf) field of frequency $\omega_{\rm rf}$ we can induce transitions between the eigenstates of $\hat{F}_z$ and, for sufficiently strong rf fields induce avoided crossings between the levels. In the rotating wave approximation, the Hamiltonian becomes, after a appropriate unitary transform:

$$\hat{H} = \hbar\sqrt{(\omega_{\rm rf} - \omega_0(\boldsymbol{r}))^2 + \Omega(\boldsymbol{r})^2}\,\hat{F}_z, \tag{2.5}$$

where $\omega_0(\boldsymbol{r}) = |\mu_B g_F \boldsymbol{B}_0(\boldsymbol{r})|/\hbar$ is the local Larmor frequency and $\Omega(\boldsymbol{r})$ is the local coupling strength induced by the rf field.

The energy levels of Hamiltonian (2.5) are sketched on figure 2.2 for an atom with total spin $F = 1$. For the resonant dressing scheme, the upper dressed state energy is minimum on the surface corresponding to the resonance condition $\omega_0(\boldsymbol{r}) = \omega_{\rm rf}$. This surface corresponds to a isomagnetic value of the norm of the static magnetic field. In this configuration the avoided crossing between dressed states is directly given by the value of the coupling amplitude. Therefore it naturally realizes a two-dimensional confinement to the resonant surface and to increase the confinement strength (i.e. increase the curvature of the avoided crossing) one can reduce the rf coupling amplitude. This also leads to increased Landau-Zener losses which limits in practice the achievable confinement. With the off-resonant dressing scheme, it is possible to create tunable barriers, thus realizing for example a double well geometry [Schumm *et al.*, 2005].

The capabilities of adiabatic potentials can be extended by modulating the static potential on a time scale fast as compared to the atomic motion but slow with respect to the rf-field period, thus realizing a time averaged adiabatic potential (TAAP). This can be used to create new trapping geometries [Lesanovsky and von Klitzing, 2007]. Recently it was shown that the combination of several dressing frequency, both in the radio-frequency and micro-wave frequency domains, addressing simultaneously the Zeeman levels of the two groundstate hyperfine manifolds [Luksch *et al.*, 2019] enables even more possibilities [Bentine *et al.*, 2017; Harte *et al.*, 2018], as the realization of mixtures in a adiabatic potential [Bentine *et al.*, 2020].

2.2 Models for deeply degenerate trapped Bose gases

This section introduces theoretical models that are well adapted to describe the dynamics of degenerate Bose gases in the mean-field limit, namely the Gross-Pitaesvekii and classical field equations. It discusses a generic method to solve both models numerically using exact (up-to numerical errors) spectral schemes. A discussion of other relevant models can be found in several papers [Castin, 2001, 2004; Dalfovo *et al.*, 1999; Proukakis and Jackson, 2008].

2.2.1 The Gross-Pitaevskii equation

To model a zero-temperature superfluid we use the well established Gross-Pitaevskii equation describing the time evolution of the mean-field wavefunction $\psi(\boldsymbol{r}, t)$ in the presence of a eventually time-dependent potential $V(\boldsymbol{r}, t)$ [Dalfovo *et al.*, 1999]:

$$i\hbar\frac{\partial}{\partial t}\psi(\boldsymbol{r},t) = \left(-\frac{\hbar^2\boldsymbol{\nabla}^2}{2M} + V(\boldsymbol{r},t) - \mu + g_{3D}|\psi(\boldsymbol{r},t)|^2\right)\psi(\boldsymbol{r},t), \tag{2.6}$$

where $g_{3D} = 4\pi\hbar^2 a_s/M$ is the usual low energy interaction strength characterized by the s wave scattering length a_s. Equation (2.6) captures accurately the low temperature dynamics of a trapped superfluid. When $V(\boldsymbol{r}, t \equiv V(\boldsymbol{r})$ is static and the chemical potential is large, the kinetic energy term can be neglected, resulting in the celebrated Thomas-Fermi solution: $|\psi(\boldsymbol{r}, t)|^2 = (\mu - V(\boldsymbol{r}))/g_{3D}$. The linearization of equation (2.6) around a stationary solution results in the Bogoliubov-de-Gennes equations that describe the low energy modes of a superfluid [Dalfovo *et al.*, 1999].

In order to solve equation (2.6) we use a spectral method: we first compute the energies E_n and eigenstates $\phi_n(\boldsymbol{r})$ of the one body problem (i.e. for $g_{3D} = 0$), where n is a label indexing all the states. We then expand the wavefunction onto the eigenstates: $\psi(\boldsymbol{r}, t) = \sum_n c_n(t)\phi_n(\boldsymbol{r})$, where $c_n(t)$ are time-dependent complex coefficients. In order to keep a computationally tractable problem we introduce the set of low energy states $\mathcal{C} = \{n \mid E_n < E_{\text{cut}}\}$ and truncate the expansion, resulting in a spectral formulation:

$$i\hbar\frac{dc_n(t)}{dt} = (E_n - \mu)c_n(t) + g_{3D}\int d\boldsymbol{r}\phi_n(\boldsymbol{r})^*|\psi_{\mathcal{C}}(\boldsymbol{r},t)|^2\psi_{\mathcal{C}}(\boldsymbol{r},t), \tag{2.7}$$

where $\psi_{\mathcal{C}} = \sum_{n \in \mathcal{C}} c_n(t)\phi_n(\boldsymbol{r})$ is the truncated field. The advantages of the spectral formulation are [Blakie, 2008]:

- we have now to deal only with a set of nonlinear coupled ordinary differential equations, instead of the original nonlinear partial differential equation,
- for most common potentials (hard-wall box, periodic boundary conditions, harmonic or polynomial traps and any combination) the non-linear term can be evaluated exactly, without approximations or aliasing, using a quadrature formula for the integral,
- the truncation is done in a controlled way, through the choice of the cutoff energy E_{cut}.

Obviously the fact that the spectral method relies on the one-body eigenstates makes it efficient only if the trapping potential can be well approximated by a simple formula, as a harmonic oscillator for example. This is the case for a cloud at equilibrium near the bottom of the shell-shaped potential but it cannot easily deal with the curvature. When the spectral method is not applicable, we rely on finite difference or split-step methods for the solution of equation (2.6).

The spectral formulation, as defined by equation (2.7), naturally implements the dimensional reduction if E_{cut} is chosen below the energy of the first transverse excited state. It even allows to study the dimensional crossover at zero-temperature, by choosing a large E_{cut} value and computing the groundstate as a function of the atom number N_0, for example. At large N_0, the density profile will be close to a three-dimensional Thomas-Fermi profile, whereas at small N_0 it should converge to an effective two-dimensional profile with a frozen vertical direction.

2.2.2 Extension to finite temperatures: classical fields

The Gross-Pitaevskii equation arises as the mean field limit of a many body nonlinear equation. Interestingly the spectral expansion allows to write an extended equation that keeps beyond mean field terms and within the most simple approximations results in the simple growth stochastic Gross-Pitaevskii equation:

$$i\hbar\frac{\partial}{\partial t}\psi_{\mathcal{C}}(\boldsymbol{r},t) = \mathcal{P}_{\mathcal{C}}\left[(1-i\gamma)\left(-\frac{\hbar^2\boldsymbol{\nabla}^2}{2M} + V(\boldsymbol{r}) - \mu + g_{3D}|\psi_{\mathcal{C}}(\boldsymbol{r},t)|^2\right)\psi_{\mathcal{C}}(\boldsymbol{r},t) + \eta(\boldsymbol{r},t)\right], \tag{2.8}$$

where $\mathcal{P}_{\mathcal{C}}[f(\boldsymbol{r})] = \sum_{n\in\mathcal{C}}\int d\boldsymbol{r}'\,\phi_n(\boldsymbol{r})\phi_n(\boldsymbol{r}')^* f(\boldsymbol{r}')$ is the projector onto the low energy modes. By treating the high energy modes above E_{cut} as a reservoir and assuming that this reservoir has a well defined temperature T, it can be shown that interactions between low and high energy modes results in a fluctuating field $\eta(\boldsymbol{r},t)$ acting onto low energy modes associated to a damping γ. This is reminiscent of Einstein's fluctuation–dissipation relations, applied here to a non-linear system. The fluctuating field possesses Gaussian correlations:

$$\langle \eta(\boldsymbol{r}',t')^*\eta(\boldsymbol{r},t)\rangle = 2\hbar\gamma k_B T\delta(\boldsymbol{r}-\boldsymbol{r}')\delta(t-t') \tag{2.9}$$

where the average $\langle\cdots\rangle$ is an ensemble average over many realizations and the damping rate can be estimated from the microscopic parameters of the theory $\gamma \simeq 8(a_s/\Lambda)^2$.

It is also very convenient to write this stochastic partial differential equation using the spectral formulation:

$$i\hbar\frac{dc_n(t)}{dt} = (1-i\gamma)\left((E_n-\mu)c_n(t) + g_{3D}\int d\boldsymbol{r}\phi_n(\boldsymbol{r})^*|\psi_\mathcal{C}(\boldsymbol{r},t)|^2\psi_\mathcal{C}(\boldsymbol{r},t)\right) + \eta_n(t), \quad (2.10)$$

where the stochastic term η_n acting on mode n is now characterized by:

$$\langle\eta_n(t')^*\eta_m(t)\rangle = 2\hbar\gamma k_B T\delta_{n,m}\delta(t-t'). \quad (2.11)$$

The resulting set of coupled nonlinear stochastic ordinary differential equations can be solved using an appropriate stochastic integration scheme.

For high energy modes, such that the non-linear term contribution to the dynamics is small, Equation (2.10) can be solved and the equilibrium population is found as:

$$\langle|c_n|^2\rangle \simeq \frac{k_B T}{E_n-\mu}, \quad (2.12)$$

which corresponds to the Rayleigh-Jeans distribution, the high-temperature limit of the Bose-Einstein distribution. This justifies the use of this formalism to study finite temperature effects in ultracold atom experiments, in the limit of high occupation number. More precisely, equation (2.12) allows to estimate the population of the modes at the cutoff energy: $n_\mathrm{cut} \simeq k_B T/(E_\mathrm{cut}-\mu)$ and as the classical field description is valid only for sufficiently populated modes, with occupation ≥ 5, the cutoff can be chosen as: $E_\mathrm{cut} = \mu + 0.2\times k_B T$.

The classical field equation (2.10) is parametrized by the chemical potential μ and the temperature T, through the fluctuations of the stochastic fields η_n, see equation (2.11). Starting from the vacuum, $c_n(t=0)=0$, the atom number first increases and after a typical time of $\sim \hbar/(\gamma\mu)$ it saturates and reach a quasi-steady state. At this point the time evolution of equation (2.10) can be seen as a sampling process of the grand-canonical thermodynamical ensemble of the Rayleigh-Jeans distribution, which may be used to estimate finite temperature equilibrium properties of the state. If necessary, the high energy modes of the reservoir, for $E > E_\mathrm{cut}$, can be accounted for using a simple semi-classical model, at least to describe the equilibrium density profiles. The main limitation of this approach is that equation (2.10) cannot capture the dynamics of the reservoir, which typically requires to solve coupled equations [Proukakis and Jackson, 2008].

2.2.3 Time-of-flight scaling solution

In the experiment, it is often convenient to measure the density distribution after a time of flight: the atoms are released from the trap at $t = 0\,\mathrm{s}$, fall under the influence of gravity and the cloud expands under the influence of the initial velocity distribution and the two-body interactions, resulting (for $T < T_c$) in a bimodal density distribution [Ketterle *et al.*, 1999]:

$$n_\mathrm{tof}(\boldsymbol{r},t) = n_d(\boldsymbol{r},t) + n_T(\boldsymbol{r},t),$$

where t is the time-of-flight duration, $n_d(\boldsymbol{r},t)$ and $n_T(\boldsymbol{r},t)$ are the degenerate (superfluid or condensate) and thermal cloud density distributions, respectively. It is reasonable to assume that the thermal cloud density distribution after a sufficiently long time of flight is very close to a three dimensional Gaussian:

$$n_T(\boldsymbol{r},t) = \frac{N_T}{(2\pi)^{3/2}\sigma_x\sigma_y\sigma_z}e^{-\frac{x^2}{2\sigma_x^2}-\frac{y^2}{2\sigma_y^2}-\frac{z^2}{2\sigma_z^2}},$$

where we expect $\sigma_x = \sigma_y = \sigma_z \simeq t \times \sqrt{k_B T/M}$ for a equilibrium state, allowing to estimate the temperature.

Due to the fact that we use oblate harmonic traps with typically $\omega_z/\omega_r > 10$, the degenerate density profile is well approximated by a hybrid form [Hechenblaikner *et al.*, 2005]:

$$n_d(\boldsymbol{r}, t) = n_0\left(\frac{x}{\lambda_x}, \frac{y}{\lambda_y}\right) \frac{e^{-\frac{z^2}{\lambda_z^2 \sigma^2}}}{\sqrt{\pi}\sigma\lambda_x\lambda_y\lambda_z}, \tag{2.13}$$

where $n_0(x, y)$ is the in situ in plane Thomas-Fermi density profile, possibly including beyond harmonic corrections as a quartic term, see section 3.3.1, $\lambda_{x,y,z}$ are time-dependent scaling factors and σ is the transverse size corrected for the effect of interactions [Hechenblaikner *et al.*, 2005]. By combining the scaling equations described in [Castin and Dum, 1996; Kagan *et al.*, 1996] with the hybrid density profile [Hechenblaikner *et al.*, 2005] and including a possible rotation around the vertical axis in the diffuse vorticity limit [Cozzini and Stringari, 2003], see section 3.2.1, I obtain the self-consistent set of equations:

$$\frac{\sigma^2}{a_z^2} - \frac{a_z^2}{\sigma^2} = \frac{g_{3D}}{\sqrt{2\pi}\sigma\hbar\omega_z} \frac{\langle n_0(x, y)\rangle}{N_0}, \tag{2.14a}$$

$$\ddot{\lambda}_x = \frac{\Omega^2}{\lambda_x^3} + \frac{g_{3D}\,\langle n_0(x, y)\rangle}{2\sqrt{2\pi}M\,\langle x^2\rangle\,\sigma} \frac{1}{\lambda_x^2\lambda_y\lambda_z}, \tag{2.14b}$$

$$\ddot{\lambda}_y = \frac{\Omega^2}{\lambda_y^3} + \frac{g_{3D}\,\langle n_0(x, y)\rangle}{2\sqrt{2\pi}M\,\langle y^2\rangle\,\sigma} \frac{1}{\lambda_x\lambda_y^2\lambda_z}, \tag{2.14c}$$

$$\ddot{\lambda}_z = \frac{a_z^4}{\sigma^2}\frac{\omega_z^2}{\lambda_z^3} + \frac{g_{3D}\,\langle n_0(x, y)\rangle}{\sqrt{2\pi}MN_0\sigma^3} \frac{1}{\lambda_x\lambda_y\lambda_z^2}, \tag{2.14d}$$

where in these equations $\langle \ldots \rangle = \int dxdy\, n_0(x, y) \times \cdots$ and N_0 is the condensate atom number. If the trap geometry is known precisely, the in-situ density profile $n_0(x, y)$ can be computed and the solutions of equations (2.14) can be tabulated for various atom numbers and rotation frequencies. It is then sufficient to measure the atom number in the degenerate part of the bimodal density profile and its rms sizes to infer the *in situ* parameters, see section 3.2.1.

2.3 Experimental realization

I now detail how we succeeded in reaching the quasi two-dimensional limit using adiabatic potentials, achieving the first two-dimensional superfluid trapped only by a magnetic potential, in a extremely smooth and well controlled environment. This work was carried out mainly during the PhD theses of [Merloti, 2013] and [De Rossi, 2016].

2.3.1 The dressed quadrupole trap

We realize adiabatic potentials in the dressed quadrupole trap configuration: the static magnetic field is created by two coils in anti-Helmholtz configuration, creating a magnetic field $\boldsymbol{B}_0(\boldsymbol{r}) = b'(x\boldsymbol{e}_x + y\boldsymbol{e}_y - 2z\boldsymbol{e}_z)$, where b' is the gradient. The rf field is generated by three coils, see section 1.1.4, producing a circularly polarized field along z: $\boldsymbol{B}_{\rm rf}(\boldsymbol{r}, t) = B_{\rm rf}(\cos[\omega_{\rm rf}t]\,\boldsymbol{e}_x + \sin[\omega_{\rm rf}t]\,\boldsymbol{e}_y)$, resulting in a inhomogeneous Rabi coupling between the

Zeeman sub-states [Garraway and Perrin, 2016; Perrin and Garraway, 2017]:

$$\Omega(\boldsymbol{r}) = \frac{\Omega_0}{2}\left(1 - \frac{2z}{\ell}\right), \tag{2.15}$$

where $\Omega_0 = |g_F|\mu_B B_{\mathrm{rf}}/\hbar$ is the maximum coupling and $\ell = \sqrt{x^2 + y^2 + 4z^2}$. For an atom in the $F = 1$ electronic groundstate the total trapping potential reads in the rotating wave approximation:

$$V(\boldsymbol{r}) = \hbar\sqrt{(\omega_{\mathrm{rf}} - \alpha\ell)^2 + \Omega(\boldsymbol{r})^2} + Mgz, \tag{2.16}$$

where $\alpha = |g_F|\mu_B b'/\hbar$ is the magnetic field gradient in frequency units, M is the atomic mass and g the gravitational acceleration. The atoms are trapped near the resonant surface $\ell = \omega_{\mathrm{rf}}/\alpha \equiv r_0$, that defines an ellipsoidal shell-shaped surface with a radius at equator r_0, and because of gravity accumulate at the bottom. The resulting trap is harmonic to a very good approximation and is characterized by [Merloti *et al.*, 2013b]:

- its equilibrium position $\boldsymbol{r}_{\mathrm{eq}} = (0, 0, -R)$, where

$$R = \frac{r_0}{2}\left(1 + \frac{\epsilon}{\sqrt{1-\epsilon^2}}\frac{\Omega_0}{\omega_{\mathrm{rf}}}\right), \tag{2.17}$$

  and $\epsilon = Mg/(2\hbar\alpha)$ quantifies the gravitational sag;

- its vertical oscillation frequency, given by the curvature of the avoided crossing between Zeeman levels:

$$\omega_z = 2\alpha\sqrt{\frac{\hbar}{M\Omega_0}}(1-\epsilon^2)^{3/4} \tag{2.18}$$

- and its in plane oscillation frequencies $\omega_x = \omega_y = \omega_r$, for a circular polarization, with

$$\omega_r = \sqrt{\frac{g}{4R}}\left(1 - \frac{\hbar\Omega_0}{2MgR}\sqrt{1-\epsilon^2}\right)^{1/2} \tag{2.19}$$

  corresponding to the pendulum frequency of small oscillations on the equilibrium surface.

For most experiments this level of approximation is sufficient to describe the trapping potential, and the surface curvature does not play a significant role, except to fix the order of magnitude of the pendulum frequency. Extensions of this simple model will be discussed later, when considering a gravity compensation scheme in section 2.4.1 or the physics in a rotating frame in section 3.3.1

What is interesting with this potential is that the vertical trapping frequency ω_z can be tuned while keeping the radial one ω_r almost constant. In particular by increasing simultaneously the magnetic gradient α and the dressing frequency ω_{rf}, while keeping Ω_0 constant[2] allows to tune the ratio ω_z/ω_r and to enter in the quasi-two-dimensional regime. We thus achieved the first quasi two-dimensional Bose gas in a pure magnetic trap [Merloti *et al.*, 2013b], where we proved the bi-dimensional character by studying the time-of-flight expansion [Hechenblaikner *et al.*, 2005] and the frequency of the in-plane breathing and quadrupole modes.

[2]In practice Ω_0 itself depends on the dressing frequency ω_{rf} because of the frequency response of the dressing antennas, that behave typically as a RLC circuit.

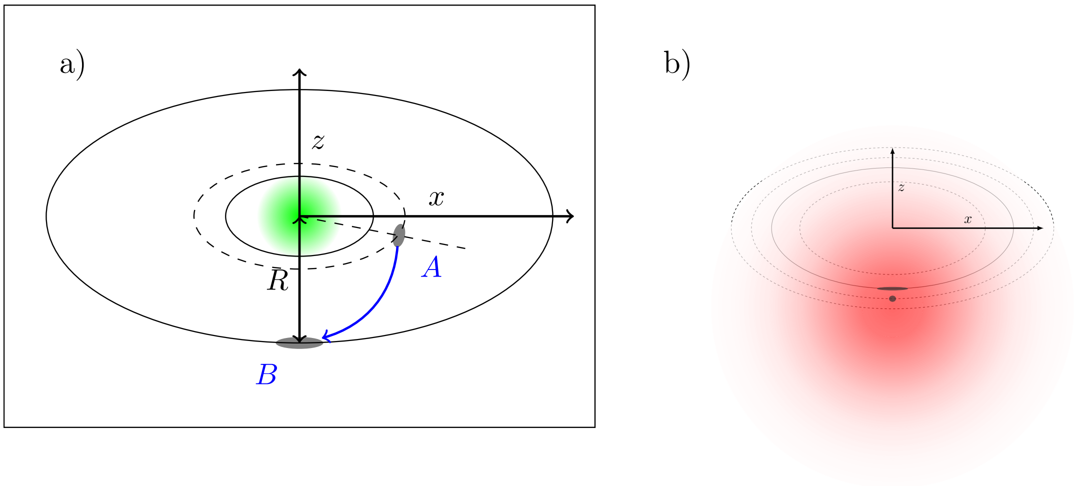

Figure 2.3: Hybrid trap configurations used to load the shell trap, a) from a blue-detuned plug trap configuration [Merloti *et al.*, 2013b] and b) from a red-detuned dimple beam configuration [Rey *et al.*, 2022], approximately represented on the same scale. The transfer from the plug-beam induces necessarily a horizontal displacement that can excite center of mass oscillations in the x direction, while the transfer from the dimple trap can be achieved without moving the atoms. The plug beam is typically focused onto a waist of $\sim 35\,\mu\text{m}$ for a total power of 4 W, while the dimple beam has a waist of $\sim 70\,\mu\text{m}$ for a power of less than 2 W.

2.3.2 Loading strategies

As the dressed quadrupole trap is a two-dimensional surface trap, it cannot be loaded directly from a magneto-optical trap or from a relatively hot atomic cloud held in a magnetic trap. Our loading strategy consists first in evaporating the cloud held in the quadrupole trap, down to a temperature close to the Bose-Einstein condensation transition. This is not possible in a bare quadrupole trap, because of Majorana losses due to spontaneous spin-flips at the trap center where the magnetic field vanishes. To avoid this we use an auxiliary optical beam to prevent this losses, realizing a hybrid quadrupole-optical trap. For a long time we used a blue detuned beam to repel atoms from the trap center [Dubessy *et al.*, 2012b] and more recently we switched to a red detuned beam to attract the atoms at the desired position [Rey *et al.*, 2022].

Both methods allow to load efficiently a Bose-Einstein condensate in the shell shaped trap [Merloti *et al.*, 2013b; Rey *et al.*, 2022], while benefiting from the large initial volume of the quadrupole magnetic trap potential, and a favorable scaling for the initial evaporation stage (the phase-space density scales as $T \propto N^{-3}$, see section 1.2.3). To transfer the cold atomic cloud in the shell-shaped trap one has to turn on the rf dressing, which requires some precautions. The atoms are held at a given magnetic field, resulting in a well defined Larmor frequency ω_i in the hybrid trap, that can be measured precisely with a weak rf probe, by monitoring the induced losses or heating as a function of frequency.

Figure 2.3 compares the shell trap loading procedure starting from the two hybrid trap configurations. In short, the transfer from the red detuned dimple trap can be done without moving the atoms by positioning the beam close to the shell trap equilibrium position. It is then sufficient to turn on the dressing field while ramping down the dimple beam intensity to transfer the atoms without significant excitations [Rey *et al.*, 2022]. The plug trap transfer is slightly more complicated because the initial and final trap position are not the same. Indeed it is very easy to excite center of mass oscillations along the x direction. Moreover we find that it is necessary to expand the shell trap radius during the loading while reducing the plug beam intensity in order to minimize residual excitations. We attribute this to a slowly fluctuating rugosity pattern superimposed onto the plug beam profile, probably due to imperfections of the glass cell and slow drifts of the laser pointing, that changes the optical potential from shot to shot. This effect is mitigated by inflating the shell and avoiding the high intensity regions during the transfer [Merloti *et al.*, 2013b]. Note that the plug beam must be slightly misaligned to the left (or right) of the quadrupole trap center, otherwise two condensates are obtained in the plug trap, that will be transferred simultaneously in the dressed trap, resulting in general in the formation of spontaneous vortices [Merloti, 2013]. The only drawback of using the red detuned dimple trap is an increased heating rate during the evaporation stage, that may be of technical origin and is still under investigation.

2.3.3 Low energy collective modes

Our first interest in the study of quasi two-dimensional Bose gases was to use the low energy collective modes of the superfluid [Stringari, 1996b] to probe the dimensional crossover and the superfluid transition. Thanks to the high degree of control on the adiabatic potential geometry, and on the stability and smoothness of the potential, we studied several of these modes, using two approaches. On the one hand, we can modulate a trap parameter for some time and look for changes in the density profile, as a function of the modulating frequency, for example the width of the cloud along one axis. Usually the recorded curve exhibits one or several resonances that correspond to specific collective modes. On the other hand, we can prepare an out-of equilibrium gas, for example by quenching a trap parameter, and record the time evolution of the density profile. By plotting the time evolution of, for example, the width of the cloud along one axis, we obtain typically oscillations from which the mode energy can be estimated.

Maxim Olshanii suggested to study the radial breathing mode frequency ω_B in the three-dimensional to two-dimensional crossover. As mentioned before, the ratio $\mu/(2\hbar\omega_z)$ can be used to describe this crossover and the breathing mode frequency is expected to reach $2\omega_r$ in the two-dimensional limit [Pitaevskii and Rosch, 1997] while the three-dimensional value, for a zero-temperature Bose-Einstein condensate is $\sqrt{10/3}\omega_z$. This work was motivated by the prospect of observing a quantum anomaly shift on the breathing mode frequency for a strictly two-dimensional system [Olshanii *et al.*, 2010]. While this effect is too small to be observed in our setup, we provided a study of systematic effects associated to the third dimension that can prevent the observation of the quantum anomaly [Merloti *et al.*, 2013a].

Figure 2.4 reports a measurement of the breathing mode frequency for three different ratios of $\mu/(2\hbar\omega_z)$, compared to a perturbative expansion and Gross-Pitaevskii simulations. The agreement of the model with the measurements is reasonable and confirms that the breathing mode frequency is sensitive to the extent of the condensate in the third dimension. This measures where obtained using a combination of resonant and quench excitations of the breathing mode.

When using quench excitations we often noticed that multiple modes were excited simultaneously, which makes sometimes the analysis of the dynamics difficult. During my

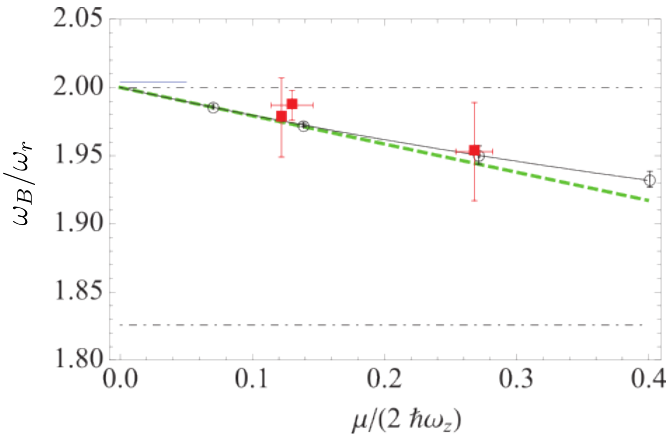

Figure 2.4: Radial monopole mode frequency in a zero temperature quasi two-dimensional Bose gas, as a function of $\mu/(2\hbar\omega_z)$. The red squares are measurements, the error bars reflecting the fit uncertainties. Black circles are the result of a three-dimensional Gross-Pitaevskii simulation, connected by a interpolating black curve. The dashed green line is the prediction from a simple perturbative expansion, and the two horizontal dashed lines indicate the two dimensional $\omega_B = 2\omega_r$ and three dimensional $\omega_B = \sqrt{10/3}\omega_r$ limits. The small blue line indicates the expected quantum anomaly shift, two small to be resolved in the experiment.

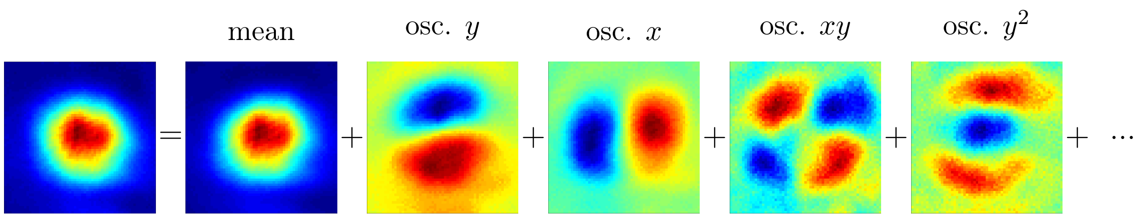

Figure 2.5: An example of principal component analysis applied to the decomposition of the dynamics of a superfluid onto its eigen-modes. A given picture from the initial dataset is expanded as a sum of the mean picture and a weighted sum of all principal components. The spatial structure of the principal components corresponds to what is expected for collective modes. In this example the two dipoles modes are visible, as well as the scissors mode and a quadrupole like mode.

early career I had the opportunity to teach an introductory course on signal analysis to first year students, in which I discussed several techniques to analyze and classify pictures, among which the principal component analysis (PCA) [Jolliffe, 2012]. This method relies on the statistical correlations between several signals to extract useful information from a dataset. I had the idea to apply it to a series of pictures recording the time evolution of a quasi-two dimensional condensate and it turned out to be very effective to identify the collective modes [Dubessy *et al.*, 2014], as shown in figure 2.5. In prior works, PCA was used to filter imaging noise, as demonstrated in [Chiow *et al.*, 2011; Desbuquois, 2013; Segal *et al.*, 2010], and especially in the context of atom interferometry [Dickerson *et al.*, 2013; Sugarbaker *et al.*, 2013].

The reason why PCA is able to detect the collective modes in the dynamics of the density profile is that they have specific spatial density correlations. Indeed PCA relies on the diagonalization of the dataset covariance matrix, whose eigenvectors –the principal components– are statistically independent pictures allowing to reconstruct the density profile at any time. We have proven that the principal components are indeed expected to contain the Bogoliubov eigenmodes and reflect accurately their density profile [Dubessy *et al.*, 2014]. A detailed analysis of the special role of the scissors mode to probe superfluidity is discussed in section 3.1. Recently PCA was used to study the superfluid to supersolid transition in quantum droplets [Hertkorn *et al.*, 2021; Natale *et al.*, 2019] and the emergence of a turbulent cascade in a driven three dimensional Bose-Einstein condensate [Gałka *et al.*, 2022].

2.4 Going beyond *flatland*

The shell-shaped geometry has attracted a lot of interest recently, due to the prospect of realizing this geometry in a micro-gravity environment aboard the International Space Station. Here the key point is that, for an appropriate adiabatic potential, the absence of gravity enables to cover, in principle the whole surface with a thin film of ultracold atoms, thus realizing a topologically non trivial hollow superfluid. This experiment is certainly very difficult, given the constrains of the remote operation of a space based experiment and has not succeeded yet. Meanwhile, the first bubble shaped Bose-Einstein condensate was obtained, on earth by cleverly using a Bose-Bose mixture in the immiscible regime, where the outer lighter specie forms a shell around heavier one in a standard harmonic trap. Although it emulates the desired shape, the dynamics of this system will certainly be richer and more complex than in the case of the simple shell-shaped superfluid, due to the coupling between the two species.

Vanderlei Bagnato convinced us that it was worth trying to address the realization of such filled bubble geometries on earth with our apparatus, to asses the feasibility of such geometry. This work is described in the PhD thesis of Yanliang Guo [Guo, 2021].

2.4.1 An effective anti-gravity force

In fact the dressed quadrupole trap embeds a very convenient knob to compensate gravity on the resonant shell surface. In the simplest approximation, combining (2.15) and (2.16), the trap potential on the resonant surface $\ell = r_0$, for a perfect circular rf polarization, reads:

$$V_{\mathrm{res}}(z) = \frac{\hbar\Omega_0}{2}\left(1 - \frac{2z}{r_0}\right) + Mgz, \tag{2.20}$$

where z is constrained on the resonant ellipsoidal surface: $\rho^2 + 4z^2 = r_0^2$. The resulting potential is a sum of two opposite gradients and, at this level of approximation, the effect of gravity can be perfectly compensated by adjusting the parameters such that:

$$\hbar\Omega_0 = Mgr_0. \tag{2.21}$$

Therefore by tuning the rf coupling amplitude, the rf dressing frequency or the magnetic field gradient it should be possible to compensate the gravity in our trap. This level of approximation allows to build an intuitive and qualitative picture of the experiment I will describe in the next sections. However the resulting model is too simple to capture all the effects but by inspecting the formula for the radial trapping frequency ω_r (2.19), the onset of gravity compensation in the presence of the gravitational sag is achieved when ω_r vanishes, leading to a *a priori* improved criterion:

$$\hbar\Omega_0 = Mg\frac{2R}{\sqrt{1-\epsilon^2}}. \tag{2.22}$$

2.4.2 Controlled expansion of a quantum gas in a shell trap

In order to test this prediction we decided to monitor the changes in atomic density in the trap using our in situ vertical imaging system, when increasing the magnetic field gradient, at fixed coupling and rf dressing frequency [Guo *et al.*, 2022]. It is simpler to change the gradient (i.e. the current flowing in the quadrupole coils), because the control of the Rabi coupling requires the simultaneous control over the amplitudes of both antennas and the rf dressing frequency affects the rf coupling strength and polarization because of the antennas resonances.

We first calibrated precisely the quadrupole magnetic gradient in the range $\alpha \in [4.16(6), 8.49(9)]$ kHz μm^{-1} as a function of the current flowing in the coils by monitoring the displacement of the cloud after time of flight for a rather small rf coupling amplitude $\Omega_0/\omega_{\text{rf}} \sim 0.13$, such that the rotating wave approximation and the prediction of (2.17) are valid. We then increase the rf coupling to a higher value $\Omega_0 = 2\pi \times 85.0(5)\,\text{kHz}$, measured by rf spectroscopy. This value of the rf coupling enables to reach the compensation threshold at a moderate magnetic field gradient. According to (2.21) it occurs for $\alpha \simeq 7.54\,\text{kHz/µm}$, while the improved criterion (2.22) gives a slightly higher prediction $\alpha \simeq 7.90\,\text{kHz/µm}$.

The results of the experiments, as shown in figure 2.6, were at first puzzling. Indeed the progressive increase of the gradient results first in an expansion of the cloud on the bubble surface, as seen in the in situ top view images but leads to the formation of a stable ring shape structure that was not expected in the simple model of (2.20). Moreover the transition between the two regimes occurs at a gradient below 7.40(8) kHz/µm significantly smaller than expected. After a double check of all measurements and a precise tuning of the rf field to a circular polarization, we decided to perform numerical simulations of the expected groundstate, using the Gross-Pitaevskii equation.

The simulations, without adjustable parameters, were able to reproduce quantitatively the experimental measurements, provided that beyond rotating-wave approximation terms are taken into account in the computation of the dressed state potential and the resolution of the imaging objective is used to blur the simulated density profiles. To achieve high accuracy and efficient memory usage in the computation of the groundstate it was necessary to use a mapping to ellipsoidal coordinates. The simulations confirm the appearance of the stable ring shape, that is a genuine effect due to transverse confinement and the fact

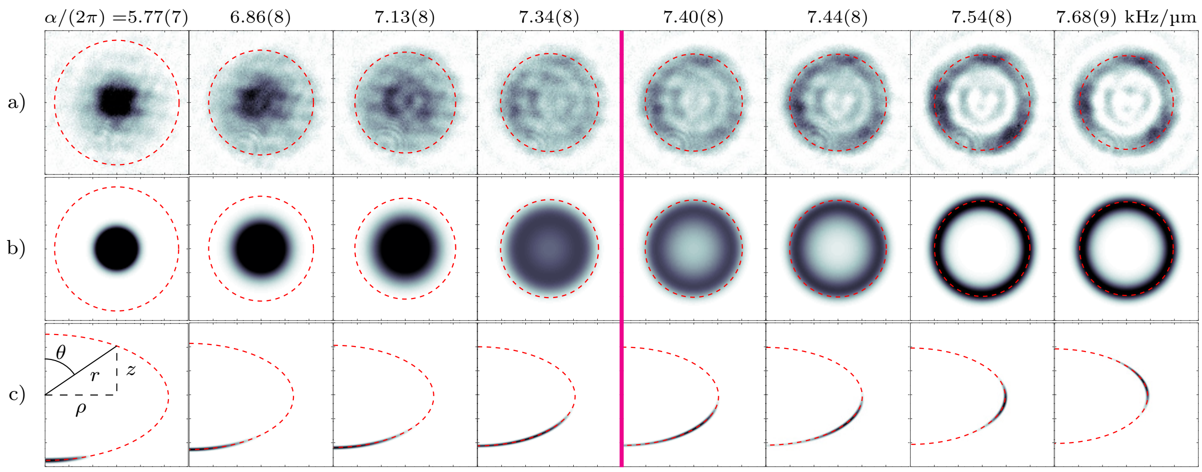

Figure 2.6: In situ atomic density distribution for an ensemble of $N \simeq 10^5$ atoms, evidencing the gravity compensation mechanism and the spontaneous change of topology, as the quadrupole gradient α increases. a) Experimental measurement, b) and c) full GP numerical simulation, top and side views respectively. The pink vertical line corresponds to the observed threshold for gravity compensation, slightly lower than the naive expectation $\alpha/(2\pi) \simeq 7.54(4)\,\mathrm{kHz/\mu m}$ (2.21). For each picture of a) and b) the field of view is $120\,\mu\mathrm{m} \times 120\,\mu\mathrm{m}$, the color scale spans $[0\text{–}35]\,\mu\mathrm{m}^{-2}$, and the dashed red circles indicate the ellipsoidal radius at equator $\rho = r_0$. b) The simulated density profiles are convoluted with a Gaussian of $1/\sqrt{e}$-radius $\sigma = 4\,\mu\mathrm{m}$ to reproduce the experimental imaging resolution. For c) the field of view is $60\,\mu\mathrm{m} \times 60\,\mu\mathrm{m}$ and the dashed red line is the shell trap surface.

that the shell-shaped potential is non separable. A detailed analysis of beyond rotating wave approximation effects is presented in appendix B.

2.4.3 The effect of the transverse confinement

The missing part in the simple approximation of (2.20) is the zero-point energy of the transverse confinement to the surface. Indeed, the local transverse confinement at a given height on the surface is well captured by the simple expression [Guo *et al.*, 2022]:

$$\omega_\perp(z) \simeq \alpha(z)\sqrt{\frac{\hbar}{M\Omega(z)}}, \tag{2.23}$$

where $\alpha(z) = \alpha\sqrt{1 + 12z^2/r_0^2}$ is the local gradient in the transverse direction and $\Omega(z) = \Omega_0/2 \times (1 - 2z/r_0)$ is the rf coupling on the surface, as expected when considering the local avoided crossing between dressed states. The associated zero-point energy can be included in the effective potential on the surface:

$$V_{\mathrm{surf}}(z) = \frac{\hbar\Omega_0}{2} + \left(Mg - \frac{\hbar\Omega_0}{r_0}\right)z + \frac{\hbar\omega_\perp(z)}{2}, \tag{2.24}$$

where the last term, proportional to (2.23) diverges as z approaches the north pole $z \to r_0/2$, thus providing a very effective repulsive barrier, stabilizing the ring shape.

It is interesting to point out that the rotating wave approximation of the adiabatic potential captures qualitatively all the phenomena observed in the experiment and that simple analytical models are obtained when neglecting the gravitational sag. However, to obtain the quantitative agreement shown in figure 2.6, it is necessary to include all the effects: beyond rotating wave approximation modeling of the potential, gravitational sag and the effect of the inhomogeneous transverse zero-point energy [Guo *et al.*, 2022]. Finally, the density modulations with three-fold symmetry in the annular gases, seen in the two rightmost pictures of figure 2.6, can be explained by the gradient of the rf coupling field on the scale of the shell radius.

Conclusion

In this chapter I presented a short introduction to two-dimensional physics, focused on the phenomena we have explored in the group and I explained how we realize quantum Bose gases in two-dimensions using adiabatic potentials. I discussed the interest of using the collective modes of a superfluid to probe the dimensional crossover and introduced a fit free method to identify these modes directly from a collection of experimental density profiles, using a generic tool of signal analysis, the principal component analysis. Finally I presented an original experiment achieving a controlled expansion of a degenerate Bose gas on the shell-shaped surface that leads to a ring shape, when gravity is over-compensated, stabilized by the transverse zero-point energy. In some sense it provides a direct visual proof of the fact that the atoms are truly experiencing a quantized transverse potential.

Before discussing out-of equilibrium phenomena in the next chapter, I would like to point out that one of the strengths of the adiabatic potentials is that they can be determined to a very good precision (at least for the needs of a ultracold atom experiment), from a few simple and independent measurements (gradient calibration, rf spectroscopy, rf polarization tuning, oscillation frequencies). They also provide very long lifetimes and low heating rates, in our experiment typically more than 120 s and about 2 nK/s respectively, thus enabling the study of superfluid dynamics over a long time. In the next chapter I will show that this enables the study of fast rotating superfluids.

Chapter 3

Rotating superfluids on a curved surface

This chapter reports the results of experiments that we performed to probe and characterize superfluidity in a weakly interacting trapped quasi two-dimensional Bose gas. Superfluidity is a fascinating phenomenon, first observed in liquid Helium, then in ultracold atomic gases and more recently in fluid of lights. It manifests itself through specific phenomena, as the existence of quantized vortices, of a critical velocity or the propagation of a second sound, that are all related to out-of-equilibrium physics. It is especially interesting to study it in quasi two-dimensional systems as it is characteristic of the Kosterlitz-Thouless transition. Moreover it is not easy to predict the dynamics of a finite temperature quasi two-dimensional system as models usually rely on simplifying assumptions, that can be tested in the experiment. I describe in this chapter several experiments that give some insight into the superfluid dynamics in two-dimensions. These experiments make use of the high degree of control on the trap geometry achieved with adiabatic potentials, and in particular the absence of rugosity, and the long lifetime in the trap.

Contents

3.1 How to probe superfluidity ?

To study superfluidity several types of experiments can be performed. On the one hand, one can measure equilibrium properties, as the equation of state, the static structure factor, the dispersion relation, or perform interference measurements between two samples to characterize phase coherence. The outcome of these experiments can be compared to the predictions of accurate equilibrium models and thus indirectly probe the superfluid transition. For example, very accurate measurements of the equation of state in weakly interacting trapped Bose gases agree well with the theoretical prediction for the superfluid transition [Desbuquois *et al.*, 2014], similarly, interference measurements allow to evidence the predicted exponential to algebraic transition in the coherence length [Hadzibabic *et al.*, 2006; Sunami *et al.*, 2022] and Bragg spectroscopy allows to recover the expected low energy spectrum. On the other hand one can directly probe the dynamical response in the superfluid phase and show that it is different than the one of the normal phase. For example, one can evidence the existence of a critical velocity for the creation of excitations using a moving obstacle [Desbuquois *et al.*, 2012; Kwon *et al.*, 2015], or the nucleation of quantized vortices by rotating the trap [Madison *et al.*, 2000], or the existence of specific collective modes in the response to a quench [Maragò *et al.*, 2000].

Interestingly, the latter two criteria were not explored before for a quasi two-dimensional weakly interacting Bose gas, probably due to the difficulty of realizing a smooth very oblate and tunable trap potential. As our experiment is well adapted to perform these measurements we decided to investigate these phenomena. I have already shown that we were able to recover the collective modes of a quasi-two dimensional superfluid thanks to the principal component analysis, see section 2.3.3, and we decided to measure how the frequency of one of these modes evolved through the superfluid transition. This study was initiated during the PhD thesis of [Merloti, 2013] and finalized during the PhD thesis of [De Rossi, 2016].

3.1.1 The scissors mode

Among all the collective modes of a harmonically trapped Bose gas [Stringari, 1996a], the scissors mode is sensitive to the moment of inertia of the gas [Guéry-Odelin and Stringari, 1999; Stringari, 1996b]. The scissors mode corresponds to a back-and-forth oscillation of the long axis of the cloud in an anisotropic trap, with for example $\omega_x < \omega_y$. As a classical fluid and a superfluid do not have the same moment of inertia, the frequency of this mode is expected to change in behavior, from a dual frequency response at $\omega_\pm = \omega_y \pm \omega_x$ in the normal phase to a single frequency regime $\omega_s = \sqrt{\omega_x^2 + \omega_y^2}$ in the superfluid phase. This was evidenced for a three dimensional Bose gas held in a cigar shaped cloud [Maragò *et al.*, 2000]. In two dimensions, a finite temperature classical field simulation using the projected Gross-Pitaesvkii equation confirmed that the change of frequency of the scissors mode was related to the apparition of a superfluid fraction [Simula *et al.*, 2008].

In order to excite specifically the scissors mode, one has to start with a cloud at rest in a anisotropic harmonic trap and change abruptly the orientation of the trap axis [Guéry-Odelin and Stringari, 1999]. We achieve this by using a adiabatic potential realized with a elliptical polarization, resulting in a very oblate trap: $\omega_z/(2\pi) = 1.83\,\mathrm{kHz}$, $\omega_x/(2\pi) = 33.8\,\mathrm{Hz}$, $\omega_y/(2\pi) = 48.0\,\mathrm{Hz}$ and a relatively large anisotropy: $\varepsilon = (\omega_y^2 - \omega_x^2)/(\omega_y^2 + \omega_x^2) = 0.34$. As explained in section 1.3.1 we can change the in-plane trap axis orientation while keeping the frequencies constant. For this study the sudden rotation was about 10° in

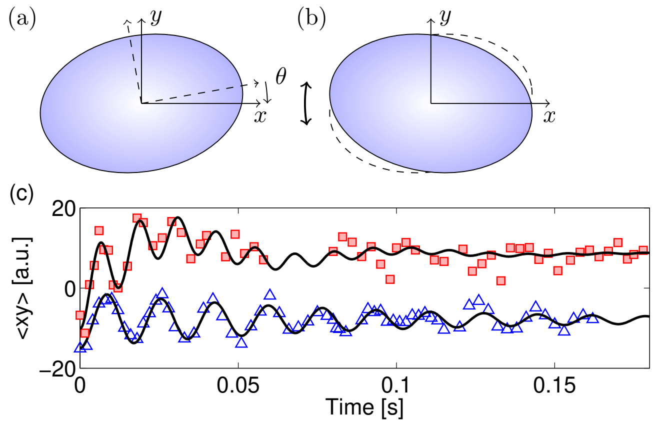

Figure 3.1: a) and b) principle of the scissors mode excitation: at $t = 0\,\mathrm{s}$ the trap axis are suddenly rotated by a small angle $\theta \simeq 10°$ and the subsequent dynamics is recorded. c) Scissors mode oscillations revealed by the moment $\langle xy \rangle_c$ for a pure superfluid (blue triangles) and a thermal cloud (red squares). The black solid lines are a fit with an ad-hoc model.

less than 1 ms. We then record the in situ density profiles after different holding times to follow the dynamics. Finally we repeat the experiment for different temperatures and atom numbers, leading to reduced chemical potentials $\bar{\mu} = \mu/(k_B T)$ in the range $[0.09, 0.88]$. For this trap, the superfluid transition is expected at $\bar{\mu}_c = 0.162$.

The measurement of scissors mode frequency across the superfluid transition turned out to be a difficult challenge. We first tried to apply principal component analysis as it was successful in identifying the collective modes of a ultracold gas deep in the superfluid phase. However it was not as successful when applied to a system with a significant thermal fraction. This can be understood as follows. The scissors mode is a surface mode of the superfluid, where the density oscillations occur essentially in the low density region. As the principal component analysis rely on an analysis of the variance of the whole picture, changes in the low density region have a small contribution to the total variance and therefore are hard to reveal for small oscillations. Moreover, as we expect different oscillations frequencies for the superfluid and the normal phase, that co-exist in the trap, the scissors mode may overlap with several principal components.

We then tried to isolate the contributions of the high and low density parts using a fit by a bimodal density profile: a sum of two Gaussian functions with arbitrary amplitudes, center, sizes and angles. This approach requires twelve independent fit parameters and was not conclusive because the fit procedure was not successful on most density profiles. To avoid the issue of the fit model, we used a model free approach, by interpreting the density profile as a probability distribution and computing the first moments of the distribution, and in particular $\langle xy \rangle_c = \langle xy \rangle - \langle x \rangle \langle y \rangle$ which reveals the scissors contribution [Guéry-Odelin and Stringari, 1999]. Here the average is taken over the measured probability distribution. This last approach allows to extract a signal from all datasets, that we fit using an ad-hoc model [De Rossi *et al.*, 2016]. Figure 3.1 shows the typical behavior of $\langle xy \rangle_c$ for two realizations in the normal phase and deep in the superfluid phase, that display the expected behavior. However in the intermediate regime $\bar{\mu} \simeq \bar{\mu}_c$ a further refinement in the analysis was needed.

3.1.2 Analysis of the local dynamics

Indeed we finally understood that, due to the co-existence of the superfluid and normal phases inside the trap, the scissors response $\langle xy \rangle_c$ still mixes their contributions that are difficult to disentangle. In fact as the moment xy gets larger far from the trap center, the lower density in the thermal component is somehow compensated and depending on

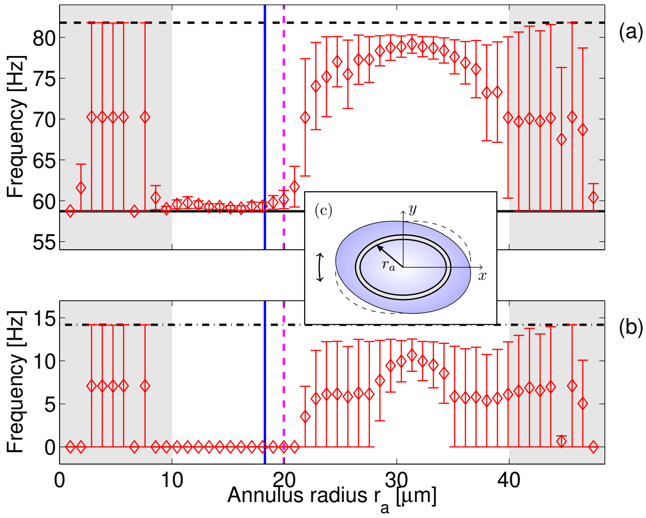

Figure 3.2: a) and b) results of the local moment analysis for $\bar{\mu} = 0.73$: frequencies determined by the fit as a function of the annulus radius r_a. The error bars are deduced from the fit uncertainties. The grey shaded areas indicate the radii at which the fit fails, due to a lack of signal. The vertical dashed lines are estimates of the superfluid boundary according to the equilibrium theory and local density approximation. c) Sketch of the local analysis, highlighting the iso-density annulus.

the relative weights of the normal and superfluid phases the global response appears as normal or superfluid, which is ambiguous for small superfluid fractions [De Rossi *et al.*, 2016].

To solve this ambiguity we introduced a local moment analysis. We restricted the analysis to a thin annulus of with 4 µm, around a rescaled radius $r_a = \sqrt{(\omega_x/\omega_y)x^2 + (\omega_y/\omega_x)y^2}$, corresponding to a iso-density curve around the trap center. Figure 3.2 gives the result of this local moment analysis: at low rescaled radius $r_a \leq 20$ µm, we obtain a local oscillation at the superfluid frequency ω_s, while at higher radius $r_a \geq 23$ µm we find a two-frequencies response, typical of a normal gas [De Rossi *et al.*, 2016, 2017]. The transition between the two regimes is in reasonable agreement with the equilibrium predictions of the Kosterlitz-Thouless theory, within local density approximation and taking into account the 20 % population remaining in the transverse excited states.

This local moment analysis is interesting because it shows clearly that two parts of the sample have a different dynamical response to the angular excitation, due to their different moment of inertia. In that sense the scissors mode response allows to implement a local dynamical analysis that somehow generalizes the local density approximation: the fluid motion is locally determined by the superfluid fraction. The success of this approach can probably be explained by the fact that the density oscillations of the scissors excitation remain close to the initial iso-density curve and therefore the response of the superfluid and normal phases are only weakly coupled. This would probably not work with a quadrupole compression mode for example.

It is interesting to compare this study to the results of [Desbuquois *et al.*, 2012]: using a local excitation (a small defect moving along an iso-density) and measuring a global observable (an increase of temperature) it was found that below a critical radius, the response was governed by a critical angular velocity, characteristic of a superfluid. Here we arrive at the same conclusion, using a "dual" measurement relying on a global excitation and a local measure. What I like the most in our approach is the strong connection with the pioneering works on superfluid Helium that evidenced the superfluid transition in two-dimensions by the frequency change of a torque pendulum [Bishop and Reppy, 1978], which is conceptually very similar to the study of the scissors mode.

3.1.3 Local correlations analysis

Finally, after having understood the importance of the local analysis in the scissors dynamics, we tried a model free analysis of the dynamics using a local principal component analysis [Dubessy *et al.*, 2018]. The idea is to apply principal component analysis to the density fluctuations of a given annulus, corresponding to a iso-density of the sample, in the spirit of the method detailed in the previous section. The results are consistent with the local moment analysis: for most radii one of the principal components exhibits the typical density pattern of the scissors mode and the signal extracted using this component is not correlated between small and large radii. This analysis does not rely on the ad-hoc model to extract the oscillation frequencies and confirms that the scissors dynamics at low radii is weakly correlated to the scissors dynamics at large radii.

3.2 Melting of a vortex lattice

In this section I describe another approach to evidence superfluid properties in a quasi-two dimensional system, based on the response to rotation. I give details about the way we induce rotation in the sample and how we control the effective rotation frequency. This enables us to study how a large vortex lattice in two-dimensions is affected by thermal fluctuations. Most of the work presented here is not yet published. The topic of rotating superfluids has been the subject of a lot of experimental and theoretical works and I will not review here all the known results, but rather introduce only what is needed to understand our experiment. A comprehensive review of this topic can be found in [Fetter, 2009].

For reference table 3.1 lists a few experiments that addressed the physics of rotating Bose gases and highlights their key parameters. The setup discussed in this manuscript presents several advantages: it is highly oblate enabling the study of two-dimensional physics, it embeds beyond harmonic trap corrections in the potential allowing the study of very fast rotating gases and provides a long lifetime and low heating rate. The first vortex lattices were observed in the group during the PhD thesis of [de Goër de Herve, 2018], the rotation control has been improved during the PhD thesis of [Guo, 2021] and a systematic study of the melting carried out during the PhD thesis of [Rey, 2023].

3.2.1 Reaching the groundstate in a rotating frame

I first discuss the properties of the groundstate, at the mean field level, in a rotating frame. The energy functional of a weakly interacting Bose gas in a rotating frame reads [Fetter, 2009]:

$$E[\psi] = \int d\boldsymbol{r}\, \psi^* \left(\frac{\boldsymbol{p}^2}{2M} + V(\boldsymbol{r}) + \frac{g_{3D}}{2}|\psi|^2 - \boldsymbol{\Omega} \cdot \boldsymbol{L} \right) \psi,$$

where $\boldsymbol{p} = -i\hbar\boldsymbol{\nabla}$ is the momentum and $\boldsymbol{L} = \boldsymbol{r} \times \boldsymbol{p}$ is the angular momentum. It is more convenient to introduce the density-phase representation of the wavefunction $\psi = \sqrt{n}e^{i\phi}$ and write the energy as:

$$E[n, \boldsymbol{v}] = \int d\boldsymbol{r} \left(\frac{\hbar^2 |\boldsymbol{\nabla} n|^2}{8Mn} + \left[\frac{M|\boldsymbol{v} - \boldsymbol{\Omega} \times \boldsymbol{r}|^2}{2} + V(\boldsymbol{r}) - \frac{M|\boldsymbol{\Omega} \times \boldsymbol{r}|^2}{2} + \frac{g_{3D} n}{2} \right] n \right),$$

Reference		$\omega_r/(2\pi)$ Hz	$\omega_z/(2\pi)$ Hz	κ $\times 10^{-4}$	Ω/ω_r	ω_z/ω_r	q2D regime
MIT [2]	Na	84	20	–	–	0.24	$\Omega/\omega_r > 0.971$
JILA [182]	Rb	8.5	5.3	–	≤ 0.993	0.62	$\Omega/\omega_r > 0.782$
LKB [20]	Rb	64.8	11.0	62	≤ 1.05	0.17	$\Omega/\omega_r > 0.985$
Seoul [110]	Na	42.5	400	–	≤ 0.89	9.4	✓
LPL [89]	Rb	33.7	356	1.5	≤ 1.05	10.6	✓
MIT [72]	Na	88.6	250.6	–	≤ 1	2.83	✓

Table 3.1: Selection of a few experiments that addressed the topic of inducing rotation in a harmonically trapped Bose-Einstein condensate, presented in chronological order. The trap geometry is characterized by radial ω_r and transverse ω_z frequencies. For some experiments, an additional quartic radial correction κ is relevant, see equation (3.1). The maximum achieved rotation frequency Ω is reported, as well as the trap oblateness ω_z/ω_r. The last column indicates when the quasi-two-dimensional limit is relevant. The row highlighted in blue corresponds to the results discussed in this chapter.

where $\boldsymbol{v} = (\hbar/M)\boldsymbol{\nabla}\phi$ is the velocity field associated to the phase gradient. As a consequence the energy can be seen as the sum of four terms: the kinetic energy cost of bending the wavefunction (related to the so-called quantum pressure), the kinetic energy with respect to the rotating frame, the potential energy lowered by the centrifugal term and the interaction energy. In order to minimize the energy it would be natural to require that the velocity field $\boldsymbol{v}$ behaves as the one of a rigid body $\boldsymbol{\Omega} \times \boldsymbol{r}$. Evidently it is not possible as $\boldsymbol{v}$ is irrotational ($\boldsymbol{\nabla} \times \boldsymbol{v} = \boldsymbol{0}$), while $\boldsymbol{\nabla} \times (\boldsymbol{\Omega} \times \boldsymbol{r}) = 2\boldsymbol{\Omega}$.

As is well known this frustration leads to the apparition of quantized vortices in the wavefunction: localized singularities corresponding to a vanishing density and around which the circulation of the velocity is exactly h/M, one quantum of circulation. While the behavior at small rotation frequency, with a few vortices is very peculiar [Madison *et al.*, 2000], in the large rotation frequency limit, when many vortices are present, they tend to arrange in a regular triangular lattice with constant vortex density (per unit area in the plane normal to the rotation axis) $n_v = M\Omega/(\pi\hbar)$ [Abo-Shaeer *et al.*, 2001] and the coarse grained velocity field mimics the one of a solid body [Fetter, 2009]. I will refer to this phenomenon as the diffuse vorticity limit. This vortex lattice supports elastic deformations known as Tkachenko modes [Coddington *et al.*, 2003; Tkachenko, 1966].

These results apply both for three-dimensional and two-dimensional systems. In three dimensions, the vortex are lines of vanishing density, parallel to the rotation axis that can bend longitudinally, giving rise to a family of modes, known as Kelvin modes [Chevy and Stringari, 2003]. In two dimensions the vortices are considered as point-like object, as the bending of the vortex line is suppressed, provided that the trap is sufficiently oblate $\omega_z/\omega_r > 8$ [Rooney *et al.*, 2011], and only the Tkachenko modes are present. Considering that the centrifugal term weakens the confinement in the plane perpendicular to the rotation axis a Bose gas in a rotating frame naturally enters the quasi-two-dimensional crossover as the rotation frequency increases [Coddington *et al.*, 2003; Schweikhard *et al.*, 2004]. This results in highly oblate geometries even for modest vertical trapping frequencies.

To induce rotation in our experiment we rotate the trap axis at constant frequency, turning on the anisotropy on a fast time scale, following the approach of [Madison *et al.*,

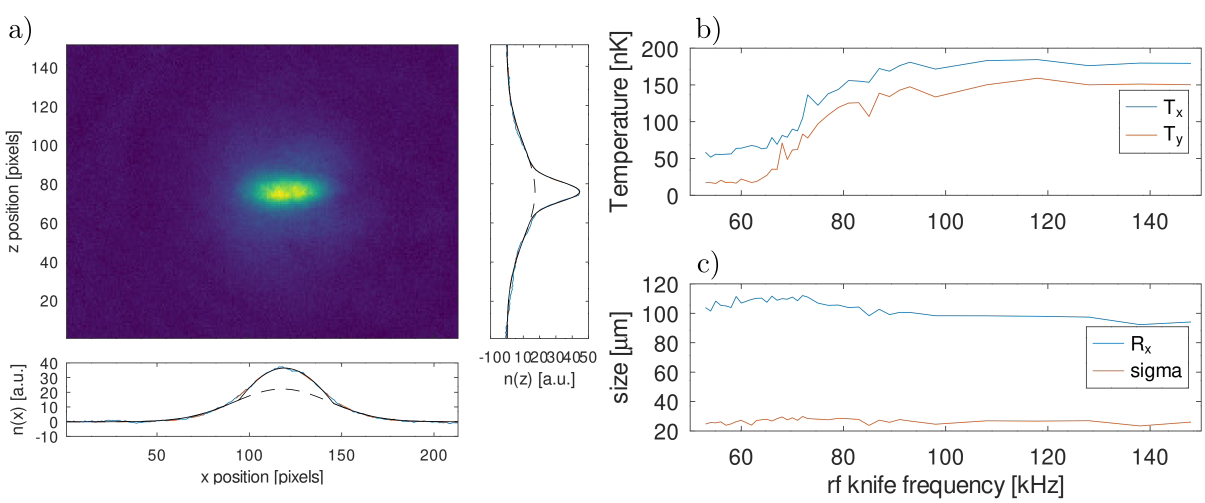

Figure 3.3: a) Horizontal absorption image of a rotating Bose gas after a 23 ms time-of-flight, with one dimensional integrated density profile showing a bi-modal density profile. Sizes of the thermal cloud b) and of the condensate c) as a function of the rf knife frequency. In b) the horizontal and vertical sizes are interpreted as a temperature, assuming that the time-of-flight density distribution reflects the initial velocity distribution.

2001]. This results in a dynamical instability [Sinha and Castin, 2001] that induces a large deformation of the condensate that eventually relaxes to a rotationally symmetric state containing a large vortex lattice [Lobo *et al.*, 2004]. This process requires a form of thermalization that is provided in the experiment by a rf knife truncating the trap depth. To evidence the rotation we measure the time-of-flight expansion of the gas after the stirring phase: we typically observe a fast ballistic horizontal expansion as expected in the diffuse vorticity limit. We may also look at the in-situ density profile and observe how the cloud expands due to the centrifugal force, without being able to resolve the vortex lattice, due to the relatively low imaging resolution. However we observe the vortex lattice for long time of flight, using vertical imaging, thanks to the magnification of all length scales during the expansion.

Figure 3.3a) shows a typical density profile of a fast rotating Bose gas after time-of-flight, adjusted with a bimodal density profile, using an anisotropic Gaussian to fit the thermal cloud and the hybrid ansatz of equation (2.13) to model the superfluid. From the fit we extract the rms sizes of the thermal cloud, that reflect the widths of the initial velocity distribution and hence give an estimation of the temperature, and the size of the superfluid, that undergoes a fast horizontal ballistic expansion due to the rotation. In figure 3.3b) and c) I report the variation of those sizes with the rf knife frequency applied during the stirring phase. This analysis shows a few interesting features. The thermal cloud horizontal size is larger than the vertical one, which means that the thermal cloud is also rotating and that the temperature should be estimated from the vertical size: for low rf knife frequency $\omega'/(2\pi) \leq 60\,\mathrm{kHz}$ it saturates to a value $T \simeq 18\,\mathrm{nK}$. The vertical size of the superfluid part is almost constant and compatible with the expected size for the groundstate of the vertical harmonic oscillator (after expansion): the superfluid is in the quasi two-dimensional regime. Finally the horizontal size of the superfluid part increases as ω' decreases: this can be explained only if the evaporation induces an increase of rotation.

To achieve this fast rotation regime we carefully tune the rf polarization to obtain a very symmetric trap, this is done by maximizing the superfluid part horizontal size in time-of-flight after several seconds of waiting time in the trap. We observe that this size decreases when the rf polarization is not well tuned. We interpret this as a slowing down of the rotation due to a residual static anisotropy [Guéry-Odelin, 2000]: the angular momentum decreases and the clouds evolve towards its equilibrium state in the laboratory frame.

3.2.2 Spin-up evaporation mechanism

To investigate this increase in the rotation frequency with the trap depth, we introduce a post-stirring evaporation ramp and measure the effective rotation rate of the cloud, deduced from its size and atom number, as a function of the final knife frequency. We use a low frequency rf signal added to the vertical axis coil (C_3 on figure 1.3) to truncate the adiabatic potential depth. We thus expect that the rf knife does not break the rotational invariance and that the angular momentum is conserved. Spin-up evaporation has already been observed [Schweikhard *et al.*, 2004], it is a direct consequence of the conservation of angular momentum: as the atoms are removed, the size of the cloud shrinks which leads to an increase of the rotation frequency. However, due to the weak dependence of the cloud size in atom number, a large atom loss is needed to increase significantly the rotation frequency.

In the adiabatic potential, this process is much more efficient because the rf knife evaporate selectively atoms with low angular momentum. Indeed, as the local rf coupling on the resonant surface is inhomogeneous, the trap depth is reduced for atoms that are closer to the rotation axis. This can be qualitatively understood using the simple approximation of the potential on the resonant surface (2.20): the trap depth is approximately $\hbar(\omega' - \Omega_0 \times (\rho/(2r_0))^2)$ and increases as ρ increases.

This property of the adiabatic potential is extremely interesting to control the effective rotation frequency and works surprisingly well, as illustrated in figure 3.4. We have systematically tested the effect of a post-stirring evaporation ramp, from 80 kHz to 60 kHz, for a wide range of stirring anisotropies and frequencies, as reported on figure 3.4c). We find that it enables a fine tuning of the effective rotation frequency Ω from $\omega_r/2$ up to $\sim \omega_r$. In addition, the final temperature is almost constant, set by the final rf knife frequency and of the order of $T = 18\,\text{nK}$. This temperature is of the order of $\hbar\omega_z/k_B$: we therefore expect that all the rotating clouds are well in the quasi two-dimensional regime.

3.2.3 Hints of a melting transition

I conclude this section by presenting preliminary results on the melting of the vortex lattice in a fast two-dimensional rotating Bose gas induced by thermal fluctuations. This is an interesting phenomenon as it allows to test the universal scenario of dislocation mediated melting of a two-dimensional crystal, as proposed by Kosterlitz, Thouless, Halperin, Nelson and Young (KTHNY), see [Gasser *et al.*, 2010] for a review. The basic idea is that the crystal to liquid phase transition in two dimensions occurs through a intermediate hexatic phase following two successive Kosterlitz-Thouless like transitions, corresponding to the unbinding of first dislocations and then disclinations.

For a vortex lattice in a fast rotating Bose gas, [Gifford and Baym, 2008] derived an implicit equation: $\mathcal{D}_s(T_m) = 16\pi\sqrt{3} \simeq 87$, that gives an upper bound for the melting temperature T_m, as a criterion on the two-dimensional superfluid phase-space density $\mathcal{D}_s$.

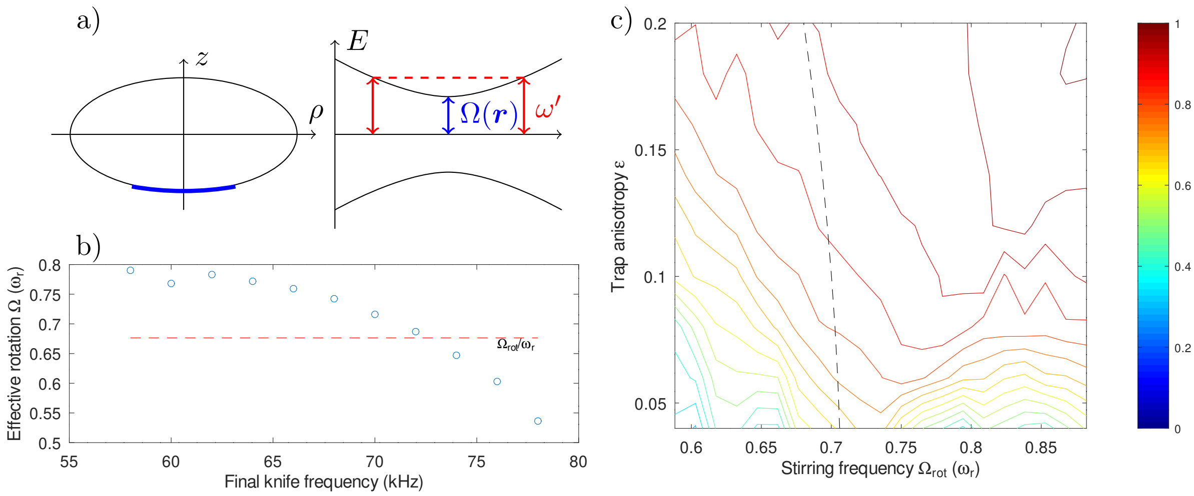

Figure 3.4: a) Sketch of the adiabatic potential in a rotating frame in which the cloud expands under the centrifugal potential. Due to the inhomogeneous coupling the apparent depth $\hbar(\omega' - \Omega(\boldsymbol{r}))$ is not constant on the shell surface. b) Increase of the effective rotation frequency as a function of the final knife frequency, the dashed red line indicates the stirring frequency for reference. c) Map of the achievable effective rotation frequency as a function of the stirring frequency $\Omega_{\rm rot}$ and trap anisotropy ε, for a post stirring evaporation ramp from 80 kHz to 60 kHz.

Surprisingly this criterion does not depend explicitly on the rotation frequency Ω, however the superfluid density itself depends explicitly on Ω as it decreases when Ω increases. Using the trap parameters and the two-dimensional prediction for the superfluid density gives the upper bound $T_m \leq 0.3T_{\rm KT}$. As the trapped superfluid is inhomogeneous this upper bound must be understood as follows: when T approaches $0.3T_{\rm KT}$ the vortex lattice is expected to fully melt, while at lower temperature the vortex lattice should survive at the trap center, where the density is the highest.

Figure 3.5 reports preliminary results on the vortex lattice melting in a fast rotating quasi two-dimensional Bose gas. From top view time-of-flight pictures, we detect the vortex lattice, measure the atom number and the effective rotation frequency Ω. Using the knowledge of the trap geometry and the fact that the temperature of the sample is $T = 18\,$nK we estimate the superfluid transition temperature $T_{\rm KT}$ for each realization. By increasing the rotation frequency we vary the dimensionless temperature $\tau = T/T_{\rm KT}$ and observe a trace of the vortex lattice melting in the loss of contrast in the vortex pair distance histogram as τ approaches 0.3, in reasonable agreement with the above computed bound.

To get a more quantitative analysis, and actually test the KTHNY scenario, it would be interesting to study other order parameters: the translational order, the orientational order and the density of defects (dislocations and disclinations). Currently the data we have are not completely conclusive as finite size effects (the vortex lattice is not infinite) seem to play a significant role. In particular we expect that even a zero-temperature rotating superfluid may exhibit dislocations as the triangular array of vortices is frustrated by the circular superfluid edge, see for example Figure 3.6. To probe more precisely this effect it would be interesting to observe the melting transition at fixed rotation frequency by varying the temperature. This is in principle doable, but requires more work as a

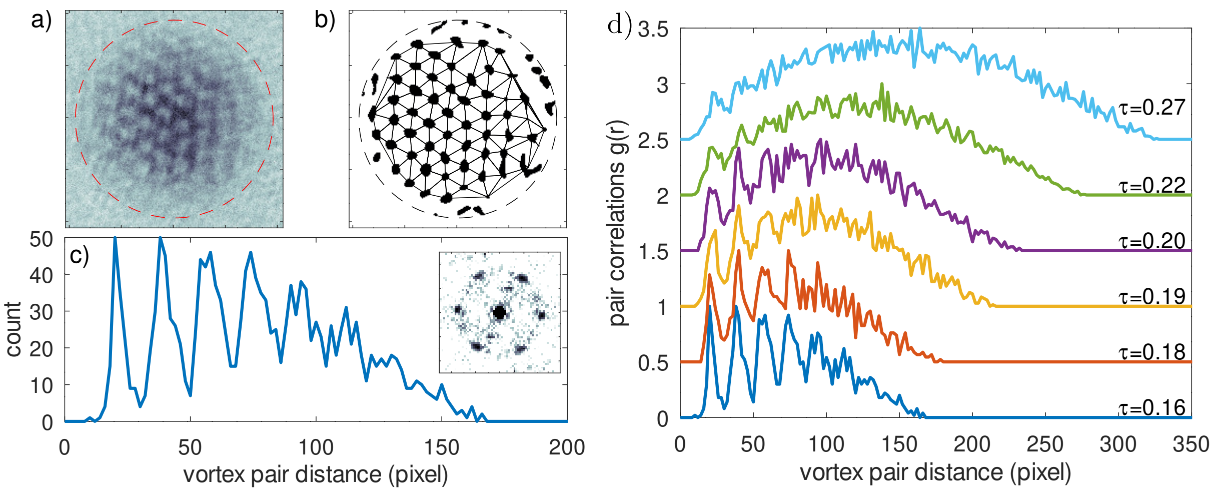

Figure 3.5: Investigation of the melting of a vortex lattice in a fast rotating Bose gas. a) Time-of-flight absorption picture of the density of a fast rotating Bose gas. the dashed red circle indicates the Thomas-Fermi radius. b) Detected vortex lattice using a simple algorithm [Rakonjac *et al.*, 2016]: each dark patch corresponds to a low density region in the picture. c) Histogram of the vortex pair distance computed from the lattice b), exhibiting regular peaks, characteristic of translational order. The inset displays the Fourier transform of the original picture, showing a hexagonal structure corresponding to the reciprocal lattice. d) Changes of the histogram structure as the rotation frequency increases or equivalently the reduced temperature $\tau = T/T_{\mathrm{KT}}(\Omega)$ increases.

calibration of the effective rotation frequency for different temperatures (i.e. final rf knife frequency), see figure 3.4c), will be needed.

3.3 Fast rotating superfluids

Finally I discuss in this section the very fast rotation regime, when Ω approaches ω_r: in this limit the Hamiltonian of a two-dimensional atomic gas acquires a Landau level structure, the one-body energy spectrum being made of many degenerate states, separated by energy gaps of size $2\hbar\omega_r$, see [Cooper, 2008] for a review. This stimulated lots of theoretical and experimental works to investigate the quantum Hall effect with ultracold atoms. Unfortunately the strongly correlated regime is out of reach in most experiments as it can be realized only with extremely low atom numbers [Roussou *et al.*, 2019]. However reaching the fast rotation regime in a shell-shaped trap leads to interesting effects, as reported in the PhD theses of [de Goër de Herve, 2018] and [Guo, 2021].

3.3.1 The giant vortex transition

As $|\Omega| \to \omega_r$ the centrifugal term reduces the radial harmonic trap potential and the next order terms in the potential become important. For the shell trap, the effect can be estimated from the simple surface potential (2.20) in the rotating frame:

$$V_{\mathrm{res}}(\rho) \simeq V_0 + \frac{M\omega_r^2}{2}\rho^2\left(1 - \frac{\Omega^2}{\omega_r^2} + \kappa\frac{\rho^2}{a_r^2}\right), \tag{3.1}$$

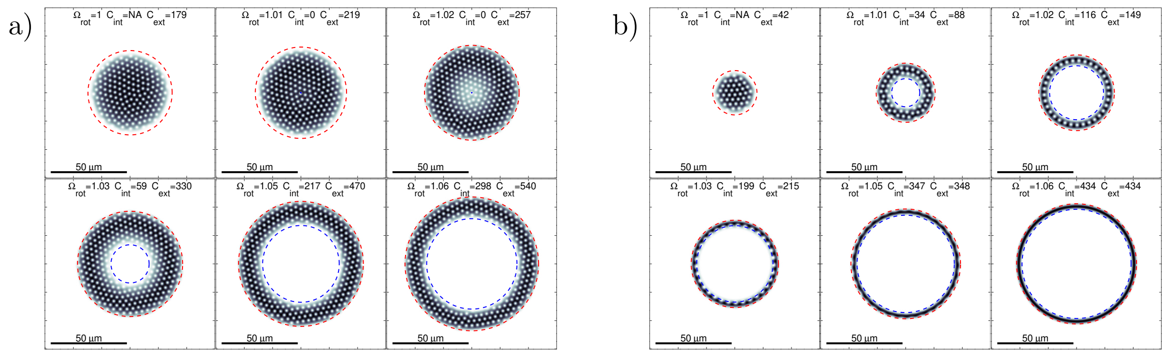

Figure 3.6: Gross-Pitaevskii zero temperature simulation of the giant-vortex transition with increasing rotation frequency Ω, for our experimental parameters with a) $N = 2\times10^4$ and b) $N = 400$ atoms. The red (blue) dashed circle indicates the outer (inner) Thomas-Fermi radius, along which the circulation of the velocity field is evaluated. The pure giant vortex state corresponds to equal inner and outer circulations $C_{\text{int}} = C_{\text{ext}}$, otherwise the difference between the two give the number of vortices in the bulk of the ring. Note that the vortex lattice is frustrated by the boundaries and that other peculiar states can be achieved, as the “vortex necklace”.

where V_0 is a constant offset, $a_r = \sqrt{\hbar/(M\omega_r)}$ is the natural length scale of the trap harmonic potential and $\kappa \simeq (a_r/(2r_0))^2 \simeq 1.5\times10^{-4}$ is the dimensionless amplitude of the quartic term.

This form of harmonic plus quartic potential in a rotating frame was previously introduced in the context of fast rotating Bose gases to help stabilize the gas and realize the limit $\Omega = \omega_r$ [Bretin *et al.*, 2004]. It was studied theoretically and a transition to a giant vortex state was predicted [Fetter, 2001; Fetter *et al.*, 2005; Kasamatsu *et al.*, 2002; Kavoulakis and Baym, 2003; Lundh, 2002], but never observed. This transition occurs above a critical rotation frequency $\Omega_h > \omega_r$, beyond which it becomes more favorable to create a multiply quantized vortex at the center of the trap. At the single particle level, the minimum of the potential (3.1) occurs at a finite radius $\rho_m = a_r\sqrt{((\Omega/\omega_r)^2-1)/(2\kappa)}$, as soon as $\Omega > \omega_r$, however the creation of a multiply charged vortex in the center requires that this potential minimum exceeds the chemical potential: $\mu < \hbar\omega_r/(8\kappa)\times((\Omega_h/\omega_r)^2-1)^2$. For a two-dimensional system in the Thomas-Fermi limit, the normalization of the wavefunction gives the explicit formula [Fetter *et al.*, 2005]:

$$\Omega_h = \sqrt{1+\left(\frac{12\kappa^2\tilde{g}N}{\pi}\right)^{1/3}}.$$

Numerical simulations using Gross-Pitaevskii equation, see Figure 3.6 show that, for our trap parameters, a zero temperature superfluid contains a large vortex lattice with very flat density for $\Omega = \omega_r$, that remain present but with a density depletion for $\omega_r < \Omega < \Omega_h$ and finally contains a vortex lattice and a multiply charged vortex in the center for $\Omega > \Omega_h$. Eventually for a larger rotation frequency, $\Omega > \Omega_{gv}$ all the vortices coalesce at the trap center and a giant vortex state is obtained, characterized by a pure two-dimensional circulation state: $\psi(\rho,\phi) = \sqrt{n(\rho)}e^{im\phi}$, with a large angular momentum m. Equivalently the transition can be observed at fixed rotation frequency $\Omega > \omega_r$, by decreasing the atom

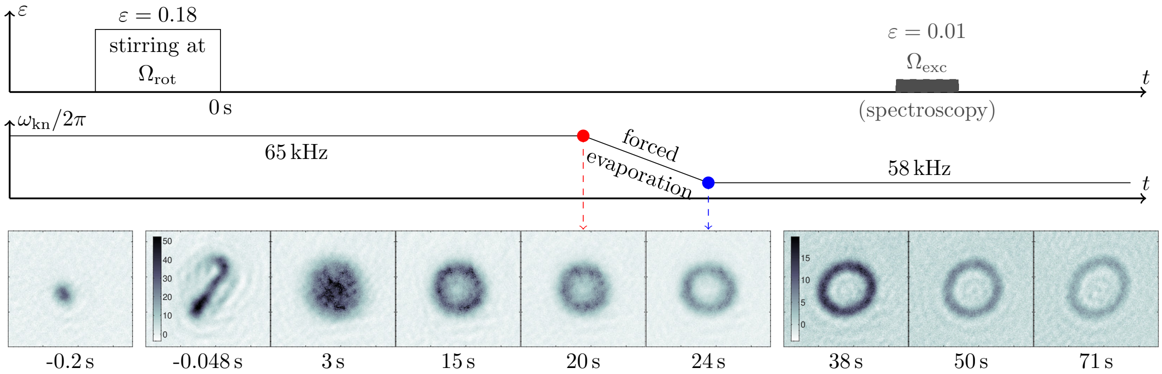

Figure 3.7: Sketch of the experimental sequence leading to the formation of a dynamical ring and in situ images of the atomic density distribution. The leftmost image shows the initial density distribution before stirring, only 10 % of the atoms are imaged. As the rotation frequency increases, the peak density in the pictures decreases and we use two different gray level scales for images taken before and after $t = 25$ s, for which the darkest pixels correspond to densities of $50\,\mu\text{m}^{-2}$ and $20\,\mu\text{m}^{-2}$ respectively.

number or tuning the quartic term.

Thanks to our fine control of the rotation frequency, we managed to increase Ω beyond Ω_h and observe the formation of a dynamical ring of atoms, sustained by its own rotation [Guo *et al.*, 2020]. Figure 3.7 shows the creation of a dynamical ring using the spin-up evaporation mechanism, where the increase of rotation frequency results in a full depletion at the trap center. The ring shape is robust to atom losses and persists for more than one minute. We were not able to test precisely the transition to a multiply charged central vortex scenario because, as reported in section 3.2.3, thermal fluctuations induce a melting of the vortex lattice to a vortex liquid state, and for fast rotations, the density drops during the time-of-flight expansion thus reducing a lot the signal to noise ratio. Both effects tend to hinder the detection of the vortices in our pictures.

3.3.2 Observation of a supersonic superfluid flow

We observe that the in situ measured density profiles are extremely well reproduced by zero temperature Gross-Pitaevskii simulations, convoluted by the finite imaging resolution. Using simple Thomas-Fermi profile estimates, we extract the chemical potential μ and the radius corresponding to the peak density r_{peak}. Interestingly, we find that the speed of sound deduced from the chemical potential: $c_s = \sqrt{\mu/M}$ is much smaller than the fluid linear azimuthal velocity: $v = \Omega r_{\text{peak}}$ in the laboratory frame. In other words the flow is supersonic, with estimated Mach numbers (v/c_s) between 11 and 18, for the fastest rotation [Guo *et al.*, 2020]. A supersonic flow has also been realized in a circular atomic waveguide, based on time-averaged adiabatic potentials [Pandey *et al.*, 2019]. To verify this estimate we performed a time-of-flight expansion measurement, as reported in Figure 3.8, providing a direct measurement of the azimuthal velocity, in good agreement with the in situ Thomas-Fermi estimation. The typical azimuthal velocity is of the order of $6-7$ mm/s, while the chemical potential is below 100 Hz, resulting in a speed of sound typically below 0.6 mm/s.

The fact that the in situ profiles are well reproduced by the mean field theory is an in-

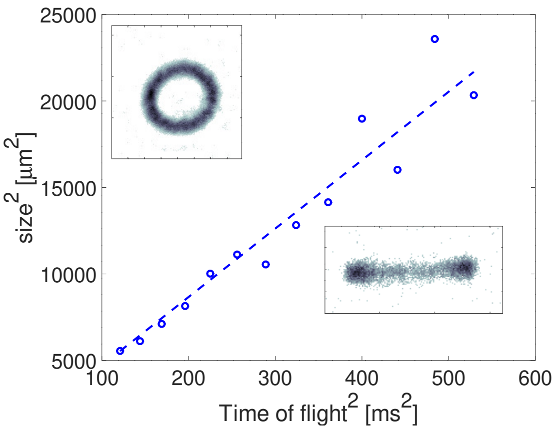

Figure 3.8: Evidence of the fast ballistic expansion of a dynamical ring configuration, as seen in horizontal time-of-flight images. The top left inset shows the in situ distribution, forming a ring shape of radius $\sim$ 32 µm, the bottom right inset shows a typical time-of-flight profile. We report on the graph the square of the horizontal rms size as a function of the square of time of flight, that displays the expected linear scaling.

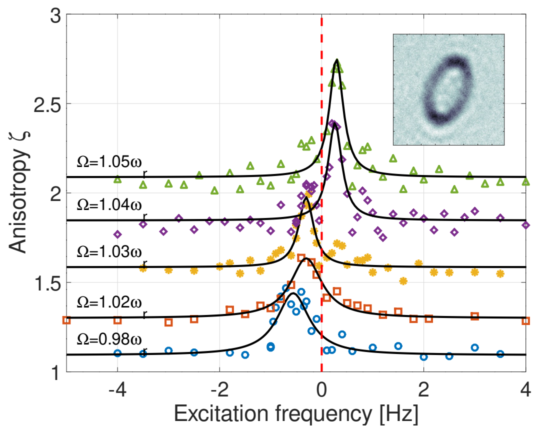

Figure 3.9: Cloud anisotropy ζ as a function of the probe frequency $\Omega_{\rm exc}$ for different effective rotation rates Ω/ω_r = 0.98, 1.02, 1.03, 1.04 and 1.05 (circle, square, star, diamond, and triangle symbols, respectively). The black solid curves are Lorentzian fits to the data. Inset: example of a resonantly excited dynamical ring.

direct proof that the ultracold atom gas is still deep in the superfluid regime. To get more insight we studied the variations of the collective modes frequencies of the cloud as the rotation frequency is increased. In particular we measured the quadrupole mode frequencies, using a spectroscopic measurement: after having prepared a rotating sample at the desired rotation frequency Ω, we turn on a weak trap anisotropy $\varepsilon \simeq 0.01$ rotating at a frequency $\Omega_{\rm exc}$. By varying $\Omega_{\rm exc}$ we observe resonances corresponding to the two quadrupole modes $\Omega_{m=\pm 2}$, as expected. At low rotation frequency, one resonance occurs at positive frequency (ie for a co-rotating excitation) corresponding to the $m = +2$ quadrupole mode, while the other one is at negative frequency (counter-rotating excitation), corresponding to the $m = -2$ quadrupole mode. We checked that $\Omega_{m=2} - \Omega_{m=-2} = 2\Omega$, as expected. For fast rotations $\Omega \geq \omega_r$ the spectrum is affected by the quartic term [Cozzini, 2006; Cozzini *et al.*, 2005]: curiously we find that it becomes very hard to excite the $m = +2$ mode, while the $m = -2$ mode acquires a positive frequency, i.e. becomes co-rotating. This is not expected from the Bogoliubov analysis of a superfluid in a rotating harmonic plus quartic two-dimensional potential [Cozzini, 2006; Cozzini *et al.*, 2005; Guo *et al.*, 2020]. Further experiments are needed to solve this puzzle, and it may be necessary to study other modes in the vicinity of the dynamical ring transition, as for example the monopole mode.

3.3.3 Landau levels picture

Finally it is interesting to discuss in this context the Landau level picture. The Hamiltonian of a harmonic oscillator, with radial symmetry, in a frame rotating around the z axis

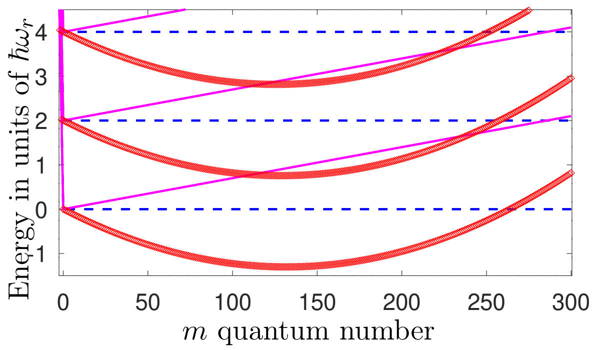

Figure 3.10: Landau level picture (blue dashed lines), the levels are classified by their angular momentum quantum number m, and approximate realizations: best case reported by the JILA group at $\Omega = 0.993\omega_r$ [Schweikhard *et al.*, 2004] (magenta lines), the LPL adiabatic potential for $\Omega = 1.02\omega_r$ (red symbols) taking into account the quartic term. For both cases the number of states in the approximate LLL is ~ 290.

at angular frequency Ω is conveniently written using the $\hat{a}_\pm = (\hat{a}_x \mp i\hat{a}_y)/\sqrt{2}$ operators, where $\hat{a}_\alpha$ is the standard annihilation operator of the harmonic oscillator in direction $\alpha = x, y, z$, resulting in [Fetter, 2009]:

$$\hat{H} = \hbar\omega_r(\hat{a}_+^\dagger\hat{a}_+ + \hat{a}_-^\dagger\hat{a}_- + 1) - \hbar\Omega(\hat{a}_+^\dagger\hat{a}_+ - \hat{a}_-^\dagger\hat{a}_-) + \hbar\omega_z\left(\hat{a}_z^\dagger\hat{a}_z + \frac{1}{2}\right).$$

The energy spectrum is thus very simple, characterized by a set of three quantum numbers (n_+, n_-, n_z): $E_{n_+,n_-,n_z} = \hbar(\omega_r - \Omega)n_+ + \hbar(\omega_r + \Omega)n_- + \hbar\omega_z n_z + E_0$ where $E_0 = \hbar\omega_r + \hbar\omega_z/2$ is the zero point energy. In the limit $\Omega \to \omega_r$ the spectrum is made of degenerate manifolds spanned by the integer n_+ and indexed by the two integers (n_-, n_z). In particular the groundstate manifold is separated from the others by a energy gap $\min(2\hbar\omega_r, \hbar\omega_z)$, and is spanned by states of the form:

$$\psi_{LLL}(\boldsymbol{r}) = A\sum_m c_m \rho^m e^{im\phi} e^{-\frac{\rho^2}{2a_r}} e^{-\frac{2z^2}{a_z^2}}$$

emphasizing the similarity with the fractional quantum Hall effect for two-dimensional electrons subjected to a strong magnetic field [Fetter, 2009; Watanabe *et al.*, 2004].

To study the influence of the weak quartic term considered in equation (3.1), on this energy spectrum, it is convenient to introduce the quantum numbers $n = n_+ + n_-$ and $m = n_+ - n_-$ that correspond to the eigenvalues of the radial energy and angular momentum, respectively. As the quartic term $\hbar\omega_r/2 \times \kappa(\rho/a_r)^4$ commutes with $\hat{L}_z$, it conserves the m quantum number but mixes states with different n values. This results in a bended Landau level picture, as reported in Figure 3.10, for which the manifolds are still separated by a $2\hbar\omega_r$ gap. This property is very convenient to build a exact Laguerre-Gauss quadrature to solve the spectral form of the Gross-Pitaevskii equation at zero (2.7) or finite (2.10) temperature, following the approach of [Wright *et al.*, 2008].

As mentioned above, during the spin up evaporation the chemical potential decreases, because the atomic density decreases as the gas expands, and eventually becomes smaller than $2\hbar\omega_r$. In this situation we realize a two-dimensional superfluid in the lowest Landau level, and the emergence of the dynamical ring can be seen at the mean field level as the condensation in the lowest energy states of Figure 3.10, with large angular momentum. As typically $k_BT \simeq \hbar\omega_z \simeq 5 \times 2\hbar\omega_r$ the thermal cloud populates several Landau levels for these experiments.

Conclusion

In this chapter I described a series of experiments aiming at probing the superfluid properties of two-dimensional weakly interacting Bose gases by studying their response to rotation. I have first reported a direct, in situ, measurement of the Kosterlitz-Thouless transition in a trapped gas, evidenced by the shift of the scissors mode collective excitation frequency across the normal to superfluid transition. This is enabled by a local analysis of the dynamics, showing that the inner part of the cloud is superfluid while the outer part is in the normal phase. I have then discussed two-dimensional physics in a rotating frame and in particular the melting of a two-dimensional vortex lattice, induced by thermal fluctuations. This study is made possible by a fine control of the effective rotation rate of the atomic cloud, in a quasi two-dimensional geometry, in which the vortices behave as point like objects. As mentioned before, this requires only a moderately oblate trap $\omega_z/\omega_r > 8$ which is easily achieved in the shell trap. In fact reducing this ratio from 40 to 10.6, by mainly decreasing the magnetic gradient, helps to increase the lifetime and limit the heating rate, which is crucial to achieve the fast rotation regime, given the long thermalization time of the vortex lattice. Finally I have shown that the shell potential in a rotating frame enables the study of the giant vortex transition, realizing a supersonic flow, a new regime for fast rotating superfluids.

One interesting feature of the shell trap that we understood while doing these experiments if the fact that the rf-knife allows to control the temperature and finely tune the effective rotation frequency, thanks to a spin-up evaporation mechanism. This enabled a preliminary study of the two-dimensional vortex lattice melting transition, at constant temperature and almost constant atom number, where the transition is driven by the fact that when the rotation rate increases, the cloud expands and thus the phase-space density (or the critical temperature) decrease. Unfortunately, we work with a relatively small system in which finite size effects cannot be ignored and must be accounted for, when trying to compare with theoretical predictions derived for infinite size systems at the thermodynamic limit. To do this properly we may need to perform finite temperature classical field simulations in a rotating frame, adapting the method of [Blakie, 2008; Wright *et al.*, 2008] to fast rotations. Another possibility would be to cross the melting transition at constant rotation frequency by varying the temperature and atom number, which is in principle doable. This would simplify the interpretation of the measurements, as I expect in this case that the finite size corrections will remain constant (at least to leading order).

Another research direction opened by these works in the study of a fast rotating Bose gas in the lowest Landau level, that we can achieve by lowering the rf-knife and hence the temperature and atom number. Here the idea would be to study the mean-field physics in the lowest Landau level, both theoretically and experimentally. In particular it would be interesting to investigate the collective modes in this regime and test if it can account for the deviation of the measurements from the hydrodynamic Thomas-Fermi predictions observed for the quadrupole mode. Although the study of many-body physics in this system is practically out of reach [Roussou *et al.*, 2019], recent experiments at MIT showed that interesting dynamics could be investigated in the mean-field lowest Landau level [Fletcher *et al.*, 2021; Mukherjee *et al.*, 2022]. Taking advantage of the tunability of the dressed potential to implement rotation schemes it seems feasible to address similar topics in our experiment.

Chapter 4

A superfluid in a ring trap

This last chapter reports my contributions to the study of a superfluid trapped in ring shaped potential, realizing a circular atomic waveguide. This project was initiated by Hélène Perrin before I joined the group, following the proposal [Morizot *et al.*, 2006], and was carried out in the experimental setup during the PhD theses of [De Rossi, 2016], [de Goër de Herve, 2018] and [Guo, 2021] under the supervision of Laurent Longchambon, in parallel of the experiments reported in the previous chapters. This project was partly funded by a ANR grant *SuperRing* (ANR-15-CE30-0012), during the years 2016–2018, in collaboration with the group of Anna Minguzzi in Grenoble. This has been for me a unique opportunity to develop my skills in theoretical modeling and numerical simulations of low-dimensional systems.

Contents

4.1 Context: the emergence of atomtronics

This part of the manuscript is an illustration of the concept of quantum simulation [Bloch *et al.*, 2012]: using the high degree of tunability of ultracold atom experiments it is possible to emulate a specific Hamiltonian relevant for a particular problem, in a clean, controllable environment. Although the simulation of a real-life complex condensed matter system, as a high-Tc superconductor material, is still out of reach, ultracold atom platforms enable the detailed study of the building blocks of model Hamiltonian that try to capture the underlying physics at the microscopic level. The strength of quantum simulation lies in the fact that most of these simple models are complex enough to be extremely hard to solve using analytical or numerical methods: the analog experiment thus provides a crucial input through the measurement outcomes.

Thanks to the possibility of designing more and more complex trap shapes, a subfield of quantum simulation, now commonly called atomtronics, targets the study of superfluid transport in atomic circuits, as an analogy of the coherent motion of electrons in superconducting circuits. This is motivated by the opportunity of extending the possibilities of atom interferometry and the study of fundamental effects in the coherent manipulation of a matter wave [Amico *et al.*, 2017; Ryu and Boshier, 2015].

4.1.1 Atomic waveguides

For more than fifteen years several research groups have investigated the persistent flows of ultracold atoms in the most basic atom circuit: the ring trap geometry [Gupta *et al.*, 2005], from the first observation of persistent currents [Ryu *et al.*, 2007], the realization of a loop with a weak link [Ramanathan *et al.*, 2011; Wright *et al.*, 2013b] allowing to drive phase-slips [Wright *et al.*, 2013a], the investigation of the stability of persistent currents [Beattie *et al.*, 2013; Moulder *et al.*, 2012] and the recent achievement of persistent currents in Fermionic systems [Cai *et al.*, 2022; Del Pace *et al.*, 2022]. Further trap shaping enable precise interferometric measurements of the circulation state [Corman *et al.*, 2014; Eckel *et al.*, 2014a], while the fine control of the dynamics enable the study of the so-called atomtronic SQUID analog [Eckel *et al.*, 2014b; Jendrzejewski *et al.*, 2014; Kumar *et al.*, 2016; Ryu *et al.*, 2020; Wang *et al.*, 2015], including the effects of finite temperature [Kumar *et al.*, 2017].

I contributed to this topic by elucidating the stability of a persistent current in a ring shaped waveguide, using the Bogoliubov-De Gennes stability analysis [Dubessy *et al.*, 2012a]. We evidenced the role of surface modes in the definition of the critical velocity, which can be captured with a simple analytical model [Anglin, 2001]. For a ring there are two surfaces, corresponding to the inner and outer radii of the superfluid and we have shown that the instability triggers first at the inner surface. The predictions of our model are in excellent agreement with experiments [Moulder *et al.*, 2012].

Later, we proposed a protocol to imprint a persistent current onto a ring-shaped atomic waveguide, by directly manipulating the phase of the superfluid wavefunction [Kumar *et al.*, 2018]. The idea is to shape a laser beam with a specific intensity profile and to use the light shift induced by this beam to create a gradient of the superfluid phase along the ring. One advantage of this protocol is that it can be applied to atoms trapped in a adiabatic potential, whereas other protocols (such as the one used in [Moulder *et al.*, 2012]) may fail. We have shown using numerical GPE simulations that this process was efficient to produce a flow with a well defined circulation. We also demonstrated that the desired intensity profile can be produced with a spatial light modulator and optimized using a simple feed-forward algorithm [Kumar *et al.*, 2018]. We have not implemented this method onto the experiment yet, but it was recently used to create circulating states in a Fermionic ring [Del Pace *et al.*, 2022].

4.1.2 Adiabatic potentials for atomtronics

While most implementations of ring shaped traps rely on optical dipole traps, adiabatic potentials offer an interesting alternative. The idea is to use the shell trap to define a rotationally invariant ellipsoidal trap surface and to hold the atoms at the equator of the shell using an additional optical trap, using a very anisotropic beam, tightly focused in the vertical direction [Heathcote *et al.*, 2008; de Goër de Herve *et al.*, 2021; Morizot *et al.*, 2006]. One advantage of this technique is that the vertical and radial confinements are independently tunable: the radius of the trap and radial trapping frequency are determined by the static magnetic and rf dressing fields properties, while the vertical confinement is controlled by the optical dipole trap parameters. In principle this allows to change the ring size easily and to reach the regime of strong confinement both in the radial and vertical directions, which enables the study of ring traps in the quasi one-dimensional limit.

In practice, at least in our experiment, this ring geometry is extremely hard to achieve [De Rossi, 2016; Guo, 2021; de Goër de Herve, 2018]: small imperfections in the optical dipole trap beam introduce uncontrolled disorder and induce the accumulation of atoms at specific positions, breaking the rotational invariance and higher power in the optical dipole trap induces heating and atom losses. With the current setup, these effects can be mitigated by realizing smaller rings with lower laser power, thus limiting the vertical confinement. To facilitate the realization of a ring trap with this technique it seems necessary to upgrade the glass cell to reach a better beam quality.

Another very promising alternative would be to use time-averaged adiabatic potentials [Gildemeister *et al.*, 2010; Lesanovsky and von Klitzing, 2007] that enable the creation of very smooth and tunable ring shaped atomic waveguides [Pandey *et al.*, 2019; Sherlock *et al.*, 2011]. As this traps are made by a combination of magnetic and rf fields they benefit from a long lifetime and low heating rate, they are highly tunable and in particular can be dynamically controlled to impart rotation [Gildemeister *et al.*, 2012; Pandey *et al.*, 2019] or implement interferometry protocols [Navez *et al.*, 2016]. However time averaging typically reduces the confinement strength, thus it may not be the best strategy to reach the low dimensional regime.

Finally, as demonstrated in section 2.4 gravity compensation in the shell potential also allows to create a ring trap geometry, close to the equator, where the ring is stabilized by the inhomogeneous transverse confinement [Guo *et al.*, 2022]. There are certainly many interesting ideas to explore along this lines by exploiting the available toolbox of adiabatic potentials, including multiple dressing [Bentine *et al.*, 2017] to realize double shell traps [Harte *et al.*, 2018] or the realization of mixtures [Bentine *et al.*, 2020], that could be extended to the ring geometry.

4.1.3 Painted potentials

It is worth mentioning here the success of all optical trapping techniques, see [Gauthier *et al.*, 2021] for a recent review, in the context of atomtronics. Building up on the idea of realizing two-dimensional box trap potentials [Chomaz *et al.*, 2015], that can be shaped using spatial light modulators or digital micro-mirror devices to almost arbitrary pattern [Corman, 2016; Corman *et al.*, 2014; Del Pace *et al.*, 2022; Saint-Jalm *et al.*, 2019]. It enables the design of narrow channels geometries, thus realizing for example simple circuits connecting two reservoirs [Eckel *et al.*, 2016]. Alternatively, by time averaging the fast modulation of the position of a red detuned dipole beam it is possible to paint complex waveguide shapes [Gauthier *et al.*, 2021; Ryu and Boshier, 2015]. All these techniques seem very promising to implement small atomtronics circuits. In contrast to magnetic trapping techniques [Cassettari *et al.*, 2000; Key *et al.*, 2000; Müller *et al.*, 1999] they offer more flexibility as the circuit can be changed simply by reprogramming a light shaping tool.

4.2 Tools to describe one-dimensional superfluids

As my contribution to this topic is mainly theoretical, I give here a few details on the models and tools I used. In the framework of the ANR *SuperRing* we focused on the one-dimensional limit of the circular atomic waveguide. I performed simulations in the weakly-interacting mean-field limit, well captured by the Gross-Pitaevskii equation, while our collaborators in Grenoble studied the strongly-interacting many-body regime, known as the Tonks-Girardeau limit, using the Bose-Fermi mapping technique[1] [Girardeau, 1960]. One interest of working with one-dimensional bosons in a ring trap is that it realizes the Lieb-Liniger model with periodic boundary conditions, for which the many-body ground-state is known exactly [Lieb and Liniger, 1963], as well as the elementary excitation spectrum [Lieb, 1963]. This can be seen as a consequence of the integrability of the system. Interestingly the mean-field limit of this model, the one-dimensional Gross-Pitaevskii equation, is also exactly integrable, in the sense of partial differential equations, which gives access to a analytical toolbox to study this model [Ablowitz and Segur, 1981]. To connect with the LPL experiment, we considered only the case of repulsive interatomic interactions.

4.2.1 The Gross-Pitaevskii equation on a line

Assuming a tight radial confinement in (2.6), allows to factorize the wavefunction $\psi(\boldsymbol{r}, t) = \psi(z,t)e^{-\rho^2/(2a_r^2)}/(\sqrt{\pi}a_r)$ and write an effective one-dimensional equation:

$$i\hbar\frac{\partial}{\partial t}\psi(z,t) = \left(-\frac{\hbar^2}{2M}\frac{\partial^2}{\partial z^2} + V(z,t) - \mu_{1D} + g_{1D}|\psi(z,t)|^2\right)\psi(z,t), \tag{4.1}$$

where $\mu_{1D} = \mu + \hbar\omega_r$ is the one-dimensional chemical potential, $g_{1D} = g_{3D}/(2\pi a_r^2) = 2\hbar\omega_r a_s$, and $V(z,t)$ is a perturbation potential, possibly time dependent. In the context of a ring potential, we impose periodic boundary conditions $\psi(z+L,t) = \psi(z,t)$ and a normalization of the wavefunction: $\int_0^L dz\,|\psi(z,t)|^2 = N$. In the absence of the potential $V(z,t)$ equation (4.1) is integrable, i.e. has infinitely many conserved quantities[2], among which the atom number N, the momentum $P = -i\hbar\int_0^L dz\,\psi(z,t)^*\frac{\partial}{\partial z}\psi(z,t)$ and

[1] In short, hardcore bosons are very similar to free fermions: they avoid each other. In one dimension it leads to the same kind of many-body wave function, up to symmetrization properties.

[2] In the inhomogeneous case, N is always conserved, and E is conserved only if the potential is static.

the energy:

$$E = \int_0^L dz \left(\frac{\hbar^2}{2M} \left| \frac{\partial \psi(z,t)}{\partial z} \right|^2 + \frac{g_{1D}}{2} |\psi(z,t)|^4 \right).$$

The mapping to ring coordinates is obtained through the substitution: $z \to 2\pi r_0 \phi$, where r_0 is the ring radius, and ϕ is the azimuthal angle.

The groundstate of equation (4.1) corresponds to a uniform density $|\psi_0|^2 = n_0 = N/L$, which allows to define characteristic velocity $c_s = (\hbar/M)\sqrt{M g_{1D} n_0/\hbar^2}$ and length scale $\xi = \sqrt{\hbar^2/(2M g_{1D} n_0)}$, corresponding respectively to the speed of sound and healing length. More generally the stationary solutions of (4.1) can be expressed in terms of elliptic functions [Carr *et al.*, 2000]. Another family of analytical solutions can be found in the form of gray solitons: density dips that propagate at constant velocity without deformations [Ablowitz and Segur, 1981]. Using perturbation theory it is possible to show that the small amplitude Bogoliubov excitations correspond to very shallow gray solitons [Tsuzuki, 1971]. On the contrary, a dark, very deep, soliton is a topolgical excitation, carrying a π phase jump, that is associated to a opposite background current in a ring.

To take into account the perturbation potential, it is in general necessary to use numerical simulations and introduce a discretized representation of equation (4.1) that reflects as much as possible the properties of the initial model. In this context it is useful to use the PGPE formalism (2.7), adapted to a one-dimensional ring geometry, using the basis of plane waves: $\phi_k(z) = e^{ikz}/\sqrt{L}$, where $k \in (2\pi/L) \times \mathbb{Z}$. Expanding $\psi(z,t) = \sum_{k \in \mathcal{C}} c_k(t)\phi_k(z)$, where the coherent region is $\mathcal{C} = \{|k| < k_{\text{cut}}\}$, equation (4.1) reads:

$$i\hbar \dot{c}_k(t) = \left(\frac{\hbar^2 k^2}{2M} - \mu_{1D} \right) c_k(t) + \int_0^L dz\, \phi_k(z)^* \left(V(z) + g_{1D}|\psi(z,t)|^2 \right) \psi(z,t). \tag{4.2}$$

Taking advantage of the similarity between the plane wave expansion and the Fourier series representation of a periodic function, the PGPE equation can be simulated efficiently using a discrete grid $k \in \{-k_{\max}, ..., k_{\max}\}$, with $k_{\max} = 3k_{\text{cut}}/2$. The extra wavevectors above k_{cut} are necessary to avoid aliasing in the evaluation of the non linear term, and require the explicit use of a projector onto the coherent region at each direct Fourier transform. This is absolutely necessary when dealing with far from equilibrium states [Polo *et al.*, 2019; Saha and Dubessy, 2021].

4.2.2 Generalized hydrodynamics

In 2016, a breakthrough in the study of out-of-equilibrium one dimensional Bose gases was achieved in the discovery of the generalized hydrodynamics (GHD) equation [Bertini *et al.*, 2016; Castro-Alvaredo *et al.*, 2016] that provides an exact description of the large scale dynamics at arbitrary interaction strength. Importantly for me it is a model that can be solved on a laptop computer, without using a complicated formalism, and it provides a conceptual framework that helps to understand out-of-equilibrium integrable one-dimensional dynamics [Dubail, 2016]. A comprehensive review of the recent developments triggered by this discovery can be found in [Bouchoule and Dubail, 2022]. I contributed to this topic by extending the model to the one-dimensional Bose gas in a box trap, relevant for the experiments [Dubessy *et al.*, 2021].

I introduce here the GHD equations based on simple ideas, without rigorous justification, that I hope still conveys the main ideas beyond this theory. Consider the generic hydrodynamic approach as sketched in figure 4.1: it is very natural to write a conservation law for the generic quantity $Q(z,t)$ as:

$$\frac{\partial}{\partial t}Q(z,t) + \frac{\partial}{\partial z}J(z,t) = 0,$$

where $J(z,t)$ is the associated flux. Now to make use of this equation one has to identify the conserved quantities of the microscopic model and their associated fluxes: this is a priori hard for a one-dimensional system that has in principle infinitely many conserved quantities, because of integrability. From the exact solution of the Lieb-Liniger model [Lieb and Liniger, 1963] we know that any state can be parametrized by a set of quantum numbers, called the rapidities k, that are described by a continuous quasi-particle density distribution $\rho_p(k)$ in the thermodynamic limit. The assumption of GHD is that the coarse-grained $\rho_p(k,z,t)$ are the relevant conserved quantities, associated to a flux $j(k,z,t) = \rho_p(k,z,t)v^{\text{eff}}(k,z,t)$, with a effective velocity given by the implicit equation:

$$v^{\text{eff}}(k,z,t) = \frac{\hbar k}{M} + \int dk'\,\phi(k-k')\rho_p(k',z,t)\left(v^{\text{eff}}(k',z,t) - v^{\text{eff}}(k,z,t)\right), \tag{4.3}$$

where the Lieb-Liniger kernel is defined as:

$$\phi(k-k') = \frac{2k_c}{k_c^2 + (k-k')^2}, \text{ with } k_c = \frac{Mg_{1D}}{\hbar^2}.$$

Finally it is even possible to include an external potential, at the hydrodynamic level, and obtain a GHD equation directly applicable to a trapped one-dimensional Bose gas [Doyon and Yoshimura, 2017]:

$$\frac{\partial \rho_p}{\partial t} + \frac{\partial}{\partial z}\left(\rho_p v^{\text{eff}}\right) - \frac{1}{\hbar}\frac{\partial V(z)}{\partial z}\frac{\partial \rho_p}{\partial k} = 0, \tag{4.4}$$

where $\rho_p \equiv \rho_p(k,z,t)$.

Equation (4.4) is very reminiscent of the one-dimensional collisionless Boltzmann equation, with the crucial difference that the interactions between particles are taken into account in the non-linear equation defining the effective velocity (4.3). This analogy is interesting to interpret equation (4.4) as a phase-space equation, as in section 4.3.2. Importantly, one can recover simply the underlying real space Boson density by integrating over the rapidities: $\rho(z,t) = \int dk\,\rho_p(k,z,t)$, as well as other local quantities as the momentum, energy, ... Finally, from a practical point of view, the GHD equation can be efficiently solved for arbitrary interaction strength and temperature (entering through the initial state distribution). It is particularly simple in the strongly interacting limit, as $\phi(k-k') \to 0$ and the GHD equations become linear and curiously much harder to solve in the mean field limit. The GHD predictions have been tested against experiments and have proven to be robust [Malvania *et al.*, 2021; Schemmer *et al.*, 2019], while being relatively simple to compute even on a laptop computer.

4.2.3 The inverse scattering transform

The last tool I want to introduce to study one dimensional systems is the inverse scattering transform, that allows to capture interesting properties of equation (4.1). I will

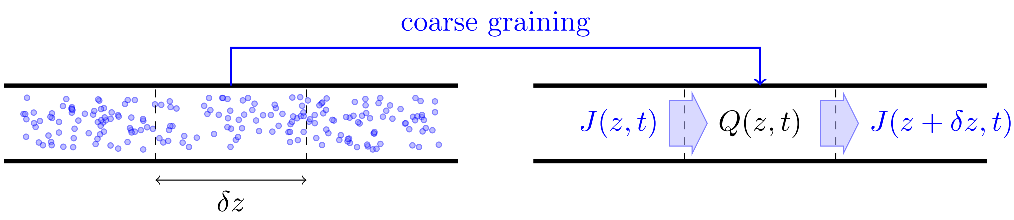

Figure 4.1: Sketch of the hydrodynamic approach, for a narrow channel: an intermediate length scale δz is introduced, over which the microscopic properties of the model are averaged, in general assuming a form of local equilibrium, to define local quantities $Q(z,t)$, associated to fluxes $J(z,t)$ and governed by a continuity equation.

not introduce the general formalism [Ablowitz and Segur, 1981] but highlight a few useful tools. A straightforward calculation shows that equation (4.1) is equivalent to the equation:

$$i\hbar\frac{\partial \mathcal{L}}{\partial t} = [\mathcal{P}, \mathcal{L}]\,, \tag{4.5}$$

for the Lax pair operators:

$$\mathcal{L} \;=\; \frac{i\hbar}{2M}\begin{pmatrix} \frac{\partial}{\partial z} & -\sqrt{k_c}\psi(z,t) \\ \sqrt{k_c}\psi(z,t)^* & -\frac{\partial}{\partial z} \end{pmatrix}, \tag{4.6a}$$

$$\mathcal{P} \;=\; \frac{\hbar^2}{M}\begin{pmatrix} -\frac{\partial^2}{\partial z^2} + \frac{k_c|\psi(z,t)|^2}{2} & \frac{\sqrt{k_c}}{2}\frac{\partial\psi(z,t)}{\partial z} + \sqrt{k_c}\psi(z,t)\frac{\partial}{\partial z} \\ -\frac{\sqrt{k_c}}{2}\frac{\partial\psi(z,t)^*}{\partial z} - \sqrt{k_c}\psi(z,t)^*\frac{\partial}{\partial z} & -\frac{k_c|\psi(z,t)|^2}{2} + \frac{\partial^2}{\partial z^2} \end{pmatrix}, \tag{4.6b}$$

where I recall that $k_c = Mg_{1D}/\hbar^2$ is the inverse length scale associated to two-body interactions in the one-dimensional geometry.

As $\mathcal{L}$ is a hermitian operator, it is diagonalizable and has a real spectrum, $\mathcal{L}v = \zeta v$, and using equation (4.5) it is simple to show that the Lax spectrum ζ is a conserved quantity

$$\frac{\partial\zeta}{\partial t} = 0, \text{ and that the eigenvectors evolve according to } i\hbar\frac{\partial v}{\partial t} = \mathcal{P}v.$$

The main interest of the Lax pair is that the initial nonlinear problem (4.1) is now mapped on a linear eigenvalue problem for the Lax spectrum and that equation (4.6a) defines formally a scattering operator that can be studied by inverse methods in the complex plane once the spectrum is known [Ablowitz and Segur, 1981]. In particular it is sufficient to compute the Lax spectrum for a particular time, for example the initial time, to, in principle, know all the properties of the dynamics, without even solving equation (4.1). This can be used for example to detect and count solitons in a far from equilibrium state [Saha and Dubessy, 2022].

4.3 Out of equilibrium phenomena

We decided to investigate out-of-equilibrium physics in this a one-dimensional system with periodic boundary conditions, and in particular transport phenomena, in the presence of an obstacle that breaks the integrability of the model. The initial idea was to investigate the decay mechanisms of persistent currents in one dimension, following a quench as

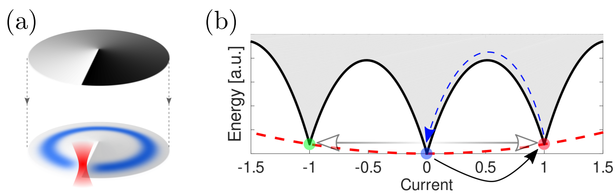

Figure 4.2: (a) A 1D Bose gas on a ring perturbed by a localized barrier is quenched out of equilibrium by phase-imprinting of a quantum of circulation. (b) Energy landscape of the homogeneous system on a ring: states with integer values of the current per particle correspond to local minima. The quench (black arrow) transfers the initial state to the state with one quantum of circulation. Depending on the regime the barrier coherently couple the +1 and -1 current states (light gray arrow) or induce a phase slip to the 0 state (dashed blue arrow).

sketched in Figure 4.2, and evaluate the influence of temperature, comparing the weakly interacting mean-field and the strongly interacting many-body limits. It was useful to evidence the key role of solitons in the phase-slip mechanism in one-dimension, to clarify the link with Bose-Josephson physics and to uncover a universal shock wave dynamics.

4.3.1 Transport through a barrier

In [Polo *et al.*, 2019] we used classical field simulations and time dependent Bose-Fermi mapping to compute the dynamics following a current quench for a one dimensional Bose gas on a ring in the mean-field and strongly interacting limits, respectively. In the mean field limit, a narrow Gaussian barrier, of rms width $\sigma \simeq 4\xi$, and amplitude $V_0 = \lambda_{\mathrm{GP}}\mu$ breaks the integrability. At zero temperature, we identify a dual of the Bose-Josephson physics: the current is initially self-trapped in a steady state and above a critical barrier height undergoes regular and weakly damped oscillations between ± 1, see Figure 4.3a). At finite temperature, modeled using equation (4.2), and averaged over 100 realizations sampling thermal equilibrium for a temperature $k_B T = \mu$, we find that random phase slips induced by the reflection of slow solitons on the barrier, see Figure 4.3c), induce on average an exponential decay of the current, with a rate dependent on λ_{GP}, see Figure 4.3b). The individual event of a soliton reflection on the barrier [Hakim, 1997] can be seen as the adiabatic process connecting the +1 and 0 current states in Figure 4.2.

In the strongly interacting limit, a delta barrier of energy $V_0 = \lambda_{\mathrm{TG}} E_F$, where E_F is the Fermi energy of the hardcore bosons, breaks the integrability, while enabling an analytically tractable solution. At zero temperature it induces coherent phase-slips where each particle of the many-body state oscillates between the ± 1 states, and as λ_{TG} higher energy modes get populated, resulting in a characteristic beatnote pattern, see Figure 4.3d). At finite temperature $k_B T = E_F$, an exponential decay emerges through incoherent phase-slips associated to the initial thermal population in high energy states, see Figure 4.3e). In this regime, the Bose-Josephson duality manifests itself by a transition of the current oscillation frequency ω from a Rabi scaling $\omega \propto \lambda_{\mathrm{TG}}$ to a Josephson-like behavior $\omega \propto \sqrt{\lambda_{\mathrm{TG}}}$. One remarkable feature that we observed in both the mean-field and strongly interacting regime was the apparition of triangular oscillations of the current for large barriers, associated to the propagation of shock fronts in the density dynamics, suggesting that a universal phenomenon was at play, see section 4.3.2.

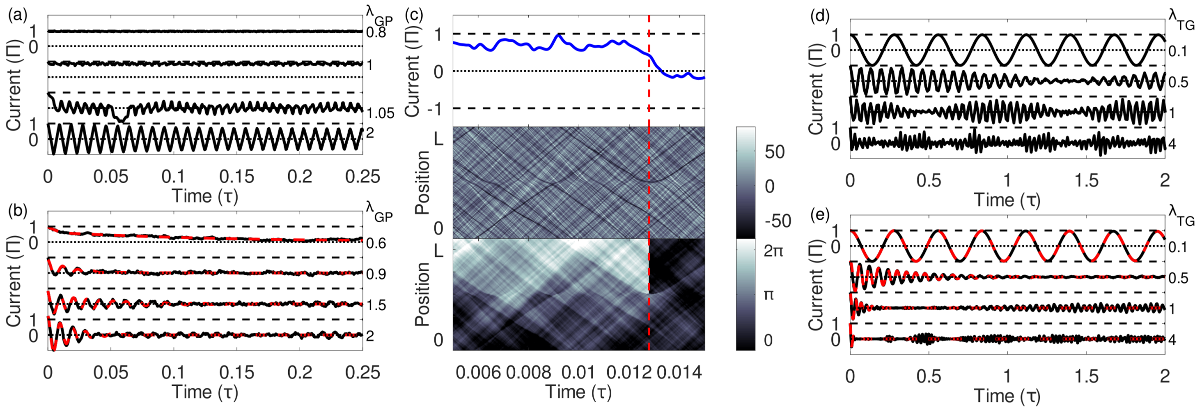

Figure 4.3: Current oscillations and decay in a one dimensional Bose gas at zero temperature for weak (a) and strong (d) interactions, as a function of the barrier strength (λ_{GP} or λ_{TG}). Same curves at finite temperature for weak (b) and strong (e) interactions. (c) Focus on one particular realization for the finite temperature mean-field simulation, evidencing a phase-slip (top panel) at the vertical dashed red line, through the reflection of a soliton on the barrier (middle panel), associated to a singularity in the phase profile (bottom panel).

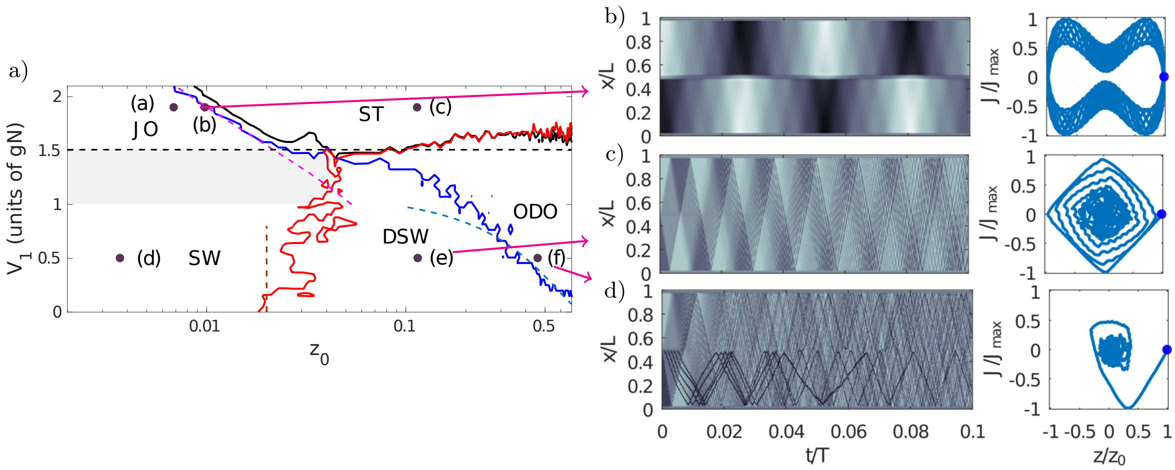

Figure 4.4: a) Dynamical phase diagram as a function of the initial population imbalance z_0 and barrier strength V_1, with empirical boundaries (solid red, blue, black curves) and analytical estimates (dashed curves), separating the self-trapping (ST), Josephson oscillations (JO), shock waves (SW), dispersive shock waves (DSW) and over-damped oscillations (ODO). Examples of density maps and phase-portraits at b) the transition between the self-trapping and Josephson oscillations, in c) the dispersive shock wave and d) over-damped oscillations regimes.

In a separate work [Saha and Dubessy, 2021], I decided to investigate more thoroughly the Bose-Josephson dynamics for a extended zero-temperature one-dimensional Bose gas, using a setup and quench protocol based on a population imbalance between z_0 two reservoirs, following the original proposal [Josephson, 1962]. This requires to work on a ring with two barriers, to define the two reservoirs: one barrier is kept high at all times while the other one is quenched to a lower height V_1 to initiate the dynamics. By varying V_1 and z_0 and analyzing the dynamics we obtain the dynamical phase diagram of Figure 4.4a). At large barriers, we recover the expected Bose-Josephson dynamics, showing the self-trapping transition above a critical initial imbalance, captured by a analytical nonlinear two-mode model. At smaller barriers we evidence a different regime sustained by direct transport above the barrier, mediated by dispersive shock waves, similarly to what is observed for current quenches, see section 4.3.2. At large imbalance and intermediate barriers, the oscillations are overdamped because they are inhibited by soliton reflections on the barrier, see Figure 4.4d), as in the previous study [Polo *et al.*, 2019].

4.3.2 Shock waves in one dimension

To investigate the behavior of current oscillations for large barriers, we decided to study the limiting case of a one-dimensional Bose gas held in a hard wall box. This simplifies a lot the theoretical treatment as the single particle orbitals are known and correspond to all sine functions vanishing at $z = 0$ and $z = L$, the size of the box. It is then possible to use this set of functions to build the exact solution in the weakly and strongly interacting limit, using the PGPE and Bose-Fermi mapping respectively. Interestingly, a one-dimensional system with hard-wall boundary conditions can be mapped exactly onto a one-dimensional system with periodic boundary conditions, provided that the system size is doubled, $z \in [-L, L]$, and that the initial states is a odd function of z. This corresponds to introducing a mirror system to enforce the boundary conditions. As this is valid at the many-body level, it applies also to the GHD equations and enables to write a efficient algorithm to solve them [Dubessy *et al.*, 2021].

By combining these three methods, covering the whole interaction strength range, we were able to uncover the universal features of the post-quench dynamics [Dubessy *et al.*, 2021], as shown in Figure 4.5. Here the quench is obtained by imprinting a current of $v_0 = 0.1 \times c(\gamma)$ on the system, where $c(\gamma)$ is the interaction dependent speed of sound and $\gamma = Mg_{1D}/(\hbar^2 n_0)$ is the dimensionless one-dimensional interaction parameter [Bouchoule and Dubail, 2022; Lieb and Liniger, 1963]. We find that the overall dynamics is very similar, once the time is rescaled by the typical period for the propagation of sound inside the box: $L/c(\gamma)$. A closer inspection of the density profiles, see Figure 4.5b) reveals that the exact solutions in the weakly and strongly interacting limit behave differently at short length scales, however their hydrodynamics behavior is in remarkable agreement. This is confirmed by the evolution of the global current observable, reported in Figure 4.6a): for all three regimes, the current exhibits first triangular oscillations, that damp over a characteristic time $\tau_d \simeq L/v_0$ and become progressively more sinusoidal.

This observation suggests that a universal dephasing mechanism is at play here. In fact, it is indeed expected in the weak interactions limit that the GPE model supports dispersive shock waves, that can be explained and predicted within a simplified analytical modulation theory [El and Hoefer, 2016]. This has been studied before in the context of the dam break problem, and modulation theory predicts that shocks in one dimension occur through the propagation of a rarefaction wave and a shock front with a soliton train.

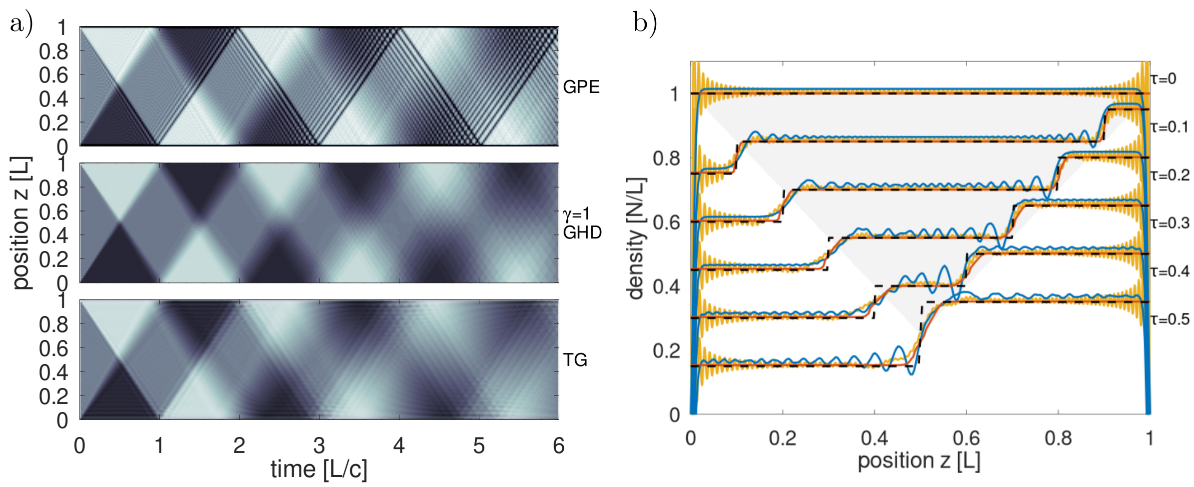

Figure 4.5: a) Density maps for a zero temperature one dimensional Bose gas in a box, after a momentum boost of $0.1 \times c(\gamma)$, at weak (GPE), intermediate (GHD) and strong (TG) interactions. The gray diamond shapes are characteristic of the propagation of shock fronts. For each map the time is rescaled by $L/c(\gamma)$, $c(\gamma)$ being the interaction dependent speed of sound. b) Universality of the shock front propagation during the first quarter period: the weak (blue), intermediate (orange) and strong (yellow) interactions density profiles overlap. Differences are also present: the weakly interacting density presents a soliton train in front of the shock, the strongly interacting density exhibit Friedel oscillations, characteristic of hardcore bosons.

In Figure 4.5b) these features can be seen for the GPE simulation (blue curve), with the rarefaction wave propagating to the right and the soliton train to the left. A prediction of the modulation theory is that the magnitude of the density jumps at the two shock fronts depend on the velocity quench. As shown in Figure 4.6b) the GHD model fully capture this effect in the weak interactions limit, despite the absence of the soliton train in the density profiles, and allows to study the crossover to the strongly interacting limit, where the results are in agreement with the prediction of the most simple long wavelength hydrodynamic theory, as expected from the mapping to free Fermions [Girardeau, 1960].

To understand precisely the physical phenomenon at play, it is interesting to look at the zero-temperature GHD solution, using the quasi-particle occupations $n(k, z, t) = \rho_p(k, z, t)/\rho_s(k, z, t)$ where $\rho_s(k, z, t) = [1/(2\pi)]^{\rm dr}$ is the density of state and the dressing operation is defined as:

$$[h]^{\rm dr}(k) - \int \frac{dk'}{2\pi}\phi(k - k')n(k', z, t)[h]^{\rm dr}(k') = h(k),$$

for any function $h: \ k \rightarrow h(k)$. Using $n(k, z, t)$ the effective velocity (4.3) simply reads: $v^{\rm eff}(k) = (\hbar/M) \times [k]^{\rm dr}/[1]^{\rm dr}$. This picture is useful because it can be shown that at zero temperature, $n(k, z, t)$ is either 0 or 1 and the groundstate of the system can be pictured as a Fermi sea of quasi-particles between rapidities $[-K, K]$ [Doyon *et al.*, 2017]. The quench protocol consists then in boosting the Fermi sea, towards higher rapidities, and because of the hard-wall boundary conditions, results in a deformation of the Fermi sea, see Figure 4.7. In particular, this picture gives an intuitive representation of a rarefaction wave in GHD (encoded in the A–B front) and of a dispersive shock wave (encoded in the

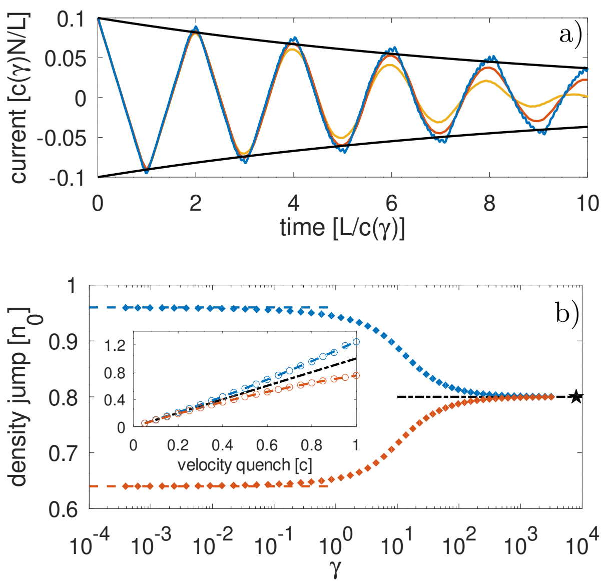

Figure 4.6: a) Dynamics of the total current versus time, in scaled units, for the same parameters as in Figure 4.5, for GPE (blue), GHD (orange) and TG (yellow) regimes and their exponential envelope with a time scale τ_d (black curves). b) Non universal density jumps of the two shock fronts for a large quench of $0.8 \times c(\gamma)$, as predicted by GHD (filled diamonds) for the whole interaction strength range: they are always equal in the strongly interacting limit, but differ in the mean-field. The blue and orange dashed lines are the prediction of the modulation theory. Inset: density jumps as a function of the quench magnitude, in the mean-field limit, comparing the predictions of GHD (circles) and modulation theory (dashed lines).

C–D front). It is interesting to notice that the dispersive shock wave is encoded in GHD as missing quasi-particles in the Fermi sea at a given position between C and D, because holes type excitations are usually associated to the many-body generalization of mean-field solitons [Lieb, 1963]. Finally one can estimate the dephasing time of the oscillations by estimating the velocity at which the two fronts broaden, that is given by the difference of the quasi-particles effective velocities evaluated at A and B (or C and D).

4.3.3 A quantitative study of gray-solitons

Finally the last work I report in this chapter is an attempt to characterize systematically the role of solitons in the one dimensional homogeneous GPE. As we have seen in the previous sections, solitonic excitations appear naturally in the transport dynamics and when many of them occur simultaneously they can be hard to identify. I decided to use the tools of the inverse scattering transform, and in particular the notion of Lax spectrum to study gray solitons. I was inspired by a recent work on surface gravity waves in water, that can be modeled by a non-linear one dimensional Schrödinger equation with attractive interactions, and for which the Lax spectrum allows the identification of bright solitons [Suret *et al.*, 2020]. In this case, the use of the Lax spectrum is quite straightforward as the solitons appear as complex eigenvalues of the Lax spectrum, whereas other excitations remain in the real spectrum.

For the repulsive one-dimensional GPE, the inverse scattering transform predicts that, for a state with asymptotically constant background density, the Lax spectrum is made of two continuous branches, separated by a gap, and that within the gap discrete eigenvalues may be found, each of them being associated to a single soliton [Ablowitz and Segur, 1981]. We tried to turn this general result into a empirical criterion that can be used in a finite size system, more relevant for the experiments [Saha and Dubessy, 2022]. This is not an easy task because for a finite size, discrete representation of the one dimensional GPE (4.1), the Lax operator (4.6a) is a matrix, whose real spectrum is by essence made of

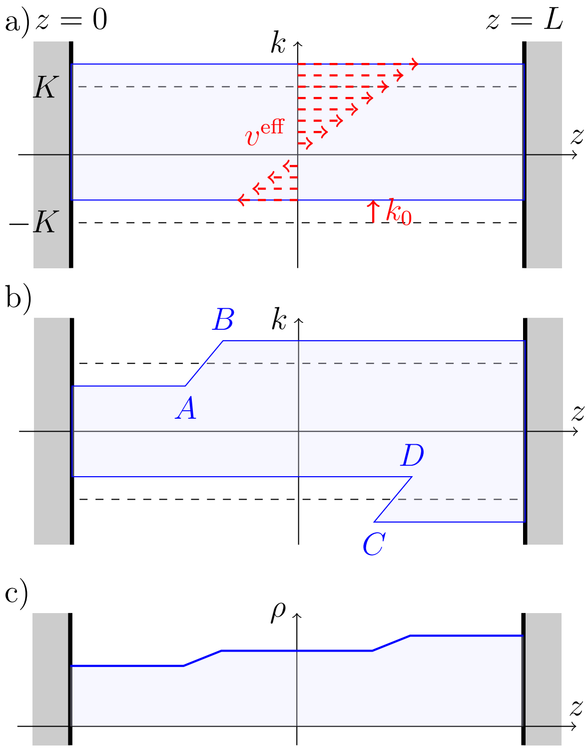

Figure 4.7: Sketch of the GHD dynamics at $T = 0$: the light blue shaded shape indicates the area where $n(k, z, t) = 1$, inside the box potential. a) State just after the quench: boosted Fermi sea. The dashed red arrows indicate the initial effective velocity field of the quasi-particles, for the simple case $\gamma \gg 1$. b) After a time $t < L/(2c)$ the occupation function $\rho_p(k, z, t)$ acquires a non trivial structure and the dynamics is mainly encoded in the position of the points A, B, C and D. c) Sketch of the real space density $\rho(z)$ corresponding to the state of b).

discrete eigenvalues.

Figure 4.8 illustrates this point: a state with a complicated dynamics is generated by first sweeping back and forth a Gaussian obstacle through a one-dimensional system and then, after having removed the obstacle, observing the dynamics with many features propagating at approximately constant velocity, that can be identified by the eye as gray solitons. In this particular case, the Lax spectrum seems almost continuous, i.e. the gap is filled with a large number of eigenvalues corresponding to solitons. However by inspecting the real space profile of the eigenvectors it is clear that some are localized whereas others are delocalized. Recalling that the Lax spectrum is obtained as the solution of $\mathcal{L}v = \zeta v$, where $v = (v_1(z), v_2(z))^T$ is a two component vector, we propose to use as a measure of the localization the ratio:

$$\mathcal{M}(\zeta) = L\frac{\sum_{i=1,2}\max_z |v_i(z)|^2}{\sum_{i=1,2}\max_k |\hat{v}_i(k)|^2},$$

where $\hat{v}_i(k)$ is the Fourier transform of $v_i(z)$. The $\mathcal{M}(\zeta)$ value is equal to one for a fully delocalized state and can be estimated as Lk_cN/π^2 for a dark soliton. In order to distinguish the localized states, we use the phenomenological threshold value $\mathcal{M}_c = 0.05 \times Lk_cN/\pi^2$.

Figure 4.9 shows the distribution of $\mathcal{M}$ values for the Lax spectrum of Figure 4.8, evidencing that the central part of the spectrum is made of localized eigenvalues, corresponding to solitons. Using the criterion $\mathcal{M}(\zeta) > \mathcal{M}_c$ allows to define the boundaries between the two continuous branches and the gap $[\zeta_L, \zeta_R]$ within which lie the discrete, localized, eigenvalues. Using again the results of the inverse scattering transform one can link a discrete Lax eigenvalue to the velocity of the soliton. In particular for a state with a single gray soliton, analytical formulas are available [Saha and Dubessy, 2022] and the discrete Lax eigenvalue is $\zeta = -(\hbar/2M)\times(k+\sqrt{k_cn_0}\sin[\phi])$, where $\hbar k/M$ is the velocity of the background flow, n_0 is the background density and $\phi \in [-\pi/2, \pi/2]$ is an angle related

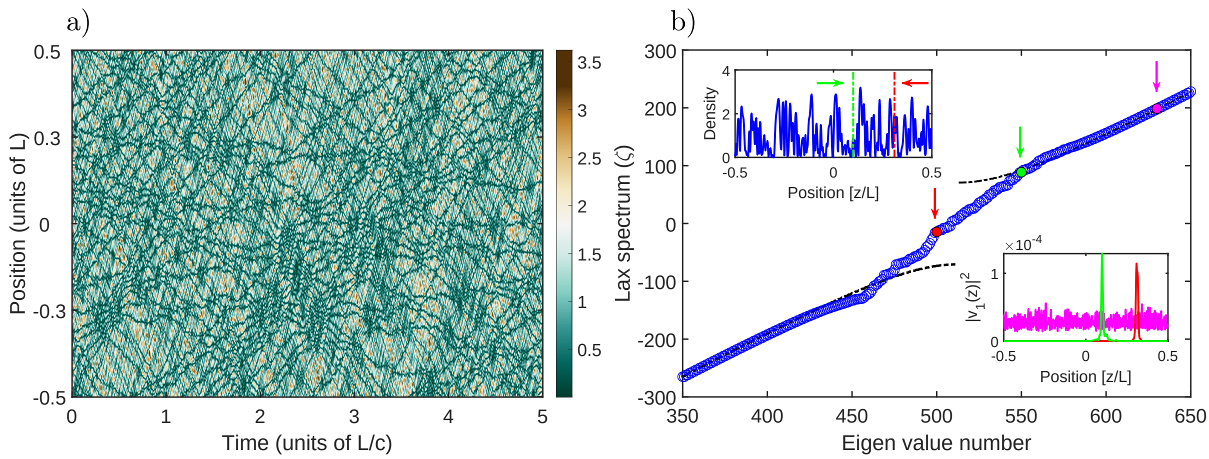

Figure 4.8: a) Density evolution color map for a far from equilibrium state of the one-dimensional GPE, with periodic boundary conditions. Many dark lines can be seen that correspond to the propagation of density dips, associated to gray solitons. b) Corresponding Lax spectrum (blue symbols). The black dashed lines indicate the Lax spectrum of the groundstate of the system, evidencing a clear gap. Upper inset: initial density profile, exhibiting strong density fluctuations. Lower inset: density profiles of three Lax eigenvectors, highlighted in the main figure by the arrows, evidencing that some are localized, the magenta curve, corresponding to a delocalized state is magnified by a factor $\times 15$.

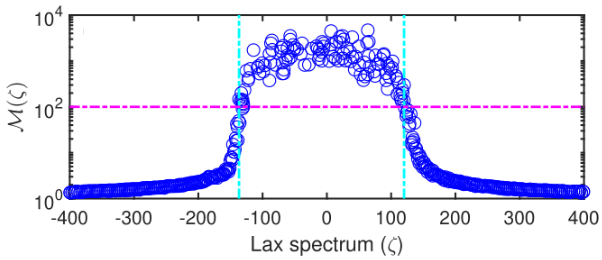

Figure 4.9: Open blue circles: distribution of $\mathcal{M}$ values for the Lax spectrum of Figure 4.8. The dashed-dotted magenta line indicates the phenomenological threshold $\mathcal{M}_c$, that allows to define the two gaps boundaries ζ_L and ζ_R (light blue vertical lines).

to the soliton depth. In that case the gap edges are $\zeta_{L,R} = -(\hbar/2M) \times (k \pm \sqrt{k_c n_0})$ (where the $\pm$ sign refer to the left/right edge) and the gap width $\zeta_R - \zeta_L = \hbar\sqrt{k_c n_0}/M = c_s$ is the speed of sound, while the gap center $\zeta_L + \zeta_R = -\hbar k/(2M)$ is the opposite of half the background velocity. Assuming that this remains true for a far from equilibrium state, we can extract from the Lax spectrum the speed of sound, the background velocity and the distribution of soliton velocities.

Conclusion

In this chapter I introduced tools and theoretical studies that are relevant in the context of one-dimensional atomtronics circuits. In particular I focused on the transport properties in one-dimensional ring and box traps and evidenced the key role played by solitons and dispersive shock waves in the dynamics. By combining the simulation of a current quench using microscopically exact models and generalized hydrodynamic equations we have studied how a localized barrier –a weak-link– breaks the integrability of the system. First we have shown that in the mean-field limit the effect of weak-link could be interpreted as a dual of the Bose-Josephson dynamics for circulation states, with a transition occurring at a critical barrier strength. We also evidenced the role of thermally activated solitons in the phase-slips leading to a dissipation of the average current at finite temperature. For large barrier strengths we revealed a universal long wavelength dynamics in the propagation of shock fronts.

This phenomenon is well understood in the mean-field limit, using the dispersive shock waves analytical framework, and we have shown how generalized hydrodynamics could extend these predictions to arbitrary interaction strengths. In the mean-field limit I also studied the dynamical phase diagram of a one-dimensional Bose-Josephson junction, in the presence of a tunable weak-link and identified the different regimes, involving Bose-Josephson dynamics, dispersive shock waves, solitons and phase-slips. Finally to quantitatively study the gray soliton properties I proposed to use the Lax spectrum as a tool to characterize far from equilibrium states, it would be interesting to apply it to thermal states that contain many spontaneous solitons [Karpiuk *et al.*, 2012, 2015].

What I find especially interesting in the one-dimensional ring with a tunable weak-link is that both the small and large barrier limits are exactly integrable. As a practical consequence both limits can be studied very precisely using a variety of methods which allows a good understanding of their out-of-equilibrium properties, even for non perturbative quenches. In particular, as shown in this chapter, the relaxation to a steady-state can be generically explained by dispersive effects, due to the many-body quasi-particles dispersion relation. It would be interesting to compare the dynamics at a intermediate barrier strength, for which the one-dimensional system is not integrable anymore to test if the microscopic Gross-Pitaevskii model and the generalized hydrodynamics equations give the same results, for the relaxation of global observables, in the mean-field limit. In particular I expect that in this regime the dynamics will be dominated by phase-slips, associated to soliton reflections at the barrier, and this microscopic process is not captured *a priori* by the generalized hydrodynamic equations.

As a last and more speculative thought, I have the intuition that their must be a connection between the Lax spectrum and the quasi-particles rapidity distribution of the generalized hydrodynamics. Indeed in the mean-field limit they both contain the information on all the conserved quantities and I wonder if one can write an effective equation to predict how the Lax spectrum evolves in the presence of an integrability breaking term in the Hamiltonian. This would be interesting to track or predict the trajectories of solitons in a complex environment.

Conclusion

During the last ten years, I contributed to the study of superfluidity in low dimensional Bose gases, both experimentally and theoretically. One of the tools that I developed is a agile eight channel radio-frequency source based on direct digital synthesis. It enables a fine time-dependent control of the adiabatic potential confining a degenerate Bose gas on a two-dimensional surface. This capability is at the heart of ongoing and future projects of the group.

Summary of the habilitation thesis

In the first chapter I presented the design of the *Rubidium* experiment, that is routinely and robustly producing Bose-Einstein condensates for more than ten years. Its main strength is the high quality vacuum in the final chamber and the stability of the adiabatic potential, leading to long lifetimes in the trap. I discussed also its weaknesses and indicated the planned short term upgrades: an update of the laser cooling/imaging system and the implementation of a non-destructive imaging technique.

The second chapter details the tools and know-how we developed to trap and study two-dimensional Bose gases, relying for example on the *in situ* imaging of the collective modes density oscillations. I reported our attempt to compensate the effect of gravity in the shell trap potential to approach the bubble geometry. Unexpectedly we evidenced how the non separability of the potential induces a transition to a stable ring geometry, due to the inhomogeneous transverse trapping energy.

In the third chapter I addressed various manifestations of superfluidity in the experiment, focusing on out-of equilibrium properties. In particular I showed how the local analysis of a collective mode excitation was able to disentangle the respective dynamics of the normal and superfluid phases that co-exist in a harmonic trap. Moreover I reported how we can set the atoms in rotation and control their effective rotation frequency, reaching the fast rotation regime, that provides a new playground to test superfluid transport in a unusual situation.

Finally, the fourth chapter reports theoretical studies of the dynamics in a one-dimensional Bose gas trapped in a ring geometry. I presented the main numerical and theoretical methods I used to address this topic. I showed how the practical question of the stability of super-currents in the presence of an obstacle lead to interesting developments in the context of integrable dynamics: the universal behavior of shock waves in the Lieb-Liniger model and the characterization of grey solitons in far from equilibrium configurations.

Year	Ref.	b' G/cm	$\omega_{\rm rf}$ MHz	Ω_0 kHz	ω_r Hz	ω_z kHz	Remarks
2013	143	210	2.336	27.7	26	1.97	quasi 2D regime reached by
2014	58	210	1	29	33/44	1.91	increasing ω_z, RWA well
2016	46	210	1	30	33.8/48.0	1.83	satisfied ($\Omega_0/\omega_{\rm rf} < 0.03$).
2020	89	55	0.3	48	33.70	0.356	2D vortices ($\omega_z/\omega_r > 8$),
2022	90	82–110	0.3	85	var.	$\sim$0.5	beyond RWA ($\Omega_0/\omega_{\rm rf} > 0.16$).

Table 5.1: Quadrupole dressed trap parameters used for the main experiments presented in this manuscript: b' is the horizontal quadrupole gradient, $\omega_{\rm rf}$ the rf frequency, Ω_0 the rf coupling at the bottom of the trap, ω_r and ω_z are the harmonic trap frequencies at the bottom of the shell potential. When two values are reported for ω_r the trap is anisotropic, due to a non-circular rf polarization.

Table 5.1 summarizes the dress trap parameters of the experiments reported in chapters 2 and 3. We first used high gradients and relatively small rf couplings to increase the vertical trapping frequency to $\omega_z \sim 2\pi \times 2\,\mathrm{kHz}$. The idea was to match the typical values of other experiments in the quasi-two-dimensional regime to be able to use the same analysis tools and enable a study of Kosterlitz-Thouless physics. In order to have a reasonable shell radius the rf frequency was in the megahertz range. Later, it was more convenient to decrease the gradient and increase the rf coupling, while keeping a very oblate geometry, to study rotating Bose gases. Indeed it helps to limit the Landau-Zener losses, inherent to adiabatic potentials, and give access to the long time scale necessary to achieve thermalization in a rotating frame. To keep approximately the same shell radius and facilitate the fine-tuning of the rf polarization we work since then with a fixed rf frequency of 300 kHz.

Ongoing projects

As mentioned in chapter 3 we are still investigating the vortex lattice melting transition that we observed. In principle it would require the computation of correlation functions characterizing the translational and orientational order. However these are strongly affected by the inhomogeneity of the density profile and finite size effects which are not trivial to account for. One promising alternative is the investigation of the proliferation of defects in the vortex lattice as the rotation frequency increases. Indeed the KTHNY theory predicts that the melting occurs through first the apparition of dislocations and then disclinations. Figure 5.1 presents an example of such an analysis for a particular realization of the experiment.

In order to assess the finite size effects we will study the melting transition using a finite temperature stochastic projected Gross-Pitaevskii simulation, as described in section 2.2.2. To this end I have developed a spectral scheme adapted to the harmonic plus quartic quasi two-dimensional model based on a Laguerre-Gauss basis for the in-plane dynamics and Hermite-Gauss basis for the transverse confinement. The simulation will be used to sample the grand canonical classical field ensemble in a rotating frame, and the resulting density profiles will be analyzed following the same protocol as the measured profiles.

Finally, to investigate more precisely the collective modes in the dynamical ring configuration described in 3.3.2, we are currently developing a non-destructive imaging scheme

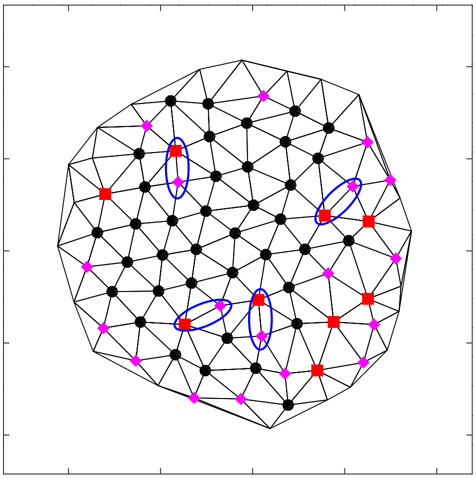

Figure 5.1: Vortex lattice deduced from a map of the vortices positions, as explained in section 3.2.3. The lattice sites with five, six and seven neighbors are marked by magenta diamonds, black disks and red squares, respectively. Dislocations appear as 5-7 pairs that may unbound to form disclinations (an isolated 5 or 7 neighbors site). A few dislocations are highlighted by the blue ellipses. Finite size effects explain the existence of sites with less than five neighbors close to the boundary of the vortex lattice.

that will enable the recording of a full movie at each run of the experiment. If it works well, this will help to study the collective modes behavior as a function of the rotation frequency. This project is at the heart of an ongoing PhD thesis that I co-supervise.

Future research directions

To conclude this manuscript, I would like to discuss a few perspectives and future research directions. To my opinion the most logical next step is to combine the results of chapters 2 and 3 to explore the physics of rotating superfluids on a curved two-dimensional surface. The idea would be either to prepare a rotating superfluid at the bottom of the shell potential and then compensate partially the gravity to let the rotating gas expand on the surface, going beyond the harmonic plus quartic approximation or to first compensate the gravity and try to spin up directly the superfluid in a quartic or ring shaped potential. One unique feature of the shell trap is the possibility to study with these scenarios the competition between curvature and rotation in the dynamics.

These questions are prominent in the field of geophysics, when one tries to model the classical hydrodynamic transport in a thin layer of the atmosphere. In these systems the competition between curvature and rotation gives rise to special classes of waves, as for example Rossby waves with a peculiar dispersion relation. I think that our experiment will be able to produce an analog simulation of this phenomenon and that we have all the tools to observe quantum Rossby waves. I have initiated a collaboration with the group of Sergey Nazarenko, that will provide a theoretical support and bring an expertise in geofluids modeling. In principle the approximations used to derive the dispersion relation of Rossby waves from classical hydrodynamics equations can be adapted to the equations describing superfluid hydrodynamics.

Interestingly the geofluid – curved superfluid analogy opens an exciting perspective in the study of two-dimensional turbulence. Classical turbulence is known to be a very hard problem, owing to the complexity of the underlying Navier-Stokes equations, and superfluid hydrodynamics allows to build models of turbulent phenomena, in a controlled environment [Nazarenko, 2011]. In superfluid two-dimensional turbulence it is interesting to study the dynamics of vortices and anti-vortices [Gauthier *et al.*, 2019]. In order to address this issue, I want to improve the vertical imaging system on the experiment to be able to see the vortices *in situ*. To achieve this, I plan to use the $5S-6P$ transition of ^{87}Rb to benefit from the smaller wavelength and achieve a sub-micrometer imaging resolution. With this tool, an outstanding achievement would be to study the mechanisms explaining the formation of the great red spot on Jupiter, that will appear through vortex clustering in a curved superfluid.

Appendix A

The dressed quadrupole trap in the rotating wave approximation

In this appendix I consider the dressed quadrupole trap in the rotating wave approximation, described by equation (2.16), in the case of the most general rf polarization (1.6). I recall here these two equations:

$$\begin{aligned} V(\boldsymbol{r}) &= \hbar\sqrt{(\omega_{\mathrm{rf}}-\alpha\ell)^2+\Omega(\boldsymbol{r})^2}+Mgz, \\ \Omega(\boldsymbol{r}) &= \frac{\Omega_0}{\sqrt{2}}\left(1-\frac{\rho^2-2\sqrt{\eta(1-\eta)}(x'^2-y'^2)}{2\ell^2}-\frac{2z}{\ell}(2\eta-1)\right)^{1/2}, \end{aligned}$$

where $\eta\in[0,1]$. The (x',y') axes are rotated with respect the (x,y) axes, by an angle ϕ' dependent on the rf polarization, see equation (1.5).

In order to study the properties of this potential it is first interesting to consider the mapping:

$$(x',y',z)\to\ell(\sin[\chi]\cos[\phi],\sin[\chi]\sin[\phi],\cos[\chi]/2), \tag{A.1}$$

which restores a spherical symmetry and simplifies the expressions. The potential now reads:

$$V(\ell,\chi,\phi)=\hbar\sqrt{(\omega_{\mathrm{rf}}-\alpha\ell)^2+\Omega(\chi,\phi)^2}+Mg\frac{\ell}{2}\cos[\chi],$$

where the coupling only depends on the angles (χ,ϕ) on the sphere:

$$\Omega(\chi,\phi)=\frac{\Omega_0}{\sqrt{2}}\left(1-\sin[\chi]^2\,\frac{1-2\sqrt{\eta(1-\eta)}\cos[2\phi]}{2}-(2\eta-1)\cos[\chi]\right)^{1/2}.$$

The coupling vanishes for $\phi_0=\pm\pi/2$ (i.e. in the direction of y'), and for an angle $\cos[\chi_0]=(2\eta-1)/(1+2\sqrt{\eta(1-\eta)})$. This results, in general, in two holes in the potential: for example with a linear polarization ($\eta=1/2$) the holes are at the equator ($\cos[\chi_0]=0$), while for a σ^+ circular polarization the holes coalesce at the north pole ($\cos[\chi_0]=1$). The coupling is maximal and equal to $\sqrt{\eta}\Omega_0$ at the south pole when $\eta>1/2$, at the north pole when $\eta<1/2$, and along the meridians $\phi=0$ and π (i.e. at the intersection of the shell surface and the xz plane) when $\eta=1/2$.

The minimal potential surface, i.e. the two-dimensional shell surface, is obtained as:

$$\frac{\partial V}{\partial\ell}=0\ \Rightarrow\ \ell_{\mathrm{eq}}(\chi,\phi)=r_0\left(1-\frac{\epsilon\cos[\chi]}{\sqrt{1-\epsilon^2\cos[\chi]^2}}\frac{\Omega(\chi,\phi)}{\omega_{\mathrm{rf}}}\right),$$

where $r_0 = \omega_{\mathrm{rf}}/\alpha$ and $\epsilon = Mg/(2\hbar\alpha)$. The potential on this surface is:

$$V_{\mathrm{eq}}(\chi,\phi) = \frac{Mgr_0}{2}\cos[\chi] + \sqrt{1-\epsilon^2\cos[\chi]^2}\,\hbar\Omega(\chi,\phi).$$

It has a well defined minimum at the south pole ($\chi = \pi$), provided that:

$$Mgr_0 > \hbar\Omega_0\frac{\sqrt{\eta}(1-3\epsilon^2)+(1-\epsilon^2)\sqrt{1-\eta}}{\sqrt{1-\epsilon^2}} \geq \hbar\Omega_0\frac{\sqrt{\eta}(1-3\epsilon^2)-(1-\epsilon^2)\sqrt{1-\eta}\cos[2\phi]}{\sqrt{1-\epsilon^2}},$$

where the inequality is saturated for $\phi = \pm\pi/2$ (when $\eta < 1$). This condition is a generalization of the criterion (2.22) to a arbitrary polarization. It shows that for a non perfect circular polarization, gravity compensation by reducing r_0 (i.e. increasing the gradient), results in the formation of a double well-like potential, in which the minima are located in the direction of the holes. This provides an extremely sensitive probe of the rf polarization and we use it for the fine tuning of the circular polarization [Guo, 2021; Rey, 2023].

I now focus on the equilibrium position at the south pole, for a arbitrary polarization, assuming that the above inequality is satisfied. The equilibrium position is

$$z_{\mathrm{eq}} = -\frac{r_0}{2}\left(1+\frac{\epsilon}{\sqrt{1-\epsilon^2}}\frac{\sqrt{\eta}\Omega_0}{\omega_{\mathrm{rf}}}\right),$$

and expanding to second order the potential (in Cartesian coordinates) one gets the three oscillation frequencies:

$$\begin{aligned}
\omega_z &= 2\alpha\sqrt{\frac{\hbar}{M\sqrt{\eta}\Omega_0}}(1-\epsilon^2)^{3/4},\\
\omega_{x'} &= \sqrt{\frac{g}{4|z_{\mathrm{eq}}|}}\left(1-\frac{\hbar\Omega_0}{2Mg|z_{\mathrm{eq}}|}\sqrt{1-\epsilon^2}\frac{\eta+\sqrt{\eta(1-\eta)}}{\sqrt{\eta}}\right)^{1/2},\\
\omega_{y'} &= \sqrt{\frac{g}{4|z_{\mathrm{eq}}|}}\left(1-\frac{\hbar\Omega_0}{2Mg|z_{\mathrm{eq}}|}\sqrt{1-\epsilon^2}\frac{\eta-\sqrt{\eta(1-\eta)}}{\sqrt{\eta}}\right)^{1/2}.
\end{aligned}$$

The strongest in-plane confinement occurs along the y' axis, that also corresponds to the direction of the holes. The in-plane anisotropy is given by:

$$\varepsilon = \frac{\omega_{y'}^2-\omega_{x'}^2}{\omega_{y'}^2+\omega_{x'}^2} = \frac{\frac{\hbar\Omega_0}{2Mg|z_{\mathrm{eq}}|}\sqrt{1-\epsilon^2}\sqrt{1-\eta}}{1-\frac{\hbar\Omega_0\sqrt{\eta}}{2Mg|z_{\mathrm{eq}}|}\sqrt{1-\epsilon^2}} = \frac{\sqrt{1-\epsilon^2}\sqrt{1-\eta}}{\frac{2\epsilon\omega_{\mathrm{rf}}}{\Omega_0}+\frac{\sqrt{\eta}}{\sqrt{1-\epsilon^2}}(3\epsilon^2-1)},$$

while the average frequency is

$$\omega_0^2 = \frac{\omega_{y'}^2+\omega_{x'}^2}{2} = \frac{g}{4|z_{\mathrm{eq}}|}\left(1-\frac{\hbar\Omega_0\sqrt{\eta}}{2Mg|z_{\mathrm{eq}}|}\sqrt{1-\epsilon^2}\right).$$

This formulas are useful in the context of rotating Bose gases, see section 3.2.1, as we use a rotating anisotropy to spin up the superfluid.

Appendix B

The dressed quadrupole trap beyond the rotating wave approximation

I derive in this appendix the formalism used to describe the atom-field interaction beyond the rotating wave approximation, based on a Floquet expansion. This derivation is quite technical and I provide first a brief summary and I discuss the main results. For the case of a quadrupole trap dressed by a circularly polarized rf field, with respect to the vertical axis, only three parameters are relevant: the rf frequency ω_{rf}, the maximum atom-field coupling Ω_0 and the quadrupole gradient α (in frequency units). The Floquet expansion is controlled by the dimensionless parameter $\Omega_0/\omega_{\mathrm{rf}}$. Because of the adiabatic potential the atoms are located close to a resonant surface defined by $\ell = r_0 = \omega_{\mathrm{rf}}/\alpha$, where $\ell^2 = \rho^2 + 4z^2$. If the polarization is not purely circular two additional dimensionless parameters are necessary to describe the atom-field coupling (the angles Θ and Φ). In addition, the effect of gravity enters through a gravitational sag from the surface, controlled by the dimensionless parameter $\epsilon = Mg/(2\hbar\alpha)$, where M is the atomic mass. Similarly if the system is in a rotating frame the equilibrium surface will be deformed by centrifugal effects.

I will show that it is necessary to include additional beyond RWA effects, that are often neglected, to describe properly the atom-field coupling on the full shell surface. In particular the effective polarization seen by the atoms depends on the position on the resonant surface, resulting in a renormalization of the couplings (due to the π component) and an effective light-shift (due to the off resonant σ^- component). As I will show below this is crucial to obtain a quantitative agreement with the experiments.

The main result is that the effective Hamiltonian for an atom in a dressed quadrupole trap is:

$$\hat{H} = \frac{\hat{\boldsymbol{p}}^2}{2M} + \hbar\sqrt{(\delta(\boldsymbol{r}) - \Sigma(\boldsymbol{r}))^2 + \tilde{\Omega}(\boldsymbol{r})^2} + Mgz, \tag{B.1}$$

where $\delta(\boldsymbol{r}) = \omega_{\mathrm{rf}} - \alpha\ell$ is the local detuning, $\tilde{\Omega}(\boldsymbol{r}) = j_0\Omega_+(\boldsymbol{r}) - j_2\Omega_-(\boldsymbol{r})$ is the effective rf coupling, $\Omega_\pm(\boldsymbol{r}) = \Omega_0/2 \times (1 \mp 2z/\ell)$ are the rf coupling corresponding to the local $\sigma^\pm$ polarization, the coefficients $j_n \equiv J_n(\Omega_\pi(\boldsymbol{r})/\omega_{\mathrm{rf}})$ are defined in terms of Bessel functions of the first kind and $\Omega_\pi(\boldsymbol{r}) = \Omega_0\rho/\ell$ is the rf coupling induced by the π polarization. In equation (B.1) $\Sigma(\boldsymbol{r})$ is a shift of the resonance induced by the off resonant coupling terms, and approximately given by, at leading order:

$$\Sigma(\boldsymbol{r}) \simeq \frac{j_0\Omega_-(\boldsymbol{r})(j_0\Omega_-(\boldsymbol{r}) - 2j_2\Omega_+(\boldsymbol{r}))}{4\omega_{\mathrm{rf}}}. \tag{B.2}$$

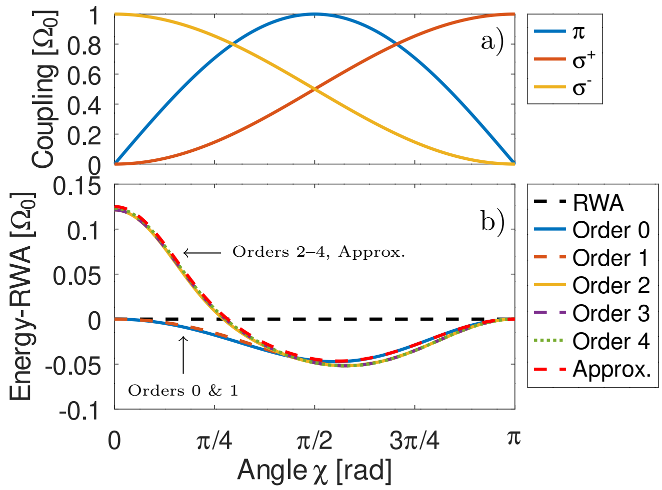

Figure B.1: a) Relative strength of the π, σ^+ and σ^- rf couplings as a function of the angle χ. At the south (north) poles, where $\chi = \pi$ (0), the polarization is purely circular, while at the equator ($\chi = \pi/2$) the π polarization is dominant. b) Comparison of the dressed state energy on the resonant surface computed with different levels of approximation. The RWA value is taken as reference. The computation is done with $\Omega_0/\omega_{\mathrm{rf}} = 0.5$, a value larger than the one used in the experiments.

Figure B.1 shows the main consequences of beyond RWA terms for a quadrupole trap dressed by a circularly polarized rf field. First, as the angle χ (defined through the map of equation (A.1)) decreases, from π to 0, the effective local rf field polarization changes, due to the rotation of the static magnetic field, as sketched in figure 1.3. It is σ^+ circularly polarized at the south pole, σ^- at the north pole, and the largest component is the π polarization at the equator. As mentioned above, and detailed in the following sections, this affects the effective coupling strength. One way of assessing the importance of beyond RWA terms is to focus on the resonant surface $\delta(\boldsymbol{r}) = 0$, corresponding to the ellipsoid defined by $\ell = r_0$ and compute the magnetic energy on this surface as a function of the angle χ. Figure B.1b) shows that the Floquet expansion converges at the second order, at least for the chosen coupling strength $\Omega_0/\omega_{\mathrm{rf}} = 0.5$, and that it is well captured by the simple analytic model of equations (B.1) and (B.2).

Finally I will also briefly discuss the terms that are often neglected and discarded when writing the adiabatic potential Hamiltonian and that are responsible for Landau-Zener losses [Burrows *et al.*, 2017] or spin-orbit coupling terms [Corman, 2016].

B.1 General formalism

I describe here the general formalism for the interaction of an atom in its electronic ground-state and both a static magnetic field and a time-dependent, periodic, radio-frequency field. I assume that the atom-field coupling can be described using the total spin operator $\hat{\boldsymbol{F}}$ and that the Hamiltonian reads:

$$\hat{H} = \frac{\hat{\boldsymbol{p}}^2}{2M} + \frac{\mu_B g_F}{\hbar}\hat{\boldsymbol{F}} \cdot \left(\boldsymbol{B}_0(\boldsymbol{r}) + \boldsymbol{B}(\boldsymbol{r}, t)\right), \tag{B.3}$$

where M is the atomic mass, $\hbar$ is the reduced Planck constant, μ_B is the Bohr magnetron, g_F the gyromagnetic factor, $\boldsymbol{B}_0$ and $\boldsymbol{B}$ are the static and oscillating magnetic fields, respectively. For the sake of simplicity I will assume that $g_F > 0$. I first focus on the atom field coupling and I will discuss later the effect of additional terms in equation (B.3), as for example the gravitational potential or the effect of rotation.

To study the Hamiltonian (B.3) it is first convenient to perform the spin rotation:

$$\hat{U}_0 = \exp\left[i\frac{\pi}{\hbar}\boldsymbol{n}_0(\boldsymbol{r}) \cdot \hat{\boldsymbol{F}}\right], \tag{B.4}$$

that amounts to choose the quantization axis along the local static magnetic field $\boldsymbol{B}_0(\boldsymbol{r})$ direction and where the unitary vector is:

$$\boldsymbol{n}_0(\boldsymbol{r}) = \frac{\boldsymbol{B}_0(\boldsymbol{r}) + |\boldsymbol{B}_0(\boldsymbol{r})|\,\boldsymbol{e}_z}{\sqrt{2\,|\boldsymbol{B}_0(\boldsymbol{r})|}\sqrt{|\boldsymbol{B}_0(\boldsymbol{r})| + \boldsymbol{B}_0(\boldsymbol{r})\cdot\boldsymbol{e}_z}}.$$

The new Hamiltonian $\hat{H}_0 = \hat{U}_0^\dagger \hat{H} \hat{U}_0$ can be written explicitly:

$$\hat{H}_0 = \frac{\left[\hat{\boldsymbol{p}} - \hat{\boldsymbol{A}}_0(\boldsymbol{r})\right]^2}{2M} + \omega_0(\boldsymbol{r})\hat{F}_z + \frac{\mu_B g_F}{\hbar}\hat{\boldsymbol{F}}\cdot\tilde{\boldsymbol{B}}(\boldsymbol{r},t),$$

where I defined the local Larmor frequency: $\omega_0(\boldsymbol{r}) = \mu_B g_F\,|\boldsymbol{B}_0(\boldsymbol{r})|\,/\hbar$. The spin rotation induces a spin-orbit coupling through the vector field $\hat{\boldsymbol{A}}_0(\boldsymbol{r}) = i\hbar\hat{U}_0^\dagger\boldsymbol{\nabla}\hat{U}_0$ and an effective oscillating field:

$$\tilde{\boldsymbol{B}}(\boldsymbol{r},t) = 2\boldsymbol{n}_0(\boldsymbol{r})\left(\boldsymbol{B}(\boldsymbol{r},t)\cdot\boldsymbol{n}_0(\boldsymbol{r})\right) - \boldsymbol{B}(\boldsymbol{r},t).$$

This equation shows that even if the rf magnetic field is homogeneous, i.e. $\boldsymbol{B}(\boldsymbol{r},t) \equiv \boldsymbol{B}(t)$, the effective field contributing to the coupling is inhomogeneous, due to change of the local orientation of the quantization axis in the inhomogeneous static magnetic field.

The fact that we require that the atomic spin follows adiabatically the external magnetic field results in the modification of the kinetic energy term of the Hamiltonian. This modification can be interpreted as a gauge field that induces a spin-orbit coupling term as it depends on the $\hat{F}_{x,y,z}$ operators. This gives rise to two different kind of terms. On the one hand terms that are proportional to $\hat{F}_z$ or the identity and that do not change the spin state: these induce extra terms in the effective Hamiltonian that act as gauge fields [Corman, 2016]. On the other hand, the remaining terms induce spin-flips that can be seen as loss channels [Burrows *et al.*, 2017]. As I will show below, see section B.3, both terms are usually small in the experiment.

Introducing now the spin raising and lowering operators $\hat{F}_\pm = \hat{F}_x \pm i\hat{F}_y$ results in:

$$\hat{H}_0 = \frac{\left[\hat{\boldsymbol{p}} - \hat{\boldsymbol{A}}_0(\boldsymbol{r})\right]^2}{2M} + \left[\omega_0(\boldsymbol{r}) + \Omega_z(\boldsymbol{r},t)\right]\hat{F}_z + \Omega_+(\boldsymbol{r},t)\hat{F}_+ + \Omega_-(\boldsymbol{r},t)\hat{F}_-,$$

where I defined the time dependent couplings:

$$\Omega_z(\boldsymbol{r},t) = \frac{\mu_B g_F}{\hbar}\tilde{B}_z(\boldsymbol{r},t), \tag{B.5a}$$

$$\Omega_\pm(\boldsymbol{r},t) = \frac{\mu_B g_F}{2\hbar}\left(\tilde{B}_x(\boldsymbol{r},t) \mp i\tilde{B}_y(\boldsymbol{r},t)\right). \tag{B.5b}$$

I now remove the time dependence in the term involving $\hat{F}_z$ using the spin rotation:

$$\hat{R} = \exp\left[-i\left(\omega t + f(\boldsymbol{r},t)\right)\frac{\hat{F}_z}{\hbar}\right],$$

where $f(\boldsymbol{r},t) = \int^t dt'\,\Omega_z(\boldsymbol{r},t')$ and $\omega = 2\pi/T$ where T is the period of the oscillating field $\boldsymbol{B}(\boldsymbol{r},t)$. This transformation results in $\hat{H}_1 = \hat{R}^\dagger\hat{H}_0\hat{R} - i\hbar\hat{R}^\dagger\partial_t\hat{R}$ and $\hat{\boldsymbol{p}} \to \hat{\boldsymbol{p}} - \boldsymbol{\nabla}f(\boldsymbol{r},t)\hat{F}_z$, giving:

$$\hat{H}_1 = \frac{\left[\hat{\boldsymbol{p}} - \hat{\boldsymbol{A}}_1(\boldsymbol{r},t)\right]^2}{2M} - \delta(\boldsymbol{r})\hat{F}_z + \Omega_+(\boldsymbol{r},t)e^{i(\omega t + f(\boldsymbol{r},t))}\hat{F}_+ + \Omega_-(\boldsymbol{r},t)e^{-i(\omega t + f(\boldsymbol{r},t))}\hat{F}_-, \tag{B.6}$$

where the local detuning is $\delta(\boldsymbol{r}) = \omega - \omega_0(\boldsymbol{r})$ and the spin-orbit coupling now reads:

$$\hat{\boldsymbol{A}}_1(\boldsymbol{r},t) = \boldsymbol{\nabla} f(\boldsymbol{r},t)\hat{F}_z + \hat{R}^\dagger \hat{\boldsymbol{A}}_0(\boldsymbol{r})\hat{R}.$$

Hamiltonian (B.6) is time periodic with a period T: it is therefore natural to solve it using a Fourier series expansion (or Floquet expansion), that I detail now.

Assuming that $\boldsymbol{B}(\boldsymbol{r},t)$ has no dc component, $f(\boldsymbol{r},t)$ is also periodic in time, with the same period T and I may introduce the formal Fourier series expansion:

$$e^{if(\boldsymbol{r},t)} = \sum_n c_n(\boldsymbol{r}) e^{in\omega t}. \tag{B.7}$$

Following the Floquet formalism I look now for a solution of the Schrödinger equation under the form:

$$|\psi\rangle = \sum_n e^{i(n\omega - E/\hbar)t} |\psi_n\rangle ,$$

where $\langle\psi_n|\psi_m\rangle = 0$ for $n \neq m$, and the normalization of the wavefunction implies that $\sum_n \langle\psi_n|\psi_n\rangle = 1$. The eigenvalue equation $E|\psi\rangle = \hat{H}_1|\psi\rangle$ results in a infinite system of coupled equations:

$$E|\psi_n\rangle = \hat{D}_n(\boldsymbol{r})|\psi_n\rangle + \sum_{k\neq 0}\left[\hat{K}_k(\boldsymbol{r}) + \hat{V}_k(\boldsymbol{r})\right]|\psi_{k+n}\rangle , \tag{B.8}$$

where I introduced the effective (time averaged) kinetic energy operator:

$$\hat{K}_k(\boldsymbol{r}) = \frac{1}{T}\int_0^T dt\, e^{ik\omega t}\frac{\left[\hat{\boldsymbol{p}} - \hat{\boldsymbol{A}}_1(\boldsymbol{r},t)\right]^2}{2M}, \tag{B.9}$$

the atom-field couplings:

$$\hat{V}_k(\boldsymbol{r}) = \sum_l \left[\tilde{\Omega}_+^{(l+1+k)}(\boldsymbol{r})c_l(\boldsymbol{r})\hat{F}_+ + \tilde{\Omega}_-^{(l+1-k)}(\boldsymbol{r})c_l(\boldsymbol{r})^*\hat{F}_-\right], \tag{B.10}$$

and the coupling harmonics:

$$\tilde{\Omega}_\pm^{(k)}(\boldsymbol{r}) = \frac{1}{T}\int_0^T dt\,\Omega_\pm(\boldsymbol{r},t)e^{\pm ik\omega t}. \tag{B.11}$$

The block diagonal term (acting within the n-th manifold) is:

$$\hat{D}_n(\boldsymbol{r}) = n\hbar\omega\hat{I} - \delta(\boldsymbol{r})\hat{F}_z + \hat{K}_0(\boldsymbol{r}) + \hat{V}_0(\boldsymbol{r}). \tag{B.12}$$

Equations (B.8), (B.9), (B.10), (B.11), and (B.12) do not depend explicitly on time and the eigenvalues can be computed using standard matrix diagonalization, using an appropriate truncation of the infinite set of coupled equations. The convergence of the Floquet expansion approximation can be tested by varying the truncation order. Until now I have used a very general formalism that can account for any static field, rf polarization, eventually include harmonics in the oscillatory field and model also the spin-orbit coupling terms.

I have now all the tools to perform a systematic and controlled study of the system. The main remaining difficulties are: the computation of the time dependent couplings of

Eq. (B.5), the determination of the Fourier series coefficients of Eq. (B.7) and the coupling harmonics of Eq. (B.11). Finally to obtain the adiabatic potential I have to diagonalize the eigenvalue equations. The effect of gravity or rotation can be taken into account by substituting:

$$\hat{D}_n(\boldsymbol{r}) \to \hat{D}_n(\boldsymbol{r}) + Mgz\hat{I} - \boldsymbol{\Omega}_{\mathrm{rot}} \cdot \hat{\boldsymbol{L}},$$

where $\hat{\boldsymbol{L}} = \boldsymbol{r} \times \left(\hat{\boldsymbol{p}} - \hat{\boldsymbol{A}}_1(\boldsymbol{r}, t)\right)$.

A common approximation consists in assuming that the oscillating field $\boldsymbol{B}(\boldsymbol{r}, t)$ is purely sinusoidal with time, such that only the ± 1 harmonics contribute directly in equation (B.10), and the atom-field coupling (B.10) writes:

$$\hat{V}_k(\boldsymbol{r}) = \tilde{\Omega}_+^{(1)}(\boldsymbol{r})c_{-k}(\boldsymbol{r})\hat{F}_+ + \tilde{\Omega}_-^{(1)}(\boldsymbol{r})c_k(\boldsymbol{r})^*\hat{F}_- + \tilde{\Omega}_+^{(-1)}(\boldsymbol{r})c_{-k-2}(\boldsymbol{r})\hat{F}_+ + \tilde{\Omega}_-^{(-1)}(\boldsymbol{r})c_{k-2}(\boldsymbol{r})^*\hat{F}_-.$$

Finally, as I will show explicitly for the quadrupole dressed trap example, see section B.3, the spin orbit coupling terms $\hat{K}_k$ are usually very small in the adiabatic potential, and it is reasonable to keep only the zero-order term:

$$\hat{K}_0 = \frac{1}{T}\int_0^T dt \, \frac{\left[\hat{\boldsymbol{p}} - \hat{\boldsymbol{A}}_1(\boldsymbol{r}, t)\right]^2}{2M} \simeq \frac{\hat{\boldsymbol{p}}^2}{2M},$$

that can often be approximated as the standard kinetic energy as is done in the above equation. This approximation can be justified as follows. The spin-orbit coupling terms are responsible for the Landau-Zener losses in adiabatic potentials. As usually the experiments are done in a regime where these losses are small, one can guess that all spin-orbit coupling terms including the ones acting as pure gauge fields without inducing losses must be small.

B.2 Approximate analytic solution

The infinite system of equations (B.8) can be formally solved using operator algebra, assuming that (as is often the case) the $n = 0$ manifold plays a special role. Let $\hat{\mathcal{P}}$ be the projector on the $n = 0$ manifold and $\hat{\mathcal{Q}} = \hat{\mathcal{I}} - \hat{\mathcal{P}}$ its complementary. Collecting all the $|\psi_n\rangle$ in a single column vector $|\Psi\rangle$, the infinite system of equations (B.8) can be written $E\,|\Psi\rangle = \hat{\mathcal{H}}\,|\Psi\rangle$ and formally [Cohen-Tannoudji *et al.*, 1998]:

$$\begin{aligned} E\hat{\mathcal{P}}\,|\Psi\rangle &= \hat{\mathcal{P}}\hat{\mathcal{H}}\hat{\mathcal{P}}\,|\Psi\rangle + \hat{\mathcal{P}}\hat{\mathcal{H}}\hat{\mathcal{Q}}\,|\Psi\rangle\,, \\ E\hat{\mathcal{Q}}\,|\Psi\rangle &= \hat{\mathcal{Q}}\hat{\mathcal{H}}\hat{\mathcal{P}}\,|\Psi\rangle + \hat{\mathcal{Q}}\hat{\mathcal{H}}\hat{\mathcal{Q}}\,|\Psi\rangle\,. \end{aligned}$$

For an energy E not in the kernel of $\hat{\mathcal{Q}}\hat{\mathcal{H}}\hat{\mathcal{Q}}$ the second equation is equivalent to:

$$\hat{\mathcal{Q}}\,|\Psi\rangle = \frac{\hat{\mathcal{Q}}}{E\hat{\mathcal{Q}} - \hat{\mathcal{Q}}\hat{\mathcal{H}}\hat{\mathcal{Q}}}\hat{\mathcal{H}}\hat{\mathcal{P}}\,|\Psi\rangle\,,$$

where the operator fraction notation is a shortcoming for operator inversion. This results in an exact implicit self-consistent equation for E:

$$E\hat{\mathcal{P}}\,|\Psi\rangle = \hat{\mathcal{P}}\hat{\mathcal{H}}\hat{\mathcal{P}}\,|\Psi\rangle + \hat{\mathcal{P}}\hat{\mathcal{H}}\frac{\hat{\mathcal{Q}}}{E\hat{\mathcal{Q}} - \hat{\mathcal{Q}}\hat{\mathcal{H}}\hat{\mathcal{Q}}}\hat{\mathcal{H}}\hat{\mathcal{P}}\,|\Psi\rangle\,.$$

This last equation may be used to build a systematic perturbative expansion to find E.

Indeed, including only the first order correction results in:

$$E\left|\psi_0\right\rangle = \left(\hat{D}_0 + \sum_{n\neq 0}(\hat{K}_n + \hat{V}_n)\frac{\hat{I}}{E\hat{I} - \hat{D}_n}(\hat{K}_n^\dagger + \hat{V}_n^\dagger)\right)\left|\psi_0\right\rangle,$$

where I used the fact that $\hat{K}_{-n} = \hat{K}_n^\dagger$ and $\hat{V}_{-n} = \hat{V}_n^\dagger$. Recalling that $\hat{D}_n = n\hbar\omega\hat{I} + \hat{D}_0$ and using the formal operator expansion:

$$\frac{\hat{I}}{E\hat{I} - \hat{D}_n} = -\frac{1}{n\hbar\omega}\sum_{k=0}^{\infty}\left(\frac{E\hat{I} - \hat{D}_0}{n\hbar\omega}\right)^k,$$

I obtain the leading order (in $1/\omega$) correction to the eigenvalue equation:

$$E\left|\psi_0\right\rangle = \left(\hat{D}_0 - \sum_{n\neq 0}\frac{(\hat{K}_n + \hat{V}_n)(\hat{K}_n^\dagger + \hat{V}_n^\dagger)}{n\hbar\omega}\right)\left|\psi_0\right\rangle.$$

Assuming, as explained above, that the spin orbit coupling terms are negligible, this last equation can be written, restoring explicitly the spatial dependence of the operators:

$$E\left|\psi_0\right\rangle = \left(\frac{\hat{\boldsymbol{p}}^2}{2M} - \delta(\boldsymbol{r})\hat{F}_z + \hat{V}_0(\boldsymbol{r}) + \sum_{n>0}\frac{\left[\hat{V}_n(\boldsymbol{r})^\dagger, \hat{V}_n(\boldsymbol{r})\right]}{n\hbar\omega}\right)\left|\psi_0\right\rangle,$$

where the last term involves the commutator between $\hat{V}_n(\boldsymbol{r})^\dagger$ and $\hat{V}_n(\boldsymbol{r})$. Due to the form of the coupling terms, this commutator is necessarily proportional to $\hat{F}_z$, such that I may write:

$$\sum_{n>0}\frac{\left[\hat{V}_n(\boldsymbol{r})^\dagger, \hat{V}_n(\boldsymbol{r})\right]}{n\hbar\omega} = \Sigma(\boldsymbol{r})\hat{F}_z,$$

and the effective equation for the $n = 0$ manifold reads:

$$E\left|\psi_0\right\rangle = \left(\frac{\hat{\boldsymbol{p}}^2}{2M} - \left[\delta(\boldsymbol{r}) - \Sigma(\boldsymbol{r})\right]\hat{F}_z + \hat{V}_0(\boldsymbol{r})\right)\left|\psi_0\right\rangle. \tag{B.13}$$

Therefore the main effects of the beyond RWA terms are a renormalization of the coupling strength, due to the coefficients $c_k(\boldsymbol{r})$ in the definition of $\hat{V}_0(\boldsymbol{r})$ and a shift of the resonance due to the off-resonant corrections contributing to the coefficient $\Sigma(\boldsymbol{r})$. The usual RWA expression is recovered by considering the limit $\Sigma(\boldsymbol{r}) = 0$, $c_0(\boldsymbol{r}) = 1$ and $c_k(\boldsymbol{r}) = 0$ for $k \neq 0$.

B.3 An example: the dressed quadrupole trap

I consider now a quadrupole trap with a z symmetry axis for which the static magnetic field is:

$$\boldsymbol{B}_0(\boldsymbol{r}) = b'(x\boldsymbol{e}_x + y\boldsymbol{e}_y - 2z\boldsymbol{e}_z),$$

where b' is the horizontal gradient. The Larmor frequency then takes a very simple form: $\omega_0(\boldsymbol{r}) = \alpha\ell$ where $\alpha = \mu_B g_F b'/\hbar$ is the horizontal gradient in frequency units and $\ell^2 = \rho^2 + 4z^2$, with (ρ, ϕ, z) the standard cylindrical coordinates.

In order to obtain simple expressions I focus on atoms in a $F = 1$ groundstate as in [Guo *et al.*, 2020], for which the spin rotation (B.4) reads:

$$\hat{U}_0 = \begin{pmatrix} -\frac{1}{2}+\frac{z}{\ell} & -\frac{\rho}{\sqrt{2}\ell}e^{-i\phi} & -\frac{\ell+2z}{2\ell}e^{-2i\phi} \\ -\frac{\rho}{\sqrt{2}\ell}e^{i\phi} & -\frac{2z}{\ell} & \frac{\rho}{\sqrt{2}\ell}e^{-i\phi} \\ -\frac{\ell+2z}{2\ell}e^{2i\phi} & \frac{\rho}{\sqrt{2}\ell}e^{i\phi} & -\frac{1}{2}+\frac{z}{\ell} \end{pmatrix}.$$

The spin orbit coupling then writes:

$$\hat{\boldsymbol{A}}_0(\boldsymbol{r}) = -i\left(\hat{F}_+e^{-i\phi} - \hat{F}_-e^{i\phi}\right)\frac{z\boldsymbol{e}_\rho - \rho\boldsymbol{e}_z}{\ell^2} + \left(-\hat{F}_z\frac{\ell+2z}{\ell\rho} + \frac{\hat{F}_+e^{-i\phi}+\hat{F}_-e^{i\phi}}{2\ell}\right)\boldsymbol{e}_\phi.$$

In the absence of the rf field trapped atoms follow adiabatically the $|+1\rangle$ eigenstate of $\hat{F}_z$ and I may write: $|\psi\rangle = \psi(\boldsymbol{r})\,|+1\rangle$, such that I obtain an effective equation for $\psi(\boldsymbol{r})$, by projecting on $|+1\rangle$:

$$i\hbar\frac{\partial\psi(\boldsymbol{r})}{\partial t} = \left[\frac{\hat{\boldsymbol{p}}^2}{2M} + \omega_0(\boldsymbol{r}) + \frac{\langle +1|\,\hat{\boldsymbol{A}}_0(\boldsymbol{r})^2\,|+1\rangle}{2M}\right]\psi(\boldsymbol{r}) - i\frac{\ell+2z}{\ell}\frac{\hbar^2}{M\rho^2}\frac{\partial\psi(\boldsymbol{r})}{\partial\phi},$$

where I used the fact that $\hat{\boldsymbol{p}}$ commutes with $\langle +1|\,\hat{\boldsymbol{A}}_0(\boldsymbol{r})\,|+1\rangle$. The last term may favor energetically states with finite angular momentum but the effect is very small [Corman, 2016]. Similarly the correction to the Larmor frequency is small. By evaluating the spin-flip terms one can estimate the lifetime of the trapped state. I note that all the spin orbit coupling terms are of the order of $\hbar^2/(M\ell^2)$ and therefore to obtain energy shifts of $\sim$ kHz one must have $\ell < 1\,\mu\text{m}$. In this situation losses are dominant, at least in the experiments.

Considering now a general homogeneous rf dressing field:

$$\boldsymbol{B}(\boldsymbol{r},t) = B_x(t)\boldsymbol{e}_x + B_y(t)\boldsymbol{e}_y + B_z(t)\boldsymbol{e}_z,$$

for which the couplings read:

$$\begin{aligned} \Omega_\pm(\boldsymbol{r},t) &= \frac{\mu_B g_F}{2\hbar}e^{\mp i\phi}\left[B_z(t)\frac{\rho}{\ell} \mp i(B_x(t)\sin[\phi] - B_y(t)\cos[\phi])\right. \\ &\quad \left. + \frac{2z}{\ell}(B_x(t)\cos[\phi] + B_y(t)\sin[\phi])\right], \\ \Omega_z(\boldsymbol{r},t) &= \frac{\mu_B g_F}{\hbar}\frac{(B_x(t)\cos[\phi] + B_y(t)\sin[\phi])\rho - 2B_z(t)z}{\ell}. \end{aligned}$$

These general expressions can be used for an arbitrary polarization.

For the sake of simplicity I focus now on a purely circular polarization: $B_x(t) = B_{\text{rf}}\cos[\omega t]$, $B_y(t) = B_{\text{rf}}\sin[\omega t]$ and $B_z(t) = 0$, resulting in:

$$\begin{aligned} \Omega_\pm(\boldsymbol{r},t) &= \frac{\Omega_0}{2}e^{\mp i\phi}\frac{2z\cos[\omega t - \phi] \pm i\sin[\omega t - \phi]\,\ell}{\ell}, \\ \Omega_z(\boldsymbol{r},t) &= \Omega_0\frac{\rho}{\ell}\cos[\omega t - \phi], \end{aligned}$$

where I introduced the typical coupling strength $\Omega_0 = \mu_B g_F B_{\text{rf}}/\hbar$.

I may now compute:

$$f(\boldsymbol{r},t) = \frac{\rho}{\ell}\frac{\Omega_0}{\omega}\sin[\omega t - \phi]$$

and using the Jacobi-Anger expansion ($e^{iz\sin[\theta]} = \sum_n J_n[z]e^{in\theta}$):

$$e^{if(\boldsymbol{r},t)} = \sum_n J_n\left[\frac{\Omega_0}{\omega}\frac{\rho}{\ell}\right]e^{in(\omega t-\phi)},$$

where $J_n[x]$ is the n-th Bessel function of the first kind, and therefore $c_n = J_n[\Omega_0\rho/(\omega\ell)]e^{-in\phi} \equiv j_n e^{-in\phi}$.

The only non vanishing harmonics are:

$$\begin{aligned}\tilde{\Omega}_\pm^{(+1)}(\boldsymbol{r}) &= \Omega_0\frac{2z-\ell}{4\ell},\\ \tilde{\Omega}_\pm^{(-1)}(\boldsymbol{r}) &= \Omega_0\frac{2z+\ell}{4\ell}e^{\mp 2i\phi}.\end{aligned}$$

Finally the atom–field couplings are:

$$\hat{V}_k(\boldsymbol{r}) = e^{ik\phi}\left[-\Omega_+(\boldsymbol{r})j_k\frac{(-1)^k\hat{F}_+ + \hat{F}_-}{2} + \Omega_-(\boldsymbol{r})\frac{(-1)^k j_{k+2}\hat{F}_+ + j_{k-2}\hat{F}_-}{2}\right],$$

where I introduced $\Omega_\pm(\boldsymbol{r}) = \Omega_0/2\times(1\mp 2z/\ell)$. For reference, the rf dressed spin orbit term is:

$$\begin{aligned}\hat{\boldsymbol{A}}_1(\boldsymbol{r},t) &= \left[4\hat{F}_z\frac{z^2}{\ell^3}\frac{\Omega_0}{\omega}\sin[\omega t-\phi] - i\frac{z}{\ell^2}\left(\hat{F}_+e^{i(\omega t-\phi+f)} - \hat{F}_-e^{-i(\omega t-\phi+f)}\right)\right]\boldsymbol{e}_\rho\\ &+\left[-\left(\frac{\ell+2z}{\ell\rho}+\frac{\Omega_0}{\omega\ell}\cos[\omega t-\phi]\right)\hat{F}_z + \frac{\hat{F}_+e^{i(\omega t-\phi+f)} + \hat{F}_-e^{-i(\omega t-\phi+f)}}{2\ell}\right]\boldsymbol{e}_\phi\\ &+\left[-4\hat{F}_z\frac{z\rho\Omega_0}{\ell^3\omega}\sin[\omega t-\phi] + i\frac{\rho}{\ell^2}\left(\hat{F}_+e^{i(\omega t-\phi+f)} - \hat{F}_-e^{-i(\omega t-\phi+f)}\right)\right]\boldsymbol{e}_z.\end{aligned}$$

These expressions are useful to derive analytical formulas or to perform numerical computations. As mentioned above $\hat{\boldsymbol{A}}_1(\boldsymbol{r},t)$ is of order $\hbar/\ell$, which corresponds to a very small term. For example, with a length $\ell\sim 30\,\mu\text{m}$ it gives a small velocity of 0.02 mm/s.

The approximate solution then reads:

$$E\left|\psi_0\right\rangle = \left(\frac{\hat{\boldsymbol{p}}^2}{2M} - [\delta(\boldsymbol{r})-\Sigma(\boldsymbol{r})]\hat{F}_z - [j_0\Omega_+(\boldsymbol{r}) - j_2\Omega_-(\boldsymbol{r})]\hat{F}_x\right)\left|\psi_0\right\rangle,$$

where at leading order:

$$\begin{aligned}\Sigma(\boldsymbol{r}) &= \sum_{n>0}(j_{n-2}-j_{n+2})\Omega_-(\boldsymbol{r})\frac{(j_{n-2}+j_{n+2})\Omega_-(\boldsymbol{r}) - 2j_n\Omega_+(\boldsymbol{r})}{2n\omega}\\ &\simeq j_0\Omega_-(\boldsymbol{r})\frac{j_0\Omega_-(\boldsymbol{r}) - 2j_2\Omega_+(\boldsymbol{r})}{4\omega}.\end{aligned}$$

A straightforward identification of the terms lead to the expression of equation (B.1).

Finally the effective Hamiltonian can be diagonalized by a spin rotation:

$$U_1 = \exp\left[i\beta(\boldsymbol{r})\frac{\hat{F}_y}{\hbar}\right],$$

where the angle $\beta(\boldsymbol{r})$ is given by:

$$\sin[\beta(\boldsymbol{r})] = \frac{\tilde{\Omega}(\boldsymbol{r})}{\sqrt{(\delta(\boldsymbol{r}) - \Sigma(\boldsymbol{r}))^2 + \tilde{\Omega}(\boldsymbol{r})^2}} \text{ and } \cos[\beta(\boldsymbol{r})] = \frac{\Sigma(\boldsymbol{r}) - \delta(\boldsymbol{r})}{\sqrt{(\delta(\boldsymbol{r}) - \Sigma(\boldsymbol{r}))^2 + \tilde{\Omega}(\boldsymbol{r})^2}}.$$

This position dependent spin rotation gives again a spin-orbit coupling term, that can be used to evaluate the Landau-Zener losses using a Fermi golden rule approach, and the final effective Hamiltonian reads:

$$\hat{H} = \frac{\left[\hat{\boldsymbol{p}} + \boldsymbol{\nabla}\beta(\boldsymbol{r})\hat{F}_y\right]^2}{2M} + \sqrt{(\delta(\boldsymbol{r}) - \Sigma(\boldsymbol{r}))^2 + \tilde{\Omega}(\boldsymbol{r})^2}\hat{F}_z,$$

where, for reference,

$$\boldsymbol{\nabla}\beta(\boldsymbol{r}) = \frac{\tilde{\Omega}(\boldsymbol{r})\boldsymbol{\nabla}(\delta(\boldsymbol{r}) - \Sigma(\boldsymbol{r})) - (\delta(\boldsymbol{r}) - \Sigma(\boldsymbol{r}))\boldsymbol{\nabla}\tilde{\Omega}(\boldsymbol{r})}{(\delta(\boldsymbol{r}) - \Sigma(\boldsymbol{r}))^2 + \tilde{\Omega}(\boldsymbol{r})^2}.$$

With the new total potential in the $|+1\rangle$ dressed state:

$$V(\boldsymbol{r}) = \hbar\sqrt{(\delta(\boldsymbol{r}) - \Sigma(\boldsymbol{r}))^2 + \tilde{\Omega}(\boldsymbol{r})^2} + Mgz,$$

the equilibrium position and vertical oscillation frequency are the same than the ones obtained with the RWA formula. However the radial oscillation frequency is modified:

$$\omega_r = \sqrt{\frac{g}{4R}}\left(1 - \frac{\hbar\Omega_0}{2MgR}\sqrt{1-\epsilon^2}\left(1 + \frac{\Omega_0^2}{\omega_{\mathrm{rf}}^2}\right)\right)^{1/2}.$$

The extra $\Omega_0^2/\omega_{\mathrm{rf}}^2$ term lowers the oscillation frequency, and the criterion for gravity compensation $\omega_r = 0$ gives:

$$\hbar\Omega_0 = \frac{Mg}{1 + \frac{\Omega_0^2}{\omega_{\mathrm{rf}}^2}} \frac{2R}{\sqrt{1-\epsilon^2}}. \tag{B.14}$$

With the parameters of section 2.4.2, this last equation predicts that the gravity compensation occurs at $\alpha/(2\pi) = 7.35\,\mathrm{kHz/\mu m}$ in fair agreement with the observations. Equation (B.14) was obtained after the publication of the results [Guo *et al.*, 2022] and is not given in the paper.

B.4 Map to spheroidal coordinates

For the quadrupole trap configuration, dressed by a circularly polarized rf field, the potential depends only on the spatial coordinates through ℓ, ρ/ℓ (for Ω_π) and $2z/\ell$ (for $\Omega_\pm$). Therefore it is interesting to map the cylindrical coordinates (ρ, z, ϕ) to spheroidal coordinates (ℓ, χ, ϕ) where the angle χ is defined through: $\sin[\chi] = \rho/\ell$ and $\cos[\chi] = 2z/\ell$.

The total potential reads, in the improved analytical expression and including gravity:

$$V(\ell, \chi) = \hbar\sqrt{(\omega_{\mathrm{rf}} - \alpha\ell - \Sigma(\chi))^2 + \tilde{\Omega}(\chi)^2} + \frac{Mg\ell}{2}\cos[\chi],$$

where both the shift Σ and the renormalized coupling $\tilde{\Omega}$ depend only on χ. The equilibrium surface, defined as $\frac{\partial V(\ell,\chi)}{\partial \ell} = 0$, is:

$$\ell_{\mathrm{eq}}(\chi) = r_0 \left(1 - \frac{\Sigma(\chi)}{\omega_{\mathrm{rf}}} - \frac{|\tilde{\Omega}(\chi)|}{\omega_{\mathrm{rf}}} \frac{\epsilon \cos[\chi]}{\sqrt{1-\epsilon^2 \cos[\chi]^2}} \right).$$

A lengthy but straightforward computation gives the Laplacian in this coordinate system:

$$\begin{aligned} \Delta \ = \ & \frac{7-3\cos[2\chi]}{2\ell}\frac{\partial}{\partial \ell} - 3\frac{\sin[2\chi]}{\ell}\frac{\partial^2}{\partial \ell \partial \chi} + \frac{5+3\cos[2\chi]}{2}\frac{\partial^2}{\partial \ell^2} \\ & + \frac{\cot[\chi]+3\sin[2\chi]}{\ell^2}\frac{\partial}{\partial \chi} + \frac{5-3\cos[2\chi]}{2\ell^2}\frac{\partial^2}{\partial \chi^2} + \frac{1}{\ell^2 \sin[\chi]^2}\frac{\partial^2}{\partial \phi^2}. \end{aligned}$$

Obviously the change of coordinates simplifies the computation of the potential but increase the difficulty of computing the Laplacian. In particular it is not compatible anymore with a spectral scheme. Therefore, in order to compute the mean field groundstate, it is necessary to introduce a finite difference scheme, using a rectangular grid of $N_\ell \times N_\chi$ elements in the domain $[r_0 - \Delta\ell/2, r_0 + \Delta\ell/2] \times [0,\pi]$, with $\Delta\ell < 2r_0$, and implement discrete differential operators acting on $\psi_{n,m} \equiv \psi(r_0 - \Delta\ell/2 + n\delta\ell, \delta\chi/2 + m\delta\chi)$, with $n \in [0, N_\ell - 1]$, $m \in [0, N_\chi - 1]$, $\delta\ell = \Delta\ell/(N_\ell - 1)$ and $\delta\chi = \pi/N_\chi$. The grid for the coordinate χ is shifted by $\delta\chi/2$ to avoid the singularities of Δ at $\chi = 0$ and π. For the inner points, the discrete derivatives can be evaluated as:

$$\begin{aligned} \left.\frac{\partial \psi}{\partial \ell}\right|_{n,m} &= \frac{\psi_{n+1,m} - \psi_{n-1,m}}{2\delta\ell}, \\ \left.\frac{\partial \psi}{\partial \chi}\right|_{n,m} &= \frac{\psi_{n,m+1} - \psi_{n,m-1}}{2\delta\chi}, \\ \left.\frac{\partial^2 \psi}{\partial \ell^2}\right|_{n,m} &= \frac{\psi_{n+1,m} - 2\psi_{n,m} + \psi_{n-1,m}}{\delta\ell^2}, \\ \left.\frac{\partial^2 \psi}{\partial \chi^2}\right|_{n,m} &= \frac{\psi_{n,m+1} - 2\psi_{n,m} + \psi_{n,m-1}}{\delta\chi^2}. \end{aligned}$$

At the edges of the domain these formulas must be adapted to take into account the boundary conditions. Assuming that the states are localized around $\ell \simeq r_0$ it is safe to assume that the wavefunction vanishes at the ℓ boundaries, provided that $\Delta\ell$ is large enough, i.e. $\psi_{-1,m} = \psi_{N_\ell,m} = 0$. For the χ variable we may use $\psi_{n,-1} = \psi_{n,0}$ and $\psi_{n,N_\ell} = \psi_{n,N_\ell-1}$ thanks to the rotational invariance on ϕ. These relations enable the representation of the Laplacian as a penta-diagonal sparse matrix, that can be efficiently implemented in a computer program.

Figure B.2 shows the result of the groundstate computation using the (ℓ, χ, ϕ) coordinate system (assuming rotational invariance on ϕ), for parameters corresponding to the last column of Figure 2.6. It uses the second order Floquet expansion, that is accurate in this situation. The imaginary time propagation converges to a chemical potential of $\mu/(2\pi) = h \times 580\,\mathrm{Hz}$. It is interesting to notice that the equipotential lines are open and that a Thomas-Fermi approximation would predict that the density profile would extend up to the north pole ($\chi \to 0$). As mentioned in chapter 2 the density profile is constrained by the inhomogeneous transverse trapping frequency.

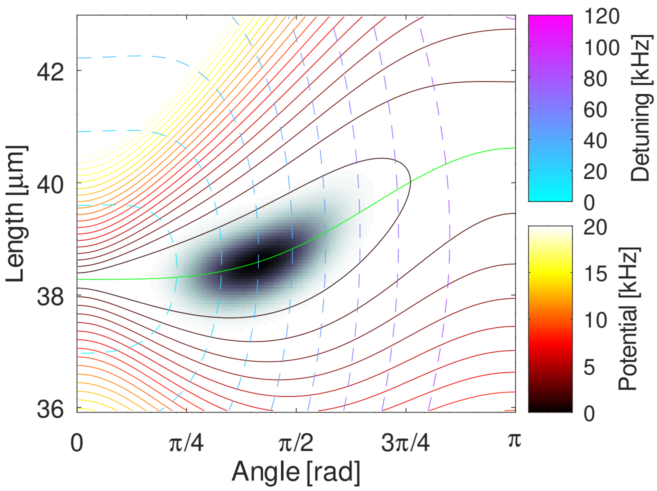

Figure B.2: Mean field groundstate density (grey shadow) in the (χ, ℓ) coordinates, for $N = 10^5$ atoms in a dressed quadrupole trap, with $\alpha/(2\pi) = 7.68\,\mathrm{kHz/\mu m}$, $\omega_{\mathrm{rf}}/(2\pi) = 300\,\mathrm{kHz}$ and $\Omega_0/(2\pi) = 85\,\mathrm{kHz}$. The green solid line is the minimum energy surface. The dashed lines give the effective detuning between dressed states (spaced by 10 kHz) and the solid lines give the equipotential lines (spaced by $h \times 1\,\mathrm{kHz}$).

Appendix C

Rotating harmonic trap

In this appendix I recall the formulas describing the thermodynamics of a harmonic trap in a rotating frame [Fetter, 2009], with an effective trapping potential:

$$V_{\text{eff}}(\boldsymbol{r}) = \frac{M\omega_r^2}{2}\rho^2\left(1 - \frac{\Omega^2}{\omega_r^2}\right) + \frac{M\omega_z^2}{2}z^2,$$

accounting for the centrifugal term. The trap has a well defined minimum for $|\Omega| < \omega_r$.

Following the approach of [Gifford and Baym, 2008], I first consider the three-dimensional Thomas-Fermi limit, at zero termperature, for which density profile is given by:

$$n_{\text{BEC}}(\boldsymbol{r}) = \frac{\mu}{g_{3D}}\left(1 - \frac{\rho^2}{R^2} - \frac{z^2}{R_z^2}\right),$$

and such that $n_{\text{BEC}}(\boldsymbol{r}) \geq 0$, with Thomas-Fermi radii $R = \sqrt{2\mu/(M(\omega_r^2 - \Omega^2))}$ and $R_z = \sqrt{2\mu/(M\omega_z^2)}$. The chemical potential obtained from the normalization of the density profile is:

$$\mu = \frac{\hbar\bar{\omega}}{2}\left(15N_0\frac{a_s}{\bar{a}}\left(1 - \frac{\Omega^2}{\omega_r^2}\right)\right)^{2/5},$$

where $\bar{\omega} = (\omega_r^2\omega_z)^{1/3}$ is the average trapping frequency (without rotation) and $\bar{a} = \sqrt{\hbar/(M\bar{\omega})}$ is the associated characteristic length.

This description can be extended to finite temperatures, in the regime where one can neglect the inter-atomic interactions, except to determine the groundstate density profile. The condensate atom number N_0 can be related to the total atom number N using the ideal Bose gas in a harmonic trap result: $N_0/N = 1 - (T/T_c)^3$, where the critical temperature is $k_BT_c = \hbar\bar{\omega}(N/\zeta(3))^{1/3} \times (1 - (\Omega/\omega_r)^2)^{1/3}$, taking into account the effect of rotation, with $\zeta(3) \simeq 1.202$. The effective two-dimensional superfluid density is then obtained as:

$$n_s(\rho) = \int dz\, n_{\text{BEC}}(\boldsymbol{r}) = \frac{4}{3}\frac{R_z\mu}{g_{3D}}\left(1 - \frac{\rho^2}{R^2}\right)^{3/2} = \frac{\sqrt{2}}{3\pi a_z a_s}\left(\frac{\mu}{\hbar\omega_z}\right)^{3/2}\left(1 - \frac{\rho^2}{R^2}\right)^{3/2},$$

where a_s is the s-wave scattering length fixing the interaction strength: $g_{3D} = 4\pi\hbar^2 a_s/M$. The peak two-dimensional superfluid phase-space density $\mathcal{D}_s = n_s(\rho = 0)\Lambda^2$ is then:

$$\mathcal{D}_s \simeq 1.7996 \times \left[\frac{\bar{a}}{a_s}\right]^{2/5}\left[\frac{\omega_r}{\omega_z}\right]^{2/3} N^{4/15}\frac{T_c}{T}\left[1 - \frac{T^3}{T_c^3}\right]^{3/5}\left[1 - \frac{\Omega^2}{\omega_r^2}\right]^{4/15}. \tag{C.1}$$

According to the criterion discussed in section 3.2.3, an upper bound on the melting temperature can be estimated by solving $\mathcal{D}_s(T_m) \simeq 87$. Equation (C.1) shows that $\mathcal{D}_s$ is a decreasing function of both T/T_c and Ω/ω_r, as a consequence T_m/T_c decreases when Ω/ω_r increases. Furthermore, T_m/T_c decreases when ω_z increases, making it easier to observe the melting transition in a oblate trap.

It is interesting to consider the two-dimensional limit $\omega_z \gg \omega_r$, neglecting the subtleties of the Kosterlitz-Thouless transition. In that case we may identify the two-dimensional superfluid and condensate densities:

$$n_s(\rho) = \frac{\mu}{g_{2D}}\left(1 - \frac{\rho^2}{R^2}\right),$$

where $g_{2D} = (\hbar^2/M) \times \sqrt{8\pi} a_s/a_z$ is the effective two-dimensional interaction strength. Using the normalization of the density to the condensate atom number I obtain the chemical potential:

$$\mu = \hbar\omega_r \left(\sqrt{\frac{8}{\pi}}\frac{a_s}{a_z} N_0 \left(1 - \frac{\Omega^2}{\omega_r^2}\right)\right)^{1/2}.$$

Similarly to the three-dimensional case, we can use the ideal Bose gas result to obtain an estimate of the finite temperature chemical potential, using the relation $N_0/N = 1 - (T/T_c)^2$, where the two-dimensional critical temperature is $k_B T_c = \hbar\omega_r(6N(1 - (\Omega/\omega_r)^2))^{1/2}/\pi$. The resulting peak two-dimensional phase-space density is then:

$$\mathcal{D}_s \simeq 2.03 \frac{T_c}{T}\left(\frac{a_z}{a_s}\left(1 - \frac{T^2}{T_c^2}\right)\right)^{1/2}.$$

With that model, the melting temperature T_m depends on the rotation rate Ω/ω_r only through T_c.

Finally one can use an estimation based on the Kosterlitz-Thouless equation of state, for the total phase-space density $\mathcal{D}(\mu/(k_B T))$ and the superfluid phase-space density $\mathcal{D}_s(\mu/(k_B T))$, where both quantities depend on the dimensionless interaction strength $\tilde{g}$. Within the local density approximation, the total atom number is given by:

$$N = \left(\frac{k_B T}{\hbar\omega_r}\right)^2 \left(1 - \frac{\Omega^2}{\omega_r^2}\right)^{-1} \int_{\infty}^{\frac{\mu}{k_B T}} du\, \mathcal{D}(u),$$

and the critical temperature T_c is defined by:

$$N = \left(\frac{k_B T_c}{\hbar\omega_r}\right)^2 \left(1 - \frac{\Omega^2}{\omega_r^2}\right)^{-1} \int_{\infty}^{\frac{\mu_c}{k_B T_c}} du\, \mathcal{D}(u),$$

where $\mu_c/(k_B T_c)$ is given in equation (2.1). Comparing the last two equations allows to write an implicit equation for

$$\frac{T}{T_c} = \left[\frac{\int_{-\infty}^{\frac{\mu_c}{k_B T_c}} du\, \mathcal{D}(u)}{\int_{-\infty}^{\frac{\mu}{k_B T}} du\, \mathcal{D}(u)}\right]^{1/2}.$$

Similarly, the peak superfluid fraction depends only on $\mu/(k_B T)$, i.e. $\mathcal{D}_s(\mu/(k_B T))$, and can be thus written has a function of T/T_c. Solving $\mathcal{D}_s \simeq 87$ thus gives the upper bound for the melting temperature. Here, similarly to the two-dimensional BEC estimate, the rotation rate enters only through the definition of the critical temperature.

Bibliography

[1] M. J. Ablowitz, and H. Segur (1981), *Solitons and the Inverse Scattering Transform*, Vol. 127 (Society for Industrial and Applied Mathematics).

[2] J. R. Abo-Shaeer, C. Raman, J. M. Vogels, and W. Ketterle (2001), "Observation of vortex lattices in Bose-Einstein condensates," Science **292** (5516), 476–479.

[3] K. Aikawa, A. Frisch, M. Mark, S. Baier, R. Grimm, and F. Ferlaino (2014), "Reaching Fermi degeneracy via universal dipolar scattering," Physical Review Letters **112**, 010404.

[4] K. Aikawa, A. Frisch, M. Mark, S. Baier, A. Rietzler, R. Grimm, and F. Ferlaino (2012), "Bose-Einstein condensation of Erbium," Physical Review Letters **108** (21), 210401.

[5] L. Amico, G. Birkl, M. Boshier, and L.-C. Kwek (2017), "Focus on atomtronics-enabled quantum technologies," New Journal of Physics **19** (2), 020201.

[6] M. H. Anderson, J. R. Ensher, M. R. Matthews, C. E. Wieman, and E. A. Cornell (1995), "Observation of Bose-Einstein condensation in a dilute atomic vapor," Science **269** (5221), 198–201.

[7] J. R. Anglin (2001), "Local vortex generation and the surface mode spectrum of large Bose-Einstein condensates," Physical Review Letters **87** (24), 240401.

[8] W. S. Bakr, J. I. Gillen, A. Peng, S. Fölling, and M. Greiner (2009), "A quantum gas microscope for detecting single atoms in a Hubbard-regime optical lattice," Nature **462** (7269), 74–77.

[9] A. J. Barker, S. Sunami, D. Garrick, A. Beregi, K. Luksch, E. Bentine, and C. J. Foot (2020), "Realising a species-selective double well with multiple-radiofrequency-dressed potentials," Journal of Physics B: Atomic, Molecular and Optical Physics **53** (15), 10.1088/1361-6455/ab9152.

[10] S. Beattie, S. Moulder, R. J. Fletcher, and Z. Hadzibabic (2013), "Persistent currents in spinor condensates," Physical Review Letters **110** (2), 025301.

[11] E. Bentine, A. J. Barker, K. Luksch, S. Sunami, T. L. Harte, B. Yuen, C. J. Foot, D. J. Owens, and J. M. Hutson (2020), "Inelastic collisions in radiofrequency-dressed mixtures of ultracold atoms," Physical Review Research **2** (3), 33163.

[12] E. Bentine, T. L. Harte, K. Luksch, A. J. Barker, J. Mur-Petit, B. Yuen, and C. J. Foot (2017), "Species-selective confinement of atoms dressed with multiple radiofrequencies," Journal of Physics B: Atomic, Molecular and Optical Physics **50** (9), 094002.

[13] B. Bertini, M. Collura, J. De Nardis, and M. Fagotti (2016), "Transport in out-of-equilibrium XXZ chains: Exact profiles of charges and currents," Physical Review Letters **117**, 207201.

[14] D. J. Bishop, and J. D. Reppy (1978), "Study of the superfluid transition in two-dimensional ^{4}He films," Physical Review Letters **40**, 1727–1730.

[15] P. B. Blakie (2008), "Numerical method for evolving the projected Gross-Pitaevskii equation," Physical Review E **78** (2), 026704.

[16] I. Bloch, J. Dalibard, and S. Nascimbène (2012), "Quantum simulations with ultracold quantum gases," Nature Physics **8** (4), 267–276.

[17] I. Bloch, J. Dalibard, and W. Zwerger (2008), "Many-body physics with ultracold gases," Reviews of Modern Physics **80** (3), 885–964.

[18] I. Bouchoule, and J. Dubail (2022), "Generalized hydrodynamics in the one-dimensional Bose gas: theory and experiments," Journal of Statistical Mechanics: Theory and Experiment **2022** (1), 014003.

[19] C. C. Bradley, C. A. Sackett, J. J. Tollett, and R. G. Hulet (1995), "Evidence of Bose-Einstein condensation in an atomic gas with attractive interactions," Physical Review Letters **75** (9), 1687–1690.

[20] V. Bretin, S. Stock, Y. Seurin, and J. Dalibard (2004), "Fast rotation of a Bose-Einstein condensate." Physical review letters **92** (5), 050403.

[21] K. A. Burrows, H. Perrin, and B. M. Garraway (2017), "Nonadiabatic losses from radio-frequency-dressed cold-atom traps: Beyond the Landau-Zener model," Physical Review A **96**, 023429.

[22] Y. Cai, D. G. Allman, P. Sabharwal, and K. C. Wright (2022), "Persistent currents in rings of ultracold fermionic atoms," Physical Review Letters **128** (15), 150401.

[23] L. D. Carr, C. W. Clark, and W. P. Reinhardt (2000), "Stationary solutions of the one-dimensional nonlinear Schrödinger equation. I. Case of repulsive nonlinearity," Physical Review A **62**, 063610.

[24] D. Cassettari, B. Hessmo, R. Folman, T. Maier, and J. Schmiedmayer (2000), "Beam splitter for guided atoms," Physical Review Letters **85** (26), 5483–5487.

[25] Y. Castin (2001), "Bose-Einstein condensates in atomic gases: Simple theoretical results," in *Coherent atomic matter waves* (Springer Berlin Heidelberg, Berlin, Heidelberg) pp. 1–136.

[26] Y. Castin (2004), "Simple theoretical tools for low dimension Bose gases," Journal de Physique IV (Proceedings) **116**, 89–132.

[27] Y. Castin, and R. Dum (1996), "Bose-Einstein condensates in time dependent traps," Physical Review Letters **77** (27), 5315–5319.

[28] O. A. Castro-Alvaredo, B. Doyon, and T. Yoshimura (2016), "Emergent hydrodynamics in integrable quantum systems out of equilibrium," Physical Review X **6**, 041065.

[29] F. Chevy, and S. Stringari (2003), "Kelvin modes of a fast rotating Bose-Einstein condensate," Physical Review A **68** (5), 053601.

[30] C. Chin, R. Grimm, P. Julienne, and E. Tiesinga (2010), "Feshbach resonances in ultracold gases," Reviews of Modern Physics **82** (2), 1225–1286.

[31] S.-W. Chiow, T. Kovachy, H.-C. Chien, and M. A. Kasevich (2011), "$102\hbar k$ large area atom interferometers," Physical Review Letters **107** (13), 130403.

[32] L. Chomaz, L. Corman, T. Bienaimé, R. Desbuquois, C. Weitenberg, S. Nascimbène, J. Beugnon, and J. Dalibard (2015), "Emergence of coherence via transverse condensation in a uniform quasi-two-dimensional Bose gas," Nature Communications **6**, 6162.

[33] I. Coddington, P. Engels, V. Schweikhard, and E. A. Cornell (2003), "Observation of Tkachenko oscillations in rapidly rotating Bose-Einstein condensates," Physical Review Letters **91** (10), 100402.

[34] C. Cohen-Tannoudji, J. Dupont-Roc, and G. Grynberg (1998), *Atom-Photon Interactions: Basic Processes and Applications* (Wiley).

[35] Y. Colombe, E. Knyazchyan, O. Morizot, B. Mercier, V. Lorent, and H. Perrin (2004), "Ultracold atoms confined in rf-induced two-dimensional trapping potentials," Europhysics Letters **67** (4), 593.

[36] N. Cooper (2008), "Rapidly rotating atomic gases," Advances in Physics **57** (6), 539–616.

[37] L. Corman (2016), *The two-dimensional Bose gas in box potentials*, Ph.D. thesis (École normale supérieure, Université Paris Sciences Lettres).

[38] L. Corman, L. Chomaz, T. Bienaimé, R. Desbuquois, C. Weitenberg, S. Nascimbène, J. Dalibard, and J. Beugnon (2014), "Quench-induced supercurrents in an annular Bose gas," Physical Review Letters **113** (13), 135302.

[39] E. A. Cornell, and C. E. Wieman (2002), "Nobel lecture: Bose-Einstein condensation in a dilute gas, the first 70 years and some recent experiments," Reviews of Modern Physics **74** (3), 875–893.

[40] M. Cozzini (2006), "Diffused vorticity approach to the oscillations of a rotating Bose-Einstein condensate confined in a harmonic plus quartic trap," Pramana **66** (1), 31–42.

[41] M. Cozzini, A. L. Fetter, B. Jackson, and S. Stringari (2005), "Oscillations of a Bose-Einstein condensate rotating in a harmonic plus quartic trap," Physical Review Letters **94**, 100402.

[42] M. Cozzini, and S. Stringari (2003), "Macroscopic dynamics of a Bose-Einstein condensate containing a vortex lattice," Physical Review A **67** (4), 041602.

[43] F. Dalfovo, S. Giorgini, L. P. Pitaevskii, and S. Stringari (1999), "Theory of Bose-Einstein condensation in trapped gases," Reviews of Modern Physics **71** (3), 463–512.

[44] K. B. Davis, M. O. O. Mewes, M. R. Andrews, N. J. van Druten, D. S. Durfee, D. M. Kurn, and W. Ketterle (1995), "Bose-Einstein condensation in a gas of sodium atoms," Physical Review Letters **75** (22), 3969–3973.

[45] C. De Rossi (2016), *Gaz de Bose en dimension deux : modes collectifs, superfluidité et piège annulaire*, Ph.D. thesis (Université Paris 13, Sorbonne Paris Cité).

[46] C. De Rossi, R. Dubessy, K. Merloti, M. de Goër de Herve, T. Badr, A. Perrin, L. Longchambon, and H. Perrin (2016), "Probing superfluidity in a quasi two-dimensional Bose gas through its local dynamics," New Journal of Physics **18** (6), 062001.

[47] C. De Rossi, R. Dubessy, K. Merloti, M. de Goër de Herve, T. Badr, A. Perrin, L. Longchambon, and H. Perrin (2017), "The scissors oscillation of a quasi two-dimensional Bose gas as a local signature of superfluidity," Journal of Physics: Conference Series **793** (1), 012023.

[48] G. Del Pace, K. Xhani, A. Muzi Falconi, M. Fedrizzi, N. Grani, D. Hernandez Rajkov, M. Inguscio, F. Scazza, W. Kwon, and G. Roati (2022), "Imprinting persistent currents in tunable fermionic rings," Physical Review X **12** (4), 041037.

[49] B. DeMarco, and D. S. Jin (1999), "Onset of Fermi degeneracy in a trapped atomic gas," Science **285** (5434), 1703–1706.

[50] R. Desbuquois (2013), *Thermal and superfluid properties of the two–dimensional Bose gas*, Ph.D. thesis (Université Pierre et Marie Curie - Paris VI).

[51] R. Desbuquois, L. Chomaz, T. Yefsah, J. Léonard, J. Beugnon, C. Weitenberg, and J. Dalibard (2012), "Superfluid behaviour of a two-dimensional Bose gas," Nature Physics **8** (9), 645–648.

[52] R. Desbuquois, T. Yefsah, L. Chomaz, C. Weitenberg, L. Corman, S. Nascimbène, and J. Dalibard (2014), "Determination of scale-invariant equations of state without fitting parameters: Application to the two-dimensional Bose gas across the Berezinskii-Kosterlitz-Thouless transition," Physical Review Letters **113**, 020404.

[53] S. M. Dickerson, J. M. Hogan, A. Sugarbaker, D. M. S. Johnson, and M. A. Kasevich (2013), "Multiaxis inertial sensing with long-time point source atom interferometry," Physical Review Letters **111** (8), 83001.

[54] B. Doyon, J. Dubail, R. Konik, and T. Yoshimura (2017), "Large-scale description of interacting one-dimensional Bose gases: Generalized hydrodynamics supersedes conventional hydrodynamics," Physical Review Letters **119** (19), 195301.

[55] B. Doyon, and T. Yoshimura (2017), "A note on generalized hydrodynamics: inhomogeneous fields and other concepts," SciPost Physics **2** (2), 014.

[56] N. J. van Druten, and W. Ketterle (1997), "Two-step condensation of the ideal Bose gas in highly anisotropic traps," Physical Review Letters **79** (4), 549–552.

[57] J. Dubail (2016), "A more efficient way to describe interacting quantum particles in 1D," Physics **9** (December), 153.

[58] R. Dubessy, C. De Rossi, T. Badr, L. Longchambon, and H. Perrin (2014), "Imaging the collective excitations of an ultracold gas using statistical correlations," New Journal of Physics **16** (12), 122001.

[59] R. Dubessy, C. De Rossi, M. de Goër de Herve, T. Badr, A. Perrin, L. Longchambon, and H. Perrin (2018), "Local correlations reveal the superfluid to normal boundary in a trapped two-dimensional quantum gas," AIP Conference Proceedings **1936** (1), 020027.

[60] R. Dubessy, T. Liennard, P. Pedri, and H. Perrin (2012a), "Critical rotation of an annular superfluid Bose-Einstein condensate," Physical Review A **86**, 011602(R).

[61] R. Dubessy, K. Merloti, L. Longchambon, P.-E. Pottie, T. Liennard, A. Perrin, V. Lorent, and H. Perrin (2012b), "Rubidium-87 Bose-Einstein condensate in an optically plugged quadrupole trap," Physical Review A **85**, 013643.

[62] R. Dubessy, J. Polo, H. Perrin, A. Minguzzi, and M. Olshanii (2021), "Universal shock-wave propagation in one-dimensional Bose fluids," Physical Review Research **3**, 013098.

[63] S. Eckel, F. Jendrzejewski, A. Kumar, C. J. Lobb, and G. K. Campbell (2014a), "Interferometric measurement of the current-phase relationship of a superfluid weak link," Physical Review X **4** (3), 031052.

[64] S. Eckel, J. G. Lee, F. Jendrzejewski, C. J. Lobb, G. K. Campbell, and W. T. Hill (2016), "Contact resistance and phase slips in mesoscopic superfluid-atom transport," Physical Review A **93** (6), 063619.

[65] S. Eckel, J. G. Lee, F. Jendrzejewski, N. Murray, C. W. Clark, C. J. Lobb, W. D. Phillips, M. Edwards, and G. K. Campbell (2014b), "Hysteresis in a quantized superfluid 'atomtronic' circuit," Nature **506** (7487), 200–3.

[66] G. El, and M. Hoefer (2016), "Dispersive shock waves and modulation theory," Physica D: Nonlinear Phenomena **333**, 11–65.

[67] T. Esslinger, and G. Blatter (2006), "Quantum physics: atomic gas in flatland." Nature **441** (7097), 1053–1054.

[68] A. L. Fetter (2001), "Rotating vortex lattice in a Bose-Einstein condensate trapped in combined quadratic and quartic radial potentials," Physical Review A **64**, 063608.

[69] A. L. Fetter (2009), "Rotating trapped Bose-Einstein condensates," Reviews of Modern Physics **81** (2), 647–691.

[70] A. L. Fetter, B. Jackson, and S. Stringari (2005), "Rapid rotation of a Bose-Einstein condensate in a harmonic plus quartic trap," Physical Review A **71**, 013605.

[71] R. J. Fletcher, M. Robert-de Saint-Vincent, J. Man, N. Navon, R. P. Smith, K. G. H. Viebahn, and Z. Hadzibabic (2015), "Connecting Berezinskii-Kosterlitz-Thouless and BEC phase transitions by tuning interactions in a trapped gas," Physical Review Letters **114**, 255302.

[72] R. J. Fletcher, A. Shaffer, C. C. Wilson, P. B. Patel, Z. Yan, V. Crépel, B. Mukherjee, and M. W. Zwierlein (2021), "Geometric squeezing into the lowest Landau level," Science **372** (6548), 1318–1322.

[73] D. G. Fried, T. C. Killian, L. Willmann, D. Landhuis, S. C. Moss, D. Kleppner, and T. J. Greytak (1998), "Bose-Einstein condensation of atomic Hydrogen," Physical Review Letters **81**, 3811–3814.

[74] T. Fukuhara, Y. Takasu, M. Kumakura, and Y. Takahashi (2007), "Degenerate Fermi gases of Ytterbium," Physical Review Letters **98** (3), 030401.

[75] M. Gałka, P. Christodoulou, M. Gazo, A. Karailiev, N. Dogra, J. Schmitt, and Z. Hadzibabic (2022), "Emergence of isotropy and dynamic scaling in 2d wave turbulence in a homogeneous Bose gas," Physical Review Letters **129**, 190402.

[76] M. Gałka, N. Dogra, R. Lopes, J. Schmitt, and Z. Hadzibabic (2021), "Observation of first and second sound in a BKT superfluid," Nature **594**, 191–194.

[77] B. M. Garraway, and H. Perrin (2016), "Recent developments in trapping and manipulation of atoms with adiabatic potentials," Journal of Physics B: Atomic, Molecular and Optical Physics **49** (17), 172001.

[78] U. Gasser, C. Eisenmann, G. Maret, and P. Keim (2010), "Melting of crystals in two dimensions," ChemPhysChem **11** (5), 963–970.

[79] A. L. Gaunt, T. F. Schmidutz, I. Gotlibovych, R. P. Smith, and Z. Hadzibabic (2013), "Bose-Einstein condensation of atoms in a uniform potential," Physical Review Letters **110**, 200406.

[80] G. Gauthier, T. A. Bell, A. B. Stilgoe, M. Baker, H. Rubinsztein-Dunlop, and T. W. Neely (2021), "Chapter one - dynamic high-resolution optical trapping of ultracold atoms," (Academic Press) pp. 1–101.

[81] G. Gauthier, M. T. Reeves, X. Yu, A. S. Bradley, M. A. Baker, T. A. Bell, H. Rubinsztein-Dunlop, M. J. Davis, and T. W. Neely (2019), "Giant vortex clusters in a two-dimensional quantum fluid," Science **364** (6447), 1264–1267.

[82] S. A. Gifford, and G. Baym (2008), "Dislocation-mediated melting in superfluid vortex lattices," Physical Review A **78** (4), 043607.

[83] M. Gildemeister, E. Nugent, B. E. Sherlock, M. Kubasik, B. T. Sheard, and C. J. Foot (2010), "Trapping ultracold atoms in a time-averaged adiabatic potential," Physical Review A **81** (3), 031402.

[84] M. Gildemeister, B. E. Sherlock, and C. J. Foot (2012), "Techniques to cool and rotate Bose-Einstein condensates in time-averaged adiabatic potentials," Physical Review A **85** (5), 053401.

[85] M. Girardeau (1960), "Relationship between systems of impenetrable bosons and fermions in one dimension," Journal of Mathematical Physics **1** (6), 516–523.

[86] A. Griesmaier, J. Werner, S. Hensler, J. Stuhler, and T. Pfau (2005), "Bose-Einstein condensation of Chromium," Physical Review Letters **94** (16), 160401.

[87] D. Guéry-Odelin, and S. Stringari (1999), "Scissors mode and superfluidity of a trapped Bose-Einstein condensed gas," Physical Review Letters **83**, 4452–4455.

[88] Y. Guo (2021), *Annular quantum gases in a bubble-shaped trap: from equilibrium to strong rotations*, Ph.D. thesis (Université Sorbonne Paris Nord - Paris XIII).

[89] Y. Guo, R. Dubessy, M. de Goër de Herve, A. Kumar, T. Badr, A. Perrin, L. Longchambon, and H. Perrin (2020), "Supersonic rotation of a superfluid: A long-lived dynamical ring," Physical Review Letters **124**, 025301.

[90] Y. Guo, E. Mercado Gutierrez, D. Rey, T. Badr, A. Perrin, L. Longchambon, V. S. Bagnato, H. Perrin, and R. Dubessy (2022), "Expansion of a quantum gas in a shell trap," New Journal of Physics **24** (9), 093040.

[91] S. Gupta, K. W. Murch, K. L. Moore, T. P. Purdy, and D. M. Stamper-Kurn (2005), "Bose-Einstein condensation in a circular waveguide," Physical Review Letters **95** (14), 143201.

[92] D. Guéry-Odelin (2000), "Spinning up and down a Boltzmann gas," Physical Review A **62** (3), 033607.

[93] A. Görlitz, J. M. Vogels, A. E. Leanhardt, C. Raman, T. L. Gustavson, J. R. Abo-Shaeer, A. P. Chikkatur, S. Gupta, S. Inouye, T. Rosenband, and W. Ketterle (2001), "Realization of Bose-Einstein condensates in lower dimensions." Physical review letters **87** (13), 130402.

[94] Z. Hadzibabic, and J. Dalibard (2013), "BKT physics with two-dimensional atomic gases," in *40 Years of Berezinskii–Kosterlitz–Thouless Theory* (World Scientific) pp. 297–323.

[95] Z. Hadzibabic, P. Krüger, M. Cheneau, B. Battelier, and J. Dalibard (2006), "Berezinskii-Kosterlitz-Thouless crossover in a trapped atomic gas," Nature **441** (7097), 1118–1121.

[96] V. Hakim (1997), "Nonlinear Schrödinger flow past an obstacle in one dimension," Physical Review E **55** (3), 2835–2845.

[97] T. L. Harte, E. Bentine, K. Luksch, A. J. Barker, D. Trypogeorgos, B. Yuen, and C. J. Foot (2018), "Ultracold atoms in multiple radio-frequency dressed adiabatic potentials," Physical Review A **97** (1), 013616.

[98] W. H. Heathcote, E. Nugent, B. T. Sheard, and C. J. Foot (2008), "A ring trap for ultracold atoms in an RF-dressed state," New Journal of Physics **10** (4), 043012.

[99] G. Hechenblaikner, J. M. Krueger, and C. J. Foot (2005), "Properties of quasi-two-dimensional condensates in highly anisotropic traps," Physical Review A **71** (1), 013604.

[100] J. Hertkorn, J.-N. Schmidt, F. Böttcher, M. Guo, M. Schmidt, K. S. H. Ng, S. D. Graham, H. P. Büchler, T. Langen, M. Zwierlein, and T. Pfau (2021), "Density fluctuations across the superfluid-supersolid phase transition in a dipolar quantum gas," Physical Review X **11**, 011037.

[101] M. de Goër de Herve (2018), *Superfluid dynamics of annular Bose gases*, Ph.D. thesis (Université Paris 13, Sorbonne Paris Cité).

[102] M. de Goër de Herve, Y. Guo, C. De Rossi, A. Kumar, T. Badr, R. Dubessy, L. Longchambon, and H. Perrin (2021), "A versatile ring trap for quantum gases," Journal of Physics B: Atomic, Molecular and Optical Physics **54** (12), 125302.

[103] P. C. Hohenberg (1967), "Existence of long-range order in one and two dimensions," Physical Review **158**, 383–386.

[104] M. Holzmann, M. Chevallier, and W. Krauth (2008), "Semiclassical theory of the quasi–two-dimensional trapped Bose gas," Europhysics Letters **82** (3), 30001.

[105] F. Jendrzejewski, S. Eckel, N. Murray, C. Lanier, M. Edwards, C. J. Lobb, and G. K. Campbell (2014), "Resistive flow in a weakly interacting Bose-Einstein condensate," Physical Review Letters **113** (4), 045305.

[106] S. Jochim, M. Bartenstein, A. Altmeyer, G. Hendl, S. Riedl, C. Chin, J. Hecker Denschlag, and R. Grimm (2003), "Bose-Einstein condensation of molecules," Science **302** (5653), 2101–2103.

[107] I. T. Jolliffe (2012), *Principal Component Analysis* (Springer New York, NY).

[108] B. D. Josephson (1962), "Possible new effects in superconductive tunnelling," Physics Letters **1** (7), 251 – 253.

[109] Y. Kagan, E. L. Surkov, and G. V. Shlyapnikov (1996), "Evolution of a Bose-condensed gas under variations of the confining potential," Physical Review A **54** (3), R1753–R1756.

[110] S. Kang, J. Choi, S. W. Seo, W. J. Kwon, and Y. Shin (2015), "Rotating a Bose-Einstein condensate by shaking an anharmonic axisymmetric magnetic potential," Physical Review A **91**, 013603.

[111] T. Karpiuk, P. Deuar, P. Bienias, E. Witkowska, K. Pawłowski, M. Gajda, K. Rzążewski, and M. Brewczyk (2012), "Spontaneous solitons in the thermal equilibrium of a quasi-1D Bose gas," Physical Review Letters **109** (20), 205302.

[112] T. Karpiuk, T. Sowiński, M. Gajda, K. Rzążewski, and M. Brewczyk (2015), "Correspondence between dark solitons and the type II excitations of the Lieb-Liniger model," Physical Review A **91** (1), 013621.

[113] K. Kasamatsu, M. Tsubota, and M. Ueda (2002), "Giant hole and circular superflow in a fast rotating Bose-Einstein condensate," Physical Review A **66**, 053606.

[114] G. M. Kavoulakis, and G. Baym (2003), "Rapidly rotating Bose-Einstein condensates in anharmonic potentials," New Journal of Physics **5**, 10.1088/1367-2630/5/1/351.

[115] W. Ketterle (2002), "Nobel lecture: When atoms behave as waves: Bose-Einstein condensation and the atom laser," Reviews of Modern Physics **74** (4), 1131–1151.

[116] W. Ketterle, D. S. Durfee, and D. M. Stamper-Kurn (1999), "Making, probing and understanding Bose-Einstein condensates," in *Proceedings of the International School of Physics "\,{E}nrico {F}ermi\,", Course {CXL}*, edited by M. Inguscio, S. Stringari, and C. E. Wieman (IOS Press) pp. 67–176.

[117] M. Key, I. G. Hughes, W. Rooijakkers, B. E. Sauer, E. A. Hinds, D. J. Richardson, and P. G. Kazansky (2000), "Propagation of cold atoms along a miniature magnetic guide," Physical Review Letters **84** (7), 1371–1373.

[118] S. J. Kim, H. Yu, S. T. Gang, D. Z. Anderson, and J. B. Kim (2016), "Controllable asymmetric double well and ring potential on an atom chip," Physical Review A **93** (3), 033612.

[119] T. Kinoshita, T. Wenger, and D. S. Weiss (2006), "A quantum Newton's cradle," Nature **440** (7086), 900–903.

[120] S. Kraft, F. Vogt, O. Appel, F. Riehle, and U. Sterr (2009), "Bose-Einstein condensation of alkaline earth atoms: Ca 40," Physical Review Letters **103** (13), 130401.

[121] A. Kumar, N. Anderson, W. D. Phillips, S. Eckel, G. K. Campbell, and S. Stringari (2016), "Minimally destructive, Doppler measurement of a quantized flow in a ring-shaped Bose-Einstein condensate," New Journal of Physics **18** (2), 25001.

[122] A. Kumar, R. Dubessy, T. Badr, C. De Rossi, M. de Goër de Herve, L. Longchambon, and H. Perrin (2018), "Producing superfluid circulation states using phase imprinting," Physical Review A **97**, 043615.

[123] A. Kumar, S. Eckel, F. Jendrzejewski, and G. K. Campbell (2017), "Temperature-induced decay of persistent currents in a superfluid ultracold gas," Physical Review A **95** (2), 021602.

[124] W. J. Kwon, G. Moon, S. W. Seo, and Y. Shin (2015), "Critical velocity for vortex shedding in a Bose-Einstein condensate," Physical Review A **91** (5), 053615.

[125] L. Lavoine, A. Hammond, A. Recati, D. S. Petrov, and T. Bourdel (2021), "Beyond-mean-field effects in Rabi-coupled two-component Bose-Einstein condensate," Physical Review Letters **127**, 203402.

[126] I. Lesanovsky, and W. von Klitzing (2007), "Time-averaged adiabatic potentials: Versatile matter-wave guides and atom traps," Physical Review Letters **99**, 083001.

[127] E. H. Lieb (1963), "Exact analysis of an interacting Bose gas. II. the excitation spectrum," Physical Review **130** (4), 1616–1624.

[128] E. H. Lieb, and W. Liniger (1963), "Exact analysis of an interacting Bose gas. I. the general solution and the ground state," Physical Review **130** (4), 1605–1616.

[129] T. Liennard (2011), *Construction d'un montage de condensation de Bose–Einstein de rubidium et étude théorique d'un superfluide en rotation dans un anneau*, Ph.D. thesis (Université Paris 13).

[130] Y.-J. Lin, A. R. Perry, R. L. Compton, I. B. Spielman, and J. V. Porto (2009), "Rapid production of ^{87}rb Bose-Einstein condensates in a combined magnetic and optical potential," Physical Review A **79** (6), 063631.

[131] C. Lobo, A. Sinatra, and Y. Castin (2004), "Vortex lattice formation in Bose-Einstein condensates," Physical review letters **92** (2), 020403.

[132] M. Lu, N. Q. Burdick, and B. L. Lev (2012), "Quantum degenerate dipolar Fermi gas," Physical Review Letters **108** (21), 215301.

[133] M. Lu, N. Q. Burdick, S. H. Youn, and B. L. Lev (2011), "Strongly dipolar Bose-Einstein condensate of Dysprosium," Physical Review Letters **107** (19), 190401.

[134] K. Luksch, E. Bentine, A. J. Barker, S. Sunami, T. L. Harte, B. Yuen, and C. J. Foot (2019), "Probing multiple-frequency atom-photon interactions with ultracold atoms," New Journal of Physics **21** (7), 073067.

[135] E. Lundh (2002), "Multiply quantized vortices in trapped Bose-Einstein condensates," Physical Review A **65** (4), 043604.

[136] K. W. Madison, F. Chevy, V. Bretin, and J. Dalibard (2001), "Stationary states of a rotating Bose-Einstein condensate: Routes to vortex nucleation," Physical Review Letters **86** (20), 4443–4446.

[137] K. W. Madison, F. Chevy, W. Wohlleben, and J. Dalibard (2000), "Vortex formation in a stirred Bose-Einstein condensate," Physical Review Letters **84**, 806–809.

[138] N. Malvania, Y. Zhang, Y. Le, J. Dubail, M. Rigol, and D. S. Weiss (2021), "Generalized hydrodynamics in strongly interacting 1D Bose gases," Science **373** (6559), 1129–1133.

[139] O. M. Maragò, S. A. Hopkins, J. Arlt, E. Hodby, G. Hechenblaikner, and C. J. Foot (2000), "Observation of the scissors mode and evidence for superfluidity of a trapped Bose-Einstein condensed gas," Physical Review Letters **84** (10), 2056–2059.

[140] H. Mas, S. Pandey, G. Vasilakis, and W. von Klitzing (2019), "Bi-chromatic adiabatic shells for atom interferometry," New Journal of Physics **21** (12), 123039.

[141] K. Merloti (2013), *Condensat de Bose-Einstein dans un piège habillé : modes collectifs d'un superfluide en dimension deux*, Ph.D. thesis (Université Paris 13, Sorbonne Paris Cité).

[142] K. Merloti, R. Dubessy, L. Longchambon, M. Olshanii, and H. Perrin (2013a), "Breakdown of scale invariance in a quasi-two-dimensional Bose gas due to the presence of the third dimension," Physical Review A **88**, 061603.

[143] K. Merloti, R. Dubessy, L. Longchambon, A. Perrin, P.-E. Pottie, V. Lorent, and H. Perrin (2013b), "A two-dimensional quantum gas in a magnetic trap," New Journal of Physics **15** (3), 033007.

[144] N. D. Mermin, and H. Wagner (1966), "Absence of ferromagnetism or antiferromagnetism in one- or two-dimensional isotropic Heisenberg models," Physical Review Letters **17**, 1133–1136.

[145] Y. Miyazawa, R. Inoue, H. Matsui, G. Nomura, and M. Kozuma (2022), "Bose-Einstein condensation of Europium," Physical Review Letters **129** (22), 223401.

[146] G. Modugno, G. Ferrari, G. Roati, R. J. Brecha, A. Simoni, and M. Inguscio (2001), "Bose-Einstein condensation of Potassium atoms by sympathetic cooling," Science **294** (5545), 1320–1322.

[147] O. Morizot, Y. Colombe, V. Lorent, H. Perrin, and B. M. Garraway (2006), "Ring trap for ultracold atoms," Physical Review A **74** (2), 023617.

[148] S. Moulder, S. Beattie, R. P. Smith, N. Tammuz, and Z. Hadzibabic (2012), "Quantized supercurrent decay in an annular Bose-Einstein condensate," Physical Review A **86** (1), 013629.

[149] B. Mukherjee, A. Shaffer, P. B. Patel, Z. Yan, C. C. Wilson, V. Crépel, R. J. Fletcher, and M. Zwierlein (2022), "Crystallization of bosonic quantum Hall states in a rotating quantum gas," Nature **601**, 58–62.

[150] D. Müller, D. Z. Anderson, R. J. Grow, P. D. D. Schwindt, and E. A. Cornell (1999), "Guiding neutral atoms around curves with lithographically patterned current-carrying wires," Physical Review Letters **83** (25), 5194–5197.

[151] S. Nascimbène, N. Navon, K. J. Jiang, F. Chevy, and C. Salomon (2010), "Exploring the thermodynamics of a universal Fermi gas," Nature **463** (7284), 1057–1060.

[152] G. Natale, R. M. W. van Bijnen, A. Patscheider, D. Petter, M. J. Mark, L. Chomaz, and F. Ferlaino (2019), "Excitation spectrum of a trapped dipolar supersolid and its experimental evidence," Physical Review Letters **123**, 050402.

[153] P. Navez, S. Pandey, H. Mas, K. Poulios, T. Fernholz, and W. Von Klitzing (2016), "Matter-wave interferometers using TAAP rings," New Journal of Physics **18** (7), 10.1088/1367-2630/18/7/075014.

[154] B. Naylor, A. Reigue, E. Maréchal, O. Gorceix, B. Laburthe-Tolra, and L. Vernac (2015), "Chromium dipolar Fermi sea," Physical Review A **91** (1), 011603.

[155] S. Nazarenko (2011), *Wave Turbulence*, Vol. 825 (Springer Berlin Heidelberg).

[156] C. F. Ockeloen, A. F. Tauschinsky, R. J. C. Spreeuw, and S. Whitlock (2010), "Detection of small atom numbers through image processing," Physical Review A **82**, 061606.

[157] M. Olshanii, H. Perrin, and V. Lorent (2010), "Example of a quantum anomaly in the physics of ultracold gases," Physical Review Letters **105** (9), 095302.

[158] S. Pandey, H. Mas, G. Drougakis, P. Thekkeppatt, V. Bolpasi, G. Vasilakis, K. Poulios, and W. von Klitzing (2019), "Hypersonic Bose–Einstein condensates in accelerator rings," Nature **570** (7760), 205–209.

[159] F. Pereira Dos Santos, J. Léonard, J. Wang, C. J. Barrelet, F. Perales, E. Rasel, C. S. Unnikrishnan, M. Leduc, and C. Cohen-Tannoudji (2001), "Bose-Einstein condensation of metastable Helium," Physical Review Letters **86** (16), 3459–3462.

[160] H. Perrin, and B. M. Garraway (2017), "Chapter four - trapping atoms with radio frequency adiabatic potentials," Advances In Atomic, Molecular, and Optical Physics **66**, 181–262.

[161] L. P. Pitaevskii, and A. Rosch (1997), "Breathing modes and hidden symmetry of trapped atoms in two dimensions," Physical Review A **55** (2), R853–R856.

[162] J. Polo, R. Dubessy, P. Pedri, H. Perrin, and A. Minguzzi (2019), "Oscillations and decay of superfluid currents in a one-dimensional Bose gas on a ring," Physical Review Letters **123**, 195301.

[163] N. Prokof'ev, O. Ruebenacker, and B. Svistunov (2001), "Critical point of a weakly interacting two-dimensional Bose gas," Physical Review Letters **87**, 270402.

[164] N. Prokof'ev, and B. Svistunov (2002), "Two-dimensional weakly interacting Bose gas in the fluctuation region," Physical Review A **66**, 043608.

[165] N. P. Proukakis, and B. Jackson (2008), "Finite-temperature models of Bose–Einstein condensation," Journal of Physics B: Atomic, Molecular and Optical Physics **41** (20), 203002.

[166] A. Rakonjac, A. L. Marchant, T. P. Billam, J. L. Helm, M. M. H. Yu, S. A. Gardiner, and S. L. Cornish (2016), "Measuring the disorder of vortex lattices in a Bose-Einstein condensate," Physical Review A **93**, 013607.

[167] A. Ramanathan, K. C. Wright, S. R. Muniz, M. Zelan, W. T. Hill, C. J. Lobb, K. Helmerson, W. D. Phillips, and G. K. Campbell (2011), "Superflow in a toroidal Bose-Einstein condensate: An atom circuit with a tunable weak link," Physical Review Letters **106** (13), 130401.

[168] G. Reinaudi, T. Lahaye, Z. Wang, and D. Guéry-Odelin (2007), "Strong saturation absorption imaging of dense clouds of ultracold atoms," Optics Letters **32** (21), 3143.

[169] D. Rey (2023), *Control and optimization of a Bose-Einstein condensation experiment*, Ph.D. thesis (Université Sorbonne Paris Nord - Paris XIII).

[170] D. Rey, S. Thomas, R. Sharma, T. Badr, L. Longchambon, R. Dubessy, and H. Perrin (2022), "Loading a quantum gas from a hybrid dimple trap to a shell trap," Journal of Applied Physics **132** (21), 214401.

[171] S. J. Rooney, P. B. Blakie, B. P. Anderson, and A. S. Bradley (2011), "Suppression of Kelvon-induced decay of quantized vortices in oblate Bose-Einstein condensates," Physical Review A **84** (2), 023637.

[172] A. Roussou, J. Smyrnakis, M. Magiropoulos, N. K. Efremidis, W. von Klitzing, and G. M. Kavoulakis (2019), "Fragility of the bosonic Laughlin state," Physical Review A **99** (5), 053613.

[173] C. Ryu, M. Andersen, P. Cladé, V. Natarajan, K. Helmerson, and W. Phillips (2007), "Observation of persistent flow of a Bose-Einstein condensate in a toroidal trap," Physical Review Letters **99** (26), 260401.

[174] C. Ryu, and M. G. Boshier (2015), “Integrated coherent matter wave circuits,” New Journal of Physics **17** (9), 92002.

[175] C. Ryu, E. C. Samson, and M. G. Boshier (2020), “Quantum interference of currents in an atomtronic SQUID,” Nature Communications **11** (1), 2–7.

[176] A. K. Saha, and R. Dubessy (2021), “Dynamical phase diagram of a one-dimensional Bose gas in a box with a tunable weak link: From Bose-Josephson oscillations to shock waves,” Physical Review A **104**, 023316.

[177] A. K. Saha, and R. Dubessy (2022), “Characterizing far from equilibrium states of the one-dimensional nonlinear Schrödinger equation,” .

[178] R. Saint-Jalm, P. C. Castilho, Le Cerf, B. Bakkali-Hassani, J. L. Ville, S. Nascimbene, J. Beugnon, and J. Dalibard (2019), “Dynamical symmetry and breathers in a two-dimensional Bose gas,” Physical Review X **9** (2), 21035.

[179] M. Schemmer, I. Bouchoule, B. Doyon, and J. Dubail (2019), “Generalized hydrodynamics on an atom chip,” Physical Review Letters **122** (9), 90601.

[180] F. Schreck, L. Khaykovich, K. L. Corwin, G. Ferrari, T. Bourdel, J. Cubizolles, and C. Salomon (2001), “Quasipure Bose-Einstein condensate immersed in a Fermi sea,” Physical Review Letters **87** (8), 080403.

[181] T. Schumm, S. Hofferberth, L. M. Andersson, S. Wildermuth, S. Groth, I. Bar-Joseph, J. Schmiedmayer, and P. Krüger (2005), “Matter-wave interferometry in a double well on an atom chip,” Nature Physics **1**, 57–62.

[182] V. Schweikhard, I. Coddington, P. Engels, V. P. Mogendorff, and E. a. Cornell (2004), “Rapidly rotating Bose-Einstein condensates in and near the lowest Landau level,” Physical Review Letters **92** (4), 040404.

[183] S. R. Segal, Q. Diot, E. A. Cornell, A. A. Zozulya, and D. Z. Anderson (2010), “Revealing buried information: Statistical processing techniques for ultracold-gas image analysis,” Physical Review A **81** (5), 53601.

[184] B. E. Sherlock, M. Gildemeister, E. Owen, E. Nugent, and C. J. Foot (2011), “Time-averaged adiabatic ring potential for ultracold atoms,” Physical Review A **83** (4), 043408.

[185] T. P. Simula, M. J. Davis, and P. B. Blakie (2008), “Superfluidity of an interacting trapped quasi-two-dimensional Bose gas,” Physical Review A **77**, 023618.

[186] S. Sinha, and Y. Castin (2001), “Dynamic instability of a rotating Bose-Einstein condensate,” Physical Review Letters **87** (19), 190402.

[187] D. A. Steck (2021), “Rubidium 87 D line data,” Available online at http://steck.us/alkalidata (revision 2.2.2, 9 July 2021).

[188] S. Stellmer, M. K. Tey, B. Huang, R. Grimm, and F. Schreck (2009), “Bose-Einstein condensation of Strontium,” Physical Review Letters **103** (20), 200401.

[189] S. Stringari (1996a), “Collective excitations of a trapped Bose-condensed gas,” Physical Review Letters **77**, 2360–2363.

[190] S. Stringari (1996b), "Moment of inertia and superfluidity of a trapped Bose gas," Physical Review Letters **76**, 1405–1408.

[191] A. Sugarbaker, S. M. Dickerson, J. M. Hogan, D. M. S. Johnson, and M. A. Kasevich (2013), "Enhanced atom interferometer readout through the application of phase shear," Physical Review Letters **111** (11), 113002.

[192] S. Sunami, V. P. Singh, D. Garrick, A. Beregi, A. J. Barker, K. Luksch, E. Bentine, L. Mathey, and C. J. Foot (2022), "Observation of the Berezinskii-Kosterlitz-Thouless transition in a two-dimensional Bose gas via matter-wave interferometry," Physical Review Letters **128**, 250402.

[193] P. Suret, A. Tikan, F. Bonnefoy, F. Copie, G. Ducrozet, A. Gelash, G. Prabhudesai, G. Michel, A. Cazaubiel, E. Falcon, G. El, and S. Randoux (2020), "Nonlinear spectral synthesis of soliton gas in deep-water surface gravity waves," Physical Review Letters **125** (26), 264101.

[194] Y. Takasu, K. Maki, K. Komori, T. Takano, K. Honda, M. Kumakura, T. Yabuzaki, and Y. Takahashi (2003), "Spin-singlet Bose-Einstein condensation of two-electron atoms," Physical Review Letters **91** (4), 040404.

[195] V. Tkachenko (1966), "Stability of vortex lattices," Soviet Journal of Experimental and Theoretical Physics **23** (6), 1049.

[196] A. G. Truscott, K. E. Strecker, W. I. McAlexander, G. B. Partridge, and R. G. Hulet (2001), "Observation of Fermi pressure in a gas of trapped atoms," Science **291** (5513), 2570–2572.

[197] T. Tsuzuki (1971), "Nonlinear waves in the Pitaevskii-Gross equation," Journal of Low Temperature Physics **4** (4), 441–457.

[198] Y.-H. Wang, A. Kumar, F. Jendrzejewski, R. M. Wilson, M. Edwards, S. Eckel, G. K. Campbell, and C. W. Clark (2015), "Resonant wavepackets and shock waves in an atomtronic SQUID," New Journal of Physics **17** (12), 125012.

[199] G. Watanabe, G. Baym, and C. J. Pethick (2004), "Landau levels and the Thomas-Fermi structure of rapidly rotating Bose-Einstein condensates," Physical Review Letters **93**, 190401.

[200] T. Weber, J. Herbig, M. Mark, H.-C. Nägerl, and R. Grimm (2003), "Bose-Einstein condensation of Cesium," Science **299** (5604), 232–235.

[201] P. B. Wigley, P. J. Everitt, K. S. Hardman, M. R. Hush, C. H. Wei, M. A. Sooriyabandara, P. Manju, J. D. Close, N. P. Robins, and C. C. N. Kuhn (2016), "Non-destructive shadowgraph imaging of ultra-cold atoms," Optics Letters **41** (20), 4795.

[202] K. C. Wright, R. B. Blakestad, C. J. Lobb, W. D. Phillips, and G. K. Campbell (2013a), "Driving phase slips in a superfluid atom circuit with a rotating weak link," Physical Review Letters **110** (2), 025302.

[203] K. C. Wright, R. B. Blakestad, C. J. Lobb, W. D. Phillips, and G. K. Campbell (2013b), "Threshold for creating excitations in a stirred superfluid ring," Physical Review A **88** (6), 063633.

[204] T. M. Wright, R. J. Ballagh, A. S. Bradley, P. B. Blakie, and C. W. Gardiner (2008), "Dynamical thermalization and vortex formation in stirred two-dimensional Bose-Einstein condensates," Physical Review A **78**, 063601.

[205] O. Zobay, and B. M. Garraway (2001), "Two-dimensional atom trapping in field-induced adiabatic potentials," Physical Review Letters **86**, 1195–1198.

[206] O. Zobay, and B. M. Garraway (2004), "Atom trapping and two-dimensional Bose-Einstein condensates in field-induced adiabatic potentials," Physical Review A **69**, 023605.